

AD-A069 782

ILLINOIS UNIV AT URBANA-CHAMPAIGN COORDINATED SCIENCE LAB F/G 20/12  
ATOMIC AND ELECTRICAL PROFILE STUDIES OF ION-IMPLANTED SEMICONDUCTORS (U)  
DEC 78 G T MARCYK  
DAAB07-72-C-0259

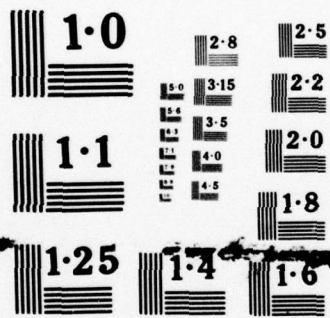
UNCLASSIFIED

R-835

NL

1 of 2  
AD  
A069782





NATIONAL BUREAU OF STANDARDS  
MICROCOPY RESOLUTION TEST CHART



SECRET 8-339

DECEMBER 1978

UHL-20079-7225

**CSL COORDINATED SCIENCE LABORATORY**

**LEVEL** *11*

*12*

AD A 069782

**ATOMIC AND ELECTRICAL  
PROFILE STUDIES OF  
ION-IMPLANTED SEMICONDUCTORS**

*FILE COPY*

**UNIVERSITY OF ILLINOIS - URBANA, ILLINOIS**

*78-08-12-143*

UNCLASSIFIED

SECURITY CLASSIFICATION OF THIS PAGE (When Data Entered)

REPORT DOCUMENTATION PAGE		READ INSTRUCTIONS BEFORE COMPLETING FORM
1. REPORT NUMBER	2. GOVT ACCESSION NO.	3. RECIPIENT'S CATALOG NUMBER
4. TITLE (and Subtitle) ATOMIC AND ELECTRICAL PROFILE STUDIES OF ION-IMPLANTED SEMICONDUCTORS.		5. TYPE OF REPORT & PERIOD COVERED Technical Report
7. AUTHOR(s) Gerald Twiggs/Marcyk		6. PERFORMING ORG. REPORT NUMBER R-835, UILU-ENG-78-2228
9. PERFORMING ORGANIZATION NAME AND ADDRESS Coordinated Science Laboratory University of Illinois at Urbana-Champaign Urbana, Illinois 61801		8. CONTRACT OR GRANT NUMBER(s) DAAB-07-72-C-0259, DAAG-29-78-C-0016, NSF DMR-77-22228; N00014-76-C-0806
11. CONTROLLING OFFICE NAME AND ADDRESS Joint Services Electronics Program		10. PROGRAM ELEMENT, PROJECT, TASK AREA & WORK UNIT NUMBERS
14. MONITORING AGENCY NAME & ADDRESS (if different from Controlling Office) (9) Doctoral thesis,		12. REPORT DATE December 1978
16. DISTRIBUTION STATEMENT (of this Report) Approved for public release; distribution unlimited		13. NUMBER OF PAGES 118
17. DISTRIBUTION STATEMENT (of the abstract entered in Block 20, if different from Report)		15. SECURITY CLASS. (of this report) UNCLASSIFIED
18. SUPPLEMENTARY NOTES		15a. DECLASSIFICATION/DOWNGRADING SCHEDULE
19. KEY WORDS (Continue on reverse side if necessary and identify by block number) Ion Implantation Optical Spectroscopy		
20. ABSTRACT (Continue on reverse side if necessary and identify by block number) The distribution of ion-implanted impurities in semiconductors was studied using atomic and electrical profiling techniques. The atomic profiles were obtained by Glow Discharge Optical Spectroscopy (GDOS). The GDOS technique, experimental system, and elemental sensitivity are discussed in detail. The impurity distributions of arsenic-implanted silicon and germanium-implanted gallium arsenide are investigated. High dose arsenic implants in silicon exhibit a concentration-dependent diffusion at high temperatures which leads to a dramatic redistribution from the original implanted profile. The		

DD FORM 1 JAN 73 1473

EDITION OF 1 NOV 65 IS OBSOLETE

UNCLASSIFIED

SECURITY CLASSIFICATION OF THIS PAGE (When Data Entered)

097 700

UNCLASSIFIED

SECURITY CLASSIFICATION OF THIS PAGE(When Data Entered)

## 20. ABSTRACT (continued)

Ge implanted into GaAs shows very little diffusion even for high concentrations annealed at 900°C. The diffusion coefficient of Ge in GaAs is estimated to be  $6 \times 10^{-15} \text{ cm}^2/\text{sec}$  at 900°C. *6 times 10 to the -15th power sq.cm,*

The electrical profiles were obtained using Hall measurements in conjunction with successive layer removal. The carrier profiles for As in Si were in substantial agreement with the atomic distributions. The carriers have a concentration limit of  $2 \times 10^{20} \text{ cm}^{-3}$  and excellent electrical activation can be obtained for 1000°C anneals. *about 2 times 10 to the 20th power/cm.cu,*

The Ge implanted into GaAs exhibits an amphoteric behavior. The implanted layers at low doses are p-type when annealed below 850°C and n-type at higher temperatures. Samples implanted at  $10^{15} \text{ cm}^{-2}$  dose were n-type for all anneal temperatures. The donor activity observed for high doses is believed to be related to the production and regrowth from an amorphous layer. The carrier profiles showed low electrical activation and mobility for both conduction types and an inactive surface region.

Germanium implantation was used to produce either p and n-type layers to form GaAs p-n junction diodes. The I-V characteristics of several implanted devices are presented. High-quality diodes can be fabricated using a  $10^{15} \text{ cm}^{-2}$  dose annealed at 800°C.

Accession For	
NTIS GML	<input checked="" type="checkbox"/>
DOC TAB	<input type="checkbox"/>
Unannounced	
Justification	
By _____	
Distribution/	
Availability Codes	
Dist	Avail and/or special
A	

UNCLASSIFIED

SECURITY CLASSIFICATION OF THIS PAGE(When Data Entered)



UILU-ENG 78-2228

ATOMIC AND ELECTRICAL PROFILE STUDIES OF  
ION-IMPLANTED SEMICONDUCTORS

by

Gerald Twiggs Marcyk

This work was supported in part by the Joint Services Electronics Program (U.S. Army, U.S. Navy and U.S. Air Force) under Contract DAAB-07-72-C-0259 and DAAG-29-78-C-0016; in part by the National Science Foundation under Grant NSF DMR-77-22228; and in part by the Office of Naval Research under Contract N00014-76-C-0806.

Reproduction in whole or in part is permitted for any purpose of the United States Government.

Approved for public release. Distribution unlimited.

ATOMIC AND ELECTRICAL PROFILE STUDIES OF  
ION-IMPLANTED SEMICONDUCTORS

BY

GERALD TWIGGS MARCYK

B.S., University of Illinois at Urbana-Champaign, 1973

M.S., University of Illinois at Urbana-Champaign, 1976

THESIS

Submitted in partial fulfillment of the requirements  
for the degree of Doctor of Philosophy in Electrical Engineering  
in the Graduate College of the  
University of Illinois at Urbana-Champaign, 1978

Thesis Adviser: Professor B. G. Streetman

Urbana, Illinois



Atomic and Electrical Profile Studies  
of Ion-Implanted Semiconductors

Gerald Twiggs Marcyk  
Coordinated Science Laboratory and  
Department of Electrical Engineering  
University of Illinois at Urbana-Champaign, 1978

The distribution of ion-implanted impurities in semiconductors was studied using atomic and electrical profiling techniques. The atomic profiles were obtained by Glow Discharge Optical Spectroscopy (GDOS). The GDOS technique, experimental system, and elemental sensitivity are discussed in detail.

The impurity distributions of arsenic-implanted silicon and germanium-implanted gallium arsenide are investigated. High dose arsenic implants in silicon exhibit a concentration-dependent diffusion at high temperatures which leads to a dramatic redistribution from the original implanted profile. The Ge implanted into GaAs shows very little diffusion even for high concentrations annealed at 900°C. The diffusion coefficient of Ge in GaAs is estimated to be  $6 \times 10^{-15} \text{ cm}^2/\text{sec}$  at 900°C.

The electrical profiles were obtained using Hall measurements in conjunction with successive layer removal. The carrier profiles for As in Si were in substantial agreement with the atomic distributions. The carriers have a concentration limit of  $\sim 2 \times 10^{20} \text{ cm}^{-3}$  and excellent electrical activation can be obtained for 1000°C anneals.

The Ge implanted into GaAs exhibits an amphoteric behavior. The implanted layers at low doses are p-type when annealed below 850°C and n-type at higher temperatures. Samples implanted at  $10^{15} \text{ cm}^{-2}$  dose were n-type for all anneal temperatures. The donor activity observed for high doses is believed to be related to the production and regrowth from an amorphous layer.

The carrier profiles showed low electrical activation and mobility for both conduction types and an inactive surface region.

Germanium implantation was used to produce either p and n-type layers to form GaAs p-n junction diodes. The I-V characteristics of several implanted devices are presented. High-quality diodes can be fabricated using a  $10^{15} \text{ cm}^{-2}$  dose annealed at  $800^{\circ}\text{C}$ .

## ACKNOWLEDGMENTS

Since research cannot be done in a vacuum, the author is indebted to a large number of people who have made contributions to this work. I would like to thank Dr. Dave Myers for supplying a wealth of information while sharing an office and for providing some electrical measurements. Mr. Siu-Sing Chan was also instrumental in producing electrical data. A number of people who have become friends as well as co-workers include Dr. John Noonan, Dr. Conilee Kirkpatrick, Dr. Al Rosa, Dr. Pollab Chatterjee, Andy Zaremba, Dean Tsang, Jon Kang, Tan-Hau Yu, Ding-Yuan Day, Max Helix, and John Oberstar. I would also like to thank the people not directly associated with this work whose advice has given me different perspectives: Dr. John Allemong, Ray Milano, Milton Feng, Eric Anderson, Joe Gibes, and especially Steve Martinck. The Coordinated Science Lab contains an excellent technical staff to whom I am deeply indebted. I would especially like to thank my typist Laura Ruggieri for her long hours of extra effort. I would like to thank my parents for their emotional and financial support during my seemingly endless career as a student. Finally, my wife, Michelle, has been a constant source of comfort and companionship through this difficult and exciting period.



## TABLE OF CONTENTS

	PAGE
1. <u>INTRODUCTION</u> . . . . .	1
1.1. Ion Implantation . . . . .	1
1.2. Electrical Measurements . . . . .	4
1.3. Atomic Measurements . . . . .	4
2. <u>DISCHARGE AND SPUTTERING PHENOMENA</u> . . . . .	6
2.1. Gas Discharges . . . . .	6
2.2. Sputtering . . . . .	10
2.3. Sputtering in a Glow Discharge . . . . .	22
3. <u>GLOW DISCHARGE OPTICAL SPECTROSCOPY</u> . . . . .	26
3.1. Optical Spectroscopy . . . . .	26
3.2. Light Emission Characteristics . . . . .	28
3.3. Experimental Apparatus . . . . .	31
4. <u>GDOS INVESTIGATIONS</u> . . . . .	38
4.1. Emission Spectra . . . . .	38
4.2. Voltage and Pressure Effects . . . . .	43
4.3. Gas Impurity Effects . . . . .	48
4.4. Absorption Experiments . . . . .	51
5. <u>ATOMIC PROFILES</u> . . . . .	59
5.1. Sample Preparation . . . . .	60
5.2. Arsenic-Implanted Silicon . . . . .	66
5.3. Germanium-Implanted Gallium Arsenide . . . . .	70
5.4. Elemental Sensitivity . . . . .	75
6. <u>ELECTRICAL MEASUREMENTS</u> . . . . .	80
6.1. Measurement System . . . . .	80
6.2. Sample Preparation . . . . .	83
6.3. Arsenic-Implanted Silicon . . . . .	87
6.4. Germanium-Implanted Gallium Arsenide . . . . .	90
6.4.1. Sheet Resistance Measurements . . . . .	91
6.4.2. Depth Profiles . . . . .	95
6.4.3. Implanted Diodes . . . . .	96
6.5. Conclusions . . . . .	105

## 1. INTRODUCTION

The profiling of impurity distributions in ion-implanted semiconductors is a challenging task. The impurity concentrations involved in a typical implant are much lower than those associated with a thermal diffusion source [1]. In addition, the impurities are usually confined to a thin region (less than 1 micron) near the surface. Although the peak concentration of the impurity distribution may reach  $10^{20}$  atoms/cm<sup>3</sup>, the total number of implanted atoms is much less than is commonly encountered in diffusion layers. For example, a heavy dose arsenic implant into silicon may contain  $10^{15}$  atoms/cm<sup>3</sup>. This corresponds roughly to one monolayer of silicon atoms. Obviously, only extremely sensitive techniques are able to detect impurities in such small amounts.

In this work we have investigated the electrical and atomic (elemental) profiles of ion implanted semiconductors. The electrical measurements were performed using a double ac van der Pauw technique [2]. Glow Discharge Optical Spectroscopy [3] (GDOS) was used to obtain the elemental profiles. As an introduction, we shall consider in this section some of the important concepts of ion implantation, electrical measurements, and the elemental profiling techniques.

### 1.1. Ion Implantation

Although ion implantation has progressed from a research tool to a common method of semiconductor doping, not all of the problems associated with the technique have been solved. In particular, the implantation of large doses of heavy ions into silicon and the doping of compound semiconductors are areas of great interest.

The physical process of implantation is best described by the theory of Lindhard, Schiott, and Scharff (LSS) [4-6]. This theory assumes the incident ion energy is lost to the substrate by two independent mechanisms: the nuclear stopping power,  $S_N(E)$ , and the electronic stopping power  $S_E(E)$ . The energy lost per distance traveled can be expressed by

$$\frac{dE}{dx} = N[S_N(E) + S_E(E)] \quad (1.1)$$

where  $N$  is the density of substrate atoms. The ion comes to rest at a range  $R$  when it has lost all of its incident energy, where

$$R = \frac{1}{N} \int_0^E \frac{dE}{[S_N(E) + S_E(E)]} \quad (1.2)$$

The bulk of the LSS theory deals with predicting the two stopping powers and, in general, the values of  $S_N(E)$  are more accurate than those of  $S_E(E)$  [5,6]. The range is the total path length of the incident ion into the substrate. Experimentally, we can observe only the distance travelled perpendicular to the surface, the projected range  $R_p$ . Range statistics for a variety of ion and substrate combinations have been tabulated elsewhere [7].

Since the ions enter the sample at a variety of distances from the substrate atoms and they suffer collisions in a random fashion, the ions come to rest in some type of distribution about the projected range. The spread of the distribution is defined by the standard deviation (straggle),  $\sigma$ . As before, only the projected straggle ( $\sigma_p$ ) is experimentally observed. The implanted atom distribution can usually be approximated by a gaussian function, although more complex functions can be used



[7,8]. In this model, the concentration of atoms  $N(x)$  is given by

$$N(x) = N_p \exp \frac{-(x-R_p)^2}{2\sigma_p^2} \quad (1.3)$$

where  $N_p$  is the peak concentration. This peak is expressed by

$$N_p = \frac{0.4}{\sigma_p} N_D \quad (1.4)$$

where  $N_D$  is the fluence (dose) of the ions given in terms of atoms/cm<sup>2</sup>.

A major thrust of ion implantation research is the study of the implanted distribution and, more importantly, the consequences of the annealing steps which are required to remove the radiation damage induced by the incident ions. The most obvious effect of annealing is some diffusion of the atoms from the original implanted distribution. If the diffusion mechanisms are normal (i.e. no concentration dependent diffusion), the original profile will broaden symmetrically with anneal time. The spreading of a gaussian distribution is given by

$$N(x,t) = \frac{N_p}{\sqrt{1 + \frac{4\pi Dt}{2\sigma_p^2}}} \exp \frac{-(x-R_p)^2}{\frac{2\sigma_p^2}{1 + \frac{4\pi Dt}{2\sigma_p^2}} + 4Dt} \quad (1.5)$$

where  $D$  is the diffusivity of the species and  $t$  is the anneal time. Notice the effective straggle ( $e^{-1}$  point) of the distribution varies as

$$\sigma_p' = (\sigma_p^2 + 2Dt)^{1/2} . \quad (1.6)$$

We can estimate the diffusion coefficient of the species by comparing the straggles of the annealed and the original distributions where

$$D = \frac{\sigma_p'^2 - \sigma_p^2}{2t} . \quad (1.7)$$

### 1.2. Electrical Measurements

The ultimate goal of ion implantation in semiconductors is to alter the electrical properties in a useful and predictable fashion. Therefore, the most commonly used techniques for analyzing the implanted layer are electrical measurements. The four-point probe [9] is one of the simplest methods for determining the sheet resistance. Unfortunately, it yields no information about either the carrier concentration or mobility. A Hall [9] or van der Pauw [10] measurement does provide this information. The van der Pauw technique is preferred since it does not require a specialized geometry. When successive van der Pauw measurements are combined with layer removal (stripping), a profile of the carrier concentration and mobility can be obtained.

### 1.3. Atomic Measurements

Unfortunately, not all of the implanted atoms are electrically active after a typical implantation and anneal. Thus, some type of atomic or elemental impurity profiling must be used in conjunction with the electrical measurement to determine the behavior of the implanted species. While there are many different types of atomic measurements, they all involve the interaction between an incident particle (photon, electron, or ion) with the surface and the resulting emission of some type of characteristic particle. It seems that an atomic profiling scheme exists for almost every possible surface interaction [11-13]. The primary analytical tools available for analysis of semiconductors are Helium ion Backscattering (HBS) [14,15], Auger Electron Spectroscopy (AES) [15,16], Electron Spectroscopy for Chemical Analysis (ESCA) [17], and Secondary Ion Mass Spectroscopy

(SIMS) [16,18]. The limitations and advantages of these techniques have been reviewed elsewhere [12,13].

Probably the most sensitive technique for semiconductor analysis is SIMS. In this system, an incident ion beam produces sputtered ions from the substrate. These ions are mass analyzed and counted to produce concentration versus depth profiles. SIMS has been used to measure impurity concentrations as low as  $10^{15} \text{ cm}^{-3}$  [19]. However, SIMS suffers from quantization problems because of the strong matrix effects associated with the secondary ion production [19]. In addition, the SIMS equipment is highly complex and expensive and requires the use of ultra high vacuum.

The atomic profiles in this work were obtained by GDOS. The GDOS system involves the sputtering of a sample in a low pressure gas discharge and the subsequent excitation of the sputtered atoms in the discharge. The advantages of GDOS include reduced matrix effects (since the excitation occurs outside the sample) and the simplicity of the equipment. Since the actual events which occur during the GDOS process are complex, a discussion of gas discharges and sputtering phenomena is presented in Chapter 2. There was a considerable amount of experimentation needed before useful data could be obtained because GDOS is a relatively new technique. Some of these experiments and information are described in Chapter 4.



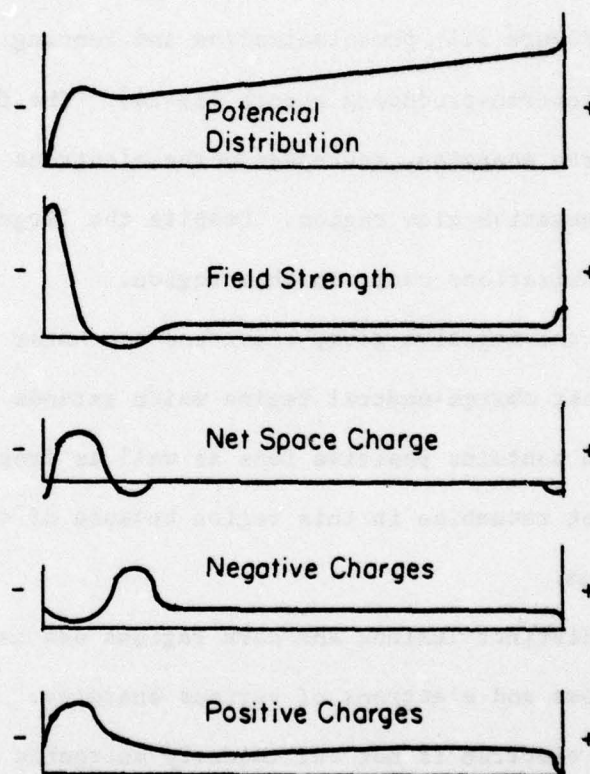
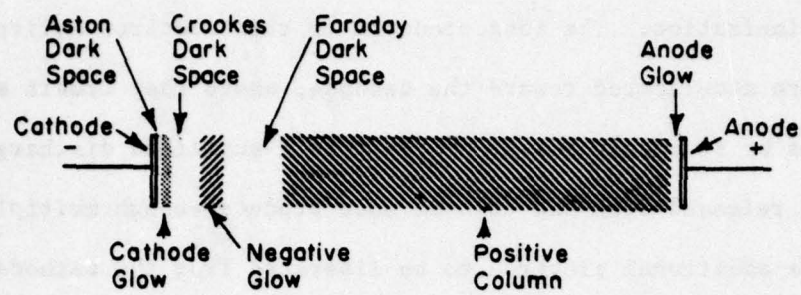
## 2. DISCHARGE AND SPUTTERING PHENOMENA

### 2.1. Gas Discharges

Gas discharges have been studied for many years with much of the initial work predating 1900. Discharges have been studied extensively, in part because they require only simple equipment to produce; yet some of the processes which occur in the discharge are complex and are still not adequately understood. A number of review articles and books [20-23] have covered the area of glow discharges and we shall consider here some of the fundamental processes which influence the cathode sputtering phenomena.

The discharge characteristics are controlled primarily by the events which occur near the cathode. In brief, ionized particles striking the cathode can liberate secondary electrons from the surface. These electrons are accelerated across a space charge region near the cathode and produce ionizing collisions with gas atoms. These ions then are accelerated back toward the cathode where they can produce more secondary electrons; and thus the discharge is maintained.

A dc discharge has several distinct regions, as shown in Figure 2.1. The various regions are best understood by following the path of an electron through the discharge. An electron emitted from the cathode first encounters a strong electric field in the space charge region near the cathode. The electron makes many collisions throughout its path, but initially it cannot ionize gas atoms because of its low energy. As it moves further away from the cathode the electron gains sufficient energy from the electric field to ionize the gas. Electrons generated by ioni-



KP-1423

Fig. 2.1. The regions of a dc glow discharge.



zation in the space charge region are in turn accelerated and produce further ionization. The ions produced in this electron multiplication region are accelerated toward the cathode, where they create additional electrons by secondary emission. In a self-sustained discharge, each electron released from the cathode must produce enough multiplication to cause one additional electron to be liberated from the cathode. While most of the ionization occurs via electron collisions in the Crooks dark space region (Figure 2.1), photoionization and Penning ionization can also be important electron-producing events [21-24]. The field strength, and thus the electron energies, decreases as the electrons leave the dark space and enter the negative glow region. Despite the large number of electrons present, few ionizations occur in this region.

From the negative glow, electrons can enter the positive column; this is an almost charge-neutral region which extends to the anode. The positive column contains positive ions as well as free electrons, but these particles do not recombine in this region because of their large difference in momentum.

The distinct luminous and dark regions are caused by collisions between gas atoms and electrons of various energies. Near the surface of the cathode an electron is not sufficiently energetic to excite or ionize a gas atom; this gives rise to the Aston dark space in Figure 2.1. In the cathode glow region the electrons have sufficient energy to excite the gas, resulting in light emission. Farther from the cathode, in the Crooks dark space, the electron energies are well above the excitation potential maximum, and thus ionization occurs with little light emission. Near the end of the space charge region, there are large numbers of secondary electrons

which have been generated by the multiplication events. These electrons in general do not ionize the gas, but they do excite atoms in the negative glow region.

At low voltages the glow region usually does not occupy the entire area of the cathode. The glow tends to maintain a constant current density near the cathode, thus the area it occupies depends on the applied power in their so-called normal glow regime. The voltage across the space charge region (cathode fall voltage) is also a constant, determined by the discharge gas and the cathode material.

The area of the glow increases if more power is applied, until the entire cathode surface is covered. The current density then must increase if additional power is added. This implies that the secondary electron emission and therefore the cathode fall voltage also increase at high power densities. This type of discharge is known as an abnormal glow, and almost all discharge sputtering is performed in this mode.

In a normal glow, it is found experimentally that the product of the gas pressure  $p$  and the dark space thickness  $d$  is a constant [22].

$$pd = \text{constant} \quad (2.1)$$

This constant is determined by the discharge gas and the cathode material. Early experimenters used this relationship to estimate the gas pressure in the discharge chamber.

In an abnormal glow, however, the dark space thickness is also a function of the applied power. The thickness of the dark space region is usually described by Aston's equation [20].

$$d = \frac{A}{p} + \frac{B}{\sqrt{j}} \quad (2.2)$$

The cathode fall voltage  $V$  is also a function of the pressure and the current density  $j$

$$V = E + \frac{F\sqrt{j}}{p} \quad (2.3)$$

where  $A$ ,  $B$ ,  $E$ , and  $F$  are experimentally determined constants. We see that the cathode fall voltage increases with increasing current density and decreases with pressure. This dependence on current density allows cathodes of different areas to have different cathode fall voltages for identical discharge parameters. Thus the cathode design is critical when studying the sputtering behavior in discharges.

## 2.2. Sputtering

The bombardment of the cathode by ions not only produces the secondary electrons needed to sustain the discharge, but it can also erode the cathode by sputtering. Cathode sputtering was first observed in a gas discharge in 1852 [25] and has been widely used for the deposition of thin metal films [26,27]. However, in this work we are more interested in the sputtering mechanisms itself rather than the deposition process.

Sputtering is the ejection of material from a target induced by an impinging energetic particle, usually an ion. It was at first thought to be an evaporation phenomenon [28,29] related to the localized heating of the target induced by the impact energy of the bombarding ion. Sputtering is now widely recognized to be a collisional momentum transfer process similar, as Wehner states, "to playing billards with atoms" [28]. Consider a classical hard sphere collision in which a incident particle collides with a second particle initially at rest. The two particles divide the initial energy according to their masses and are directed with individual



final velocities in separate directions. We recall from conservation of energy and momentum that the angle between the two final velocities cannot be greater than  $180^\circ$ . Thus, at least two collisions are required to transfer the momentum of an incident ion to a target atom having momentum directed away from the surface, as seen in Figure 2.2. The ion's initial energy is lost to the target through collisions which produce target heating and the ion eventually becomes embedded in the target.

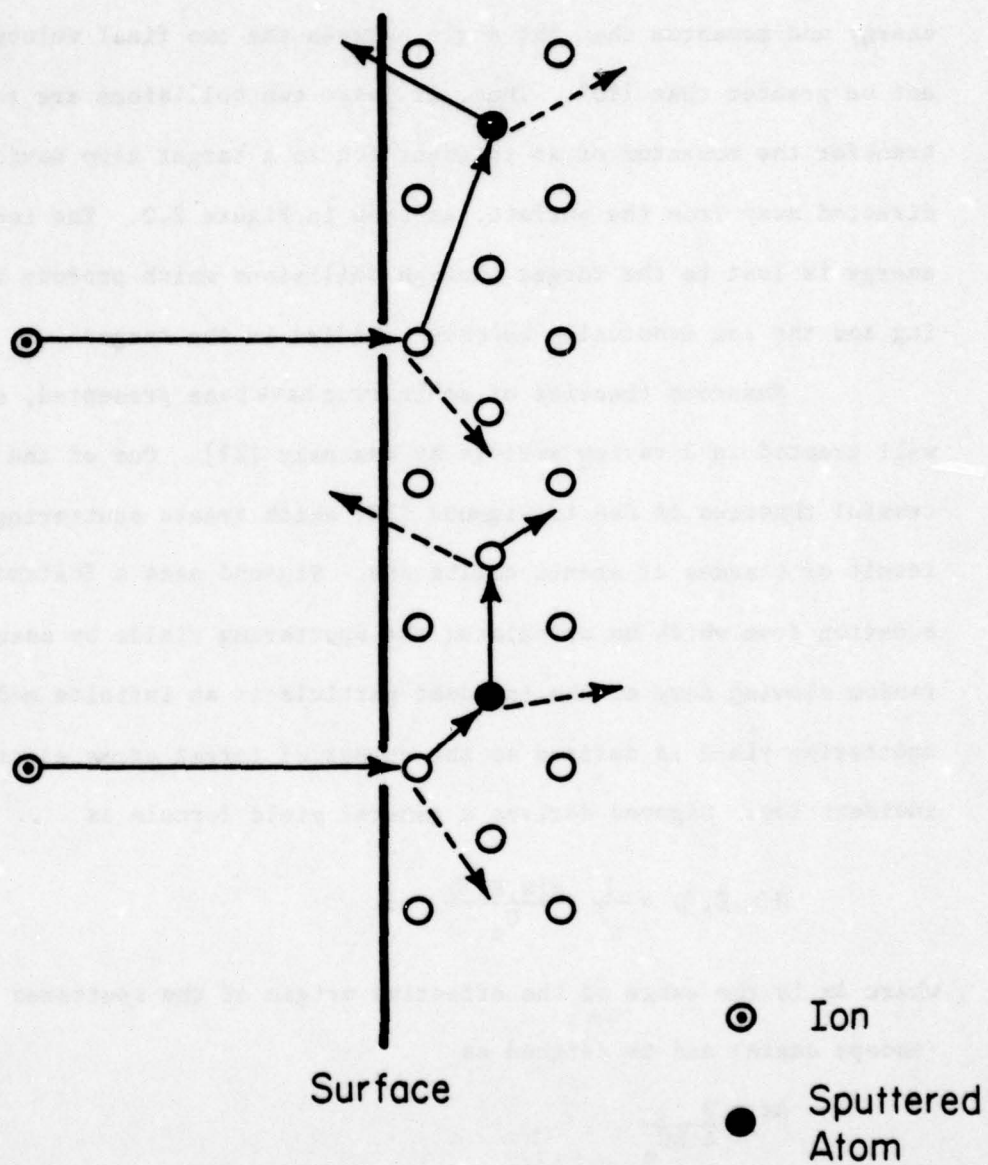
Numerous theories of sputtering have been presented, and they are well treated in a review article by Kaminsky [29]. One of the more successful theories is due to Sigmund [30] which treats sputtering as the result of cascades of atomic collisions. Sigmund uses a Boltzman transport equation from which he calculates the sputtering yields by assuming the random slowing down of the incident particle in an infinite medium. The sputtering yield is defined as the number of target atoms ejected per incident ion. Sigmund derives a general yield formula as

$$H(x, E, \eta) = \frac{1}{\pi^2} \frac{F(x, E, \eta)}{U_0} \Delta x \quad (2.4)$$

where  $\Delta x$  is the range of the effective origin of the sputtered atoms (escape depth) and is defined as

$$\Delta x = \frac{3}{4} \frac{1}{NC_0} \quad (2.5)$$

Using Sigmund's notation  $N$  is the density of target atoms,  $E$  is the energy of the incident ion,  $x$  is the distance measured from the surface of the target,  $\eta$  is the projected velocity of the ion normal to the surface,  $U_0$  is the binding energy of a target atom,  $C_0$  is a constant related to the scattering cross section of the target, and  $F(x, E, \eta)$  is defined as the



LP-1460

Fig. 2.2. Two possible sequences for sputtering by multiple collisions.

depth distribution of the energy lost by the incident ion to the target by any mechanism.

By assuming an isotropic medium and a low ion energy ( $E < 1$  reV), the yield can be approximated by

$$S(E) = \frac{3}{4\pi^2} \frac{\alpha}{C_o U_o} S_N(E) \quad (2.6)$$

The constant  $\alpha$  is a function of the ion to target atom mass ratio and is plotted as a graph by Sigmund. The energy loss mechanism is assumed to be described by a nuclear stopping power  $S_N(E)$  which has been tabulated by Lindhard [4] and Gibbons [7].

Sigmund's theory allows us to estimate the yield from an amorphous target if the proper target characteristic are known. The yield values obtained agree quite well with experimental values, considering the number of assumptions which must be made. One of the most difficult parameters to predict is the atomic binding energy  $U_o$ , which is influenced by the cohesive binding energy of neighboring atoms as well as any binding due to conduction band electrons [30]. Thus the phase of the target (e.g. amorphous or crystalline) can directly effect the sputtering yield. Also, since sputtering is a collisional process, one could expect crystal orientation to modify the yield as compared to a simple amorphous target.

Some of the strongest evidence that sputtering is not an evaporation process was provided by the dramatic differences between the sputtering of amorphous and crystalline targets. The spatial distribution of evaporated particles should follow a cosine distribution [28,29]. However, Wehner measured a "sub-cosine" distribution from amorphous targets bombarded at normal incidence [31] as in Figure 2.3(a). A cosine distribution



could appear as a circle just touching the origin in this polar graph. The distribution of sputtered atoms also changed when the angle of incidence was varied as in Figure 2.3(b). Anderson observed that the ejection of target atoms from crystals tends to follow along the close packed directions of the lattice [32]. This led some observers to speculate on the existence of long focusing chains of collisions called "focusons" which caused sputtering along specific crystal directions [33]. Focusons are now generally considered to be only a second order effect in the total sputtering process. The important collisions which lead to sputtering usually occur within the first two or three monolayers of the surface. Thus we can expect the sputtering rates for different orientations of the same crystal to vary as a consequence of the different packing densities of the various directions.

Another consequence of the collisional nature of sputtering is the variation of yield with the incident angle of the ion. For most targets the yield increases as the incidence angle becomes greater with respect to the surface normal [28,29]. At angles oblique to the surface fewer collisions are required to give target atoms momentum directed away from the surface. The sputtering yield drops at grazing incidence since there is a high probability of the ion simply reflecting off the surface.

The sputtering yield is found experimentally to be a function of the ion-target mass ratio, the ion energy, the structure of the target, and the angle of incidence of the ion. Thus, there is a wide variation of reported yields caused by the inevitable differences in experimental conditions. Yield data may be found in several review articles [34,35] and an example of such data is presented in Table 2.1. We observed in

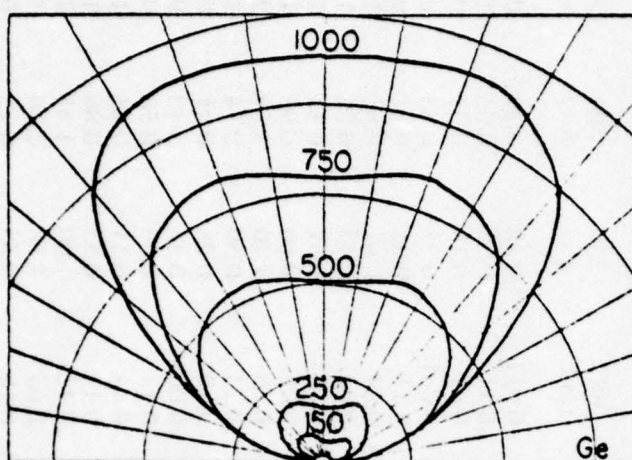


Fig. 2.3a. Angular distribution of sputtered germanium [31]. The incident argon ion beam was normal to the substrate with ion energies ranging from 150 to 1000 eV.

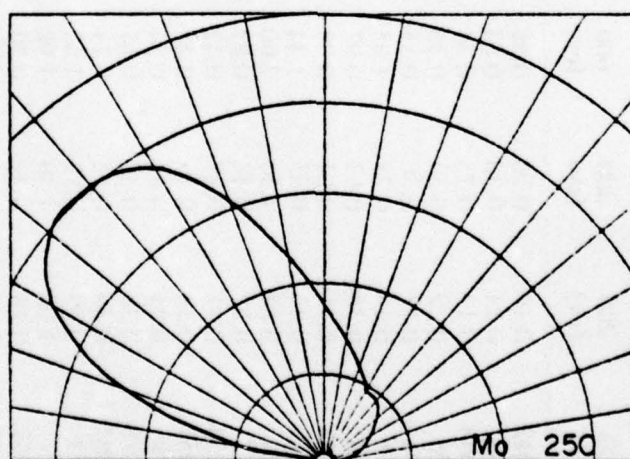


Fig. 2.3b. Angular distribution of sputtered Mo [31]. The 250 eV incident argon ions were directed from the right at an angle of  $45^\circ$  to the substrate.



Table 2.1. Sputtering yields of 28 elements under neon and argon bombardments [35].

Target	Neon				Argon			
	Yield at lowest ion energy							
	100 (ev)	200 (ev)	300 (ev)	600 (ev)	100 (ev)	200 (ev)	300 (ev)	600 (ev)
Be	0.012	0.10	0.26	0.56	0.05	80	0.074	0.80
Al	0.031	0.24	0.43	0.83	0.11	100	0.11	1.24
Si	0.034	0.13	0.25	0.54	0.06	80	0.07	0.53
Ti	0.08	0.22	0.30	0.45	0.081	100	0.081	0.58
V	0.06	0.17	0.36	0.55	0.03	60	0.11	0.70
Cr	0.18	0.49	0.73	1.05	0.026	40	0.30	1.30
Fe	0.18	0.38	0.62	0.97	0.064	60	0.20	1.26
Co	0.084	0.41	0.64	0.99	0.048	60	0.15	1.36
Ni	0.22	0.46	0.65	1.34	0.067	60	0.28	1.52
Cu	0.26	0.84	1.20	2.00	0.10	60	0.48	2.30
Ge	0.12	0.32	0.48	0.82	0.017	30	0.22	1.22
Zr	0.054	0.17	0.27	0.42	0.027	60	0.12	0.75
Nb	0.051	0.16	0.23	0.42	0.017	60	0.068	0.65
Mo	0.10	0.24	0.34	0.54	0.027	60	0.13	0.93
Ru	0.078	0.26	0.38	0.67	0.012	60	0.14	1.30
Rh	0.081	0.36	0.52	0.77	0.19	100	0.19	1.46
Pd	0.14	0.59	0.82	1.32	0.033	50	0.42	2.39
Ag	0.27	1.00	1.30	1.98	0.22	60	0.63	3.40
Hf	0.057	0.15	0.22	0.39	0.004	40	0.16	0.83
Ta	0.056	0.13	0.18	0.30	0.01	60	0.10	0.62
W	0.038	0.13	0.18	0.32	0.008	60	0.068	0.62
Re	0.04	0.15	0.24	0.42	0.034	80	0.10	0.91
Os	0.032	0.16	0.24	0.41	0.057	100	0.057	0.95
Ir	0.069	0.21	0.30	0.46	0.019	60	0.12	1.17
Pt	0.12	0.31	0.44	0.70	0.032	60	0.20	1.56
Au	0.20	0.56	0.84	1.18	0.035	50	0.32	2.43 (500)
Th	0.028	0.11	0.17	0.36	0.017	60	0.097	0.66
U	0.063	0.20	0.30	0.52	0.14	100	0.14	0.97

equation 2.6 that the yield should vary linearly with the stopping power of the target. This implies that heavy atoms should sputter more readily than light ones. Indeed as seen in Table 2.1 the yield for beryllium is  $\sim 3$  times less than that of copper for bombardment with 600eV argon ions. However, the sputtering yield does not increase monotonically with atomic number, as Figure 2.4 indicates. The periodicity which is related to the filling of electron shells is apparent in this diagram.

Above some sputtering threshold energy the yield increases with ion energy until a constant yield plateau is reached [28,29]. At very high energies the yield drops, since the collisions are occurring deeper in the target whereas the displaced atoms can escape only near the surface. This is exactly the process which occurs during ion implantation.

A particle ejected in the sputtering process leaves the surface with a velocity much greater than that of an evaporated atom [27]. Figure 2.5 shows that the typical range of particle energies is under 20eV and is not a strong function of the incident ion energy. While it is well known that the sputtered particles are primarily neutral atoms, a small fraction of the material leaves the surface as excited neutrals, ions, and in clusters [36-38]. The secondary ion yield depends on many variables, including the surface composition and the ion energy. The yields of positive secondary ions are generally higher for insulators as compared to metals on semiconductors [19]. One method used in SIMS profiling is to sputter with an oxygen beam which creates a very thin oxide region on the surface, thus enhancing the ion yield [19].

So far we have only considered the sputtering of a target compound of a single element; naturally, alloy sputtering is even more compli-

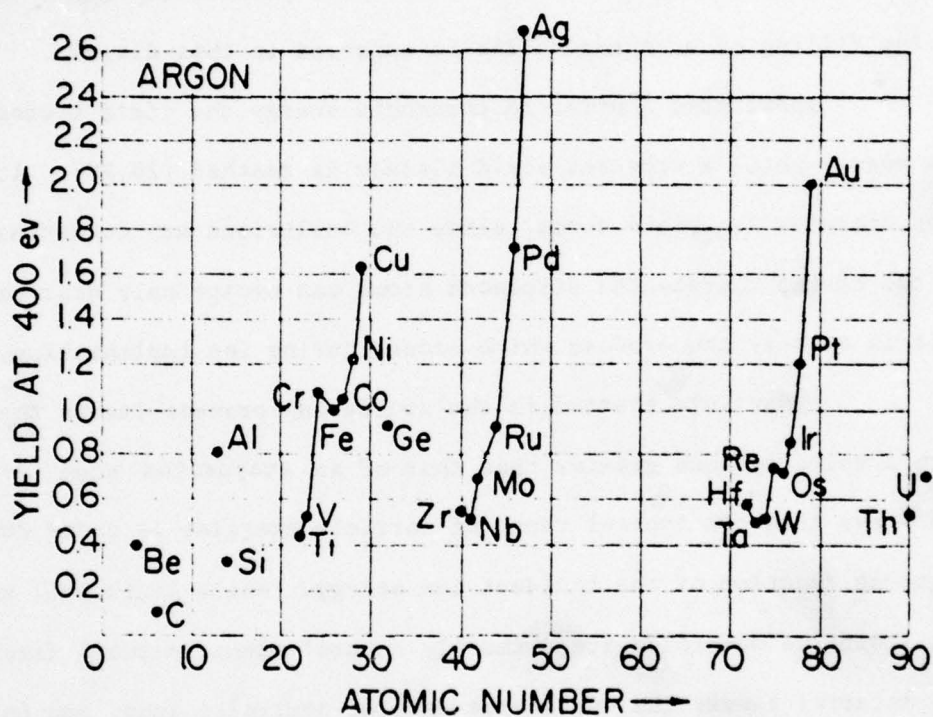


Fig. 2.4. Sputtering yield of 28 elements under 400 eV argon bombardment as a function of atomic number [35].



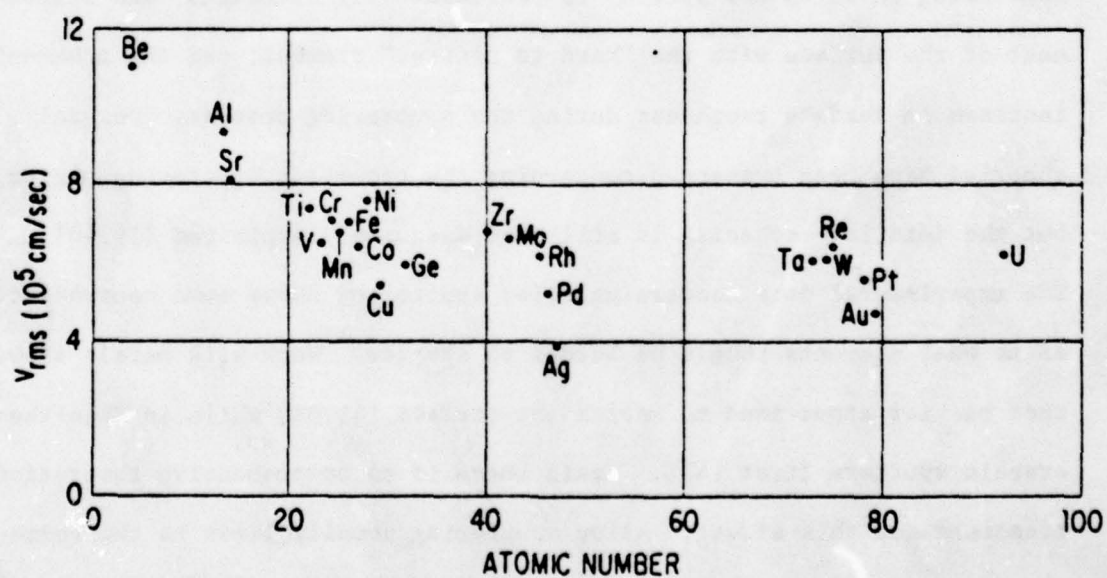
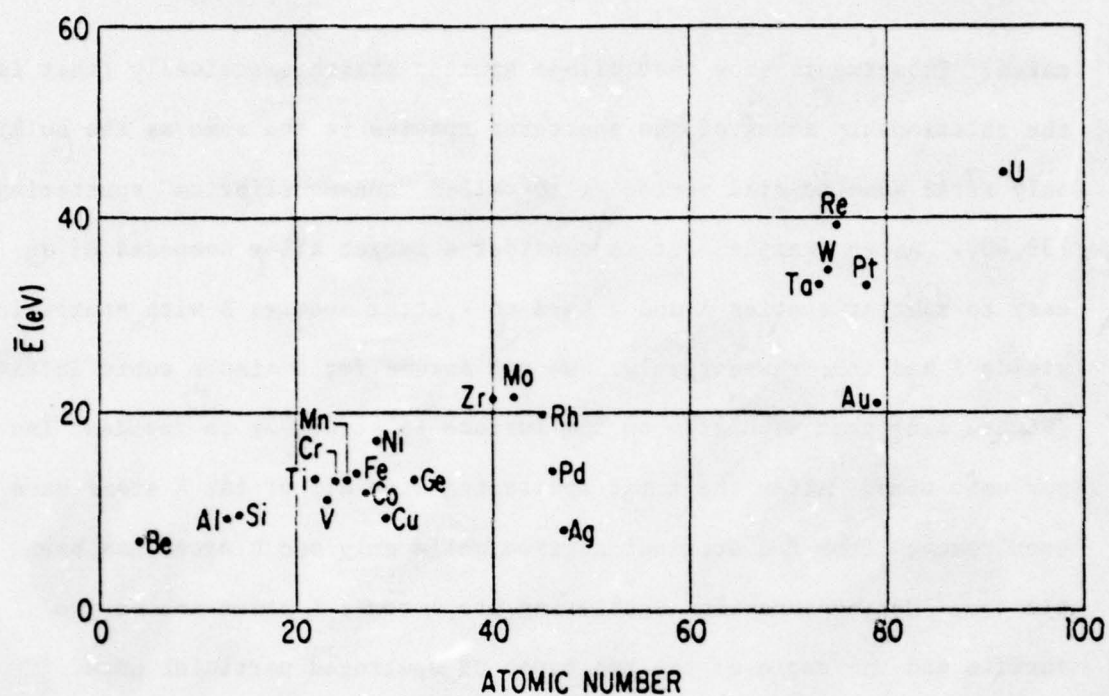


Fig. 2.5. Average ejection energies and velocities of sputtered elements with 400 eV argon ion bombardment [28].

cated. Experiments show that alloys sputter stoichiometrically (that is, the relationship among of the sputtered species is the same as the bulk) only after some initial period of so-called "non-equilibrium" sputtering [39,40]. As an example, let us consider a target alloy composed of an easy to sputter species A and a hard to sputter species B with sputtering yields 1 and  $1/3$ , respectively. We can assume for a simple cubic lattice (Figure 2.6) that each atom on the surface is struck by an incident ion per unit time. After the first sputtering step all of the A atoms have been removed from the original surface while only one B atoms has been ejected. During successive sputtering steps fewer A atoms are on the surface and the ratio of the two types of sputtered particles more closely matches the composition of the target.

Although this model is over simplified, it presents the important features of alloy sputtering: an initial period of non-equilibrium sputtering in which one species is preferentially sputtered; the enrichment of the surface with the "hard to sputter" element; and the inherent increase in surface roughness during the sputtering process. Several theories have been presented concerning the transient sputtering period, but the detailed mechanism is still not adequately explained [39,40]. The experimental data concerning alloy sputtering shows some contradiction as to what elements should be harder to sputter. Work with metals shows that heavier atoms tend to enrich the surface [41,42] while in GaAs the arsenic sputters first [43]. Again there is no comprehensive theoretical treatment for this effect. Alloy sputtering usually leads to the formation of surface irregularities or cones as the easily sputtered species are removed [43-45].

A	B	A	B	A	B	A	B
B	A	B	A	B	A	B	A
A	B	A	B	A	B	A	B
B	A	B	A	B	A	B	A
A	B	A	B	A	B	A	B

Original Surface

	B				B		B
B	A	B	A	B	A	B	A
A	B	A	B	A	B	A	B
B	A	B	A	B	A	B	A
A	B	A	B	A	B	A	B

After 1 Step

	B				B		
B	A	B			A	B	A
A	B	A	B	A	B	A	B
B	A	B	A	B	A	B	A
A	B	A	B	A	B	A	B

After 2 Steps

					B		
B	A				A	B	
A	B	A	B		B	A	B
B	A	B	A	B	A	B	A
A	B	A	B	A	B	A	B

After 3 Steps

LP-1456

Fig. 2.6. Simplified model of alloy sputtering. The easy to sputter species (A) has a sputtering yield of 1 while the hard to sputter species (B) has a yield of  $1/3$ .



### 2.3. Sputtering in a Glow Discharge

Sputtering was first observed in a glow discharge [25] and, until recently, most of the subsequent research was performed with the discharge method. However, glow discharges are highly unsuited for quantitative studies of the sputtering process. The fundamental problem is that the pressure required for a self sustained discharge is so high that both the gas atoms and the sputtered particles have mean free paths smaller than the dimension of the discharge tube. Thus before a sputtered atom can deposit on the walls it undergoes multiple collisions with gas atoms. Such collisions can excite or ionize the particle, or even reflect it back toward the cathode. As Kaminsky points out, these collisions make it impossible to obtain information on the various parameters involved with the sputtering process [29].

Ions produced in the glow region arrive at the cathode with a wide range of energies, various charge states, and with different angles of incidence due to the collisions in the cathode fall region. Experiments measuring the actual distribution of ion energies arriving at the cathode show that more than half of the ions have energies less than 20% of the cathode fall energy [46], as in Figure 2.7. Essentially no ions arrive with the full cathode fall energy because of the collisions in the Crooks dark space. Thus, the incident ion energy is a function of the pressure as well as the applied voltage.

At high pressures the sputtered atoms may lose all of their initial energy through collisions and never reach the walls of the chamber. Laegrid and Wehner [35] estimate that only 10% of the sputtered atoms are actually deposited at pressures above 100 mTorr (Figure 2.8). The

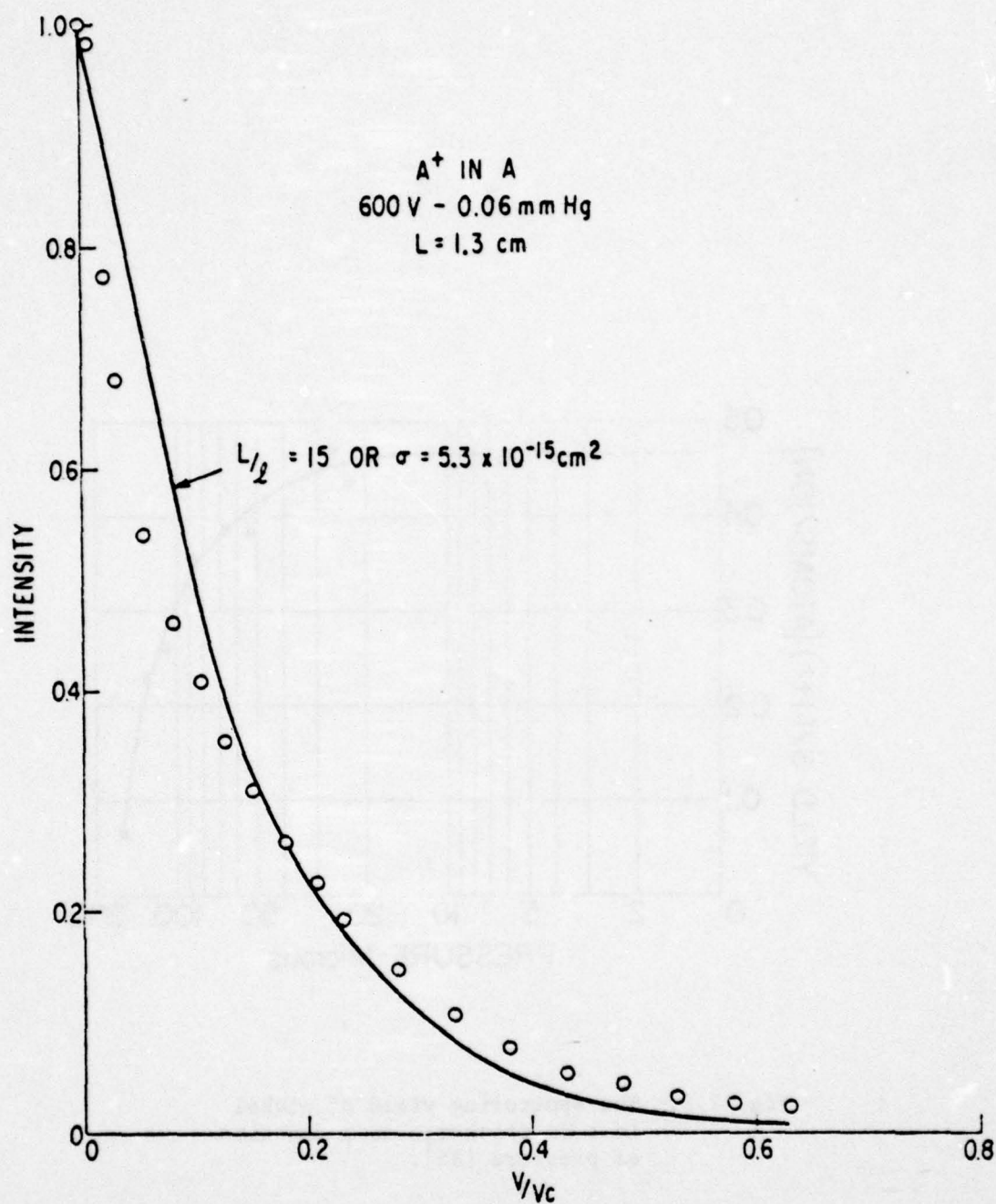


Fig. 2.7. The energy distribution of argon ions arriving at the cathode in a glow discharge [46]. The dark space distance ( $L$ ) is 1.3 cm with an applied voltage ( $V_c$ ) of 600 v.



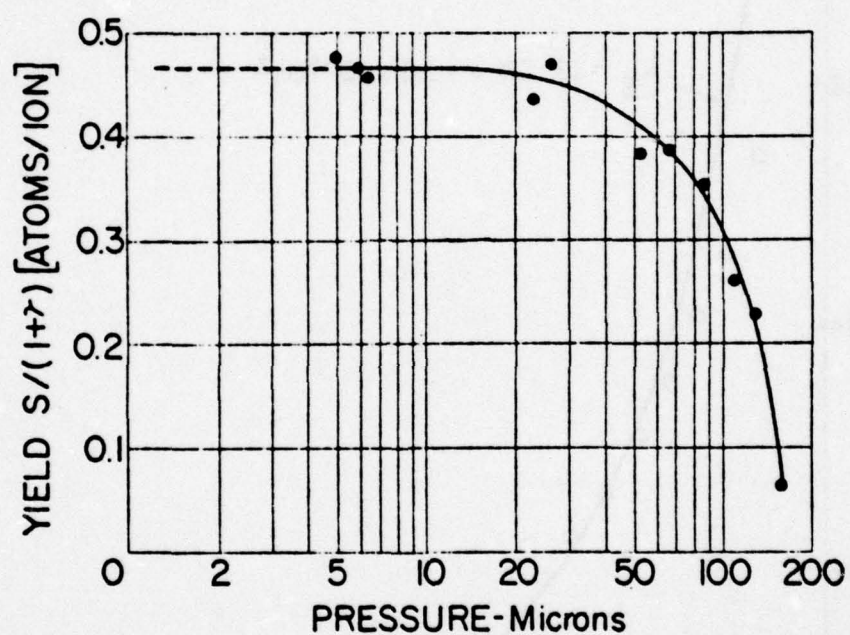


Fig. 2.8. The sputtering yield of nickel in a dc discharge as a function of pressure [35].

remaining atoms stay in the discharge where they can be ionized or deposited on the target itself.

Another problem is that the secondary electron emission is a function of the incident ion energy and also of the target composition. Because there is no way of measuring the secondary emission, the current through the discharge cannot be used to estimate the number of incident ions.

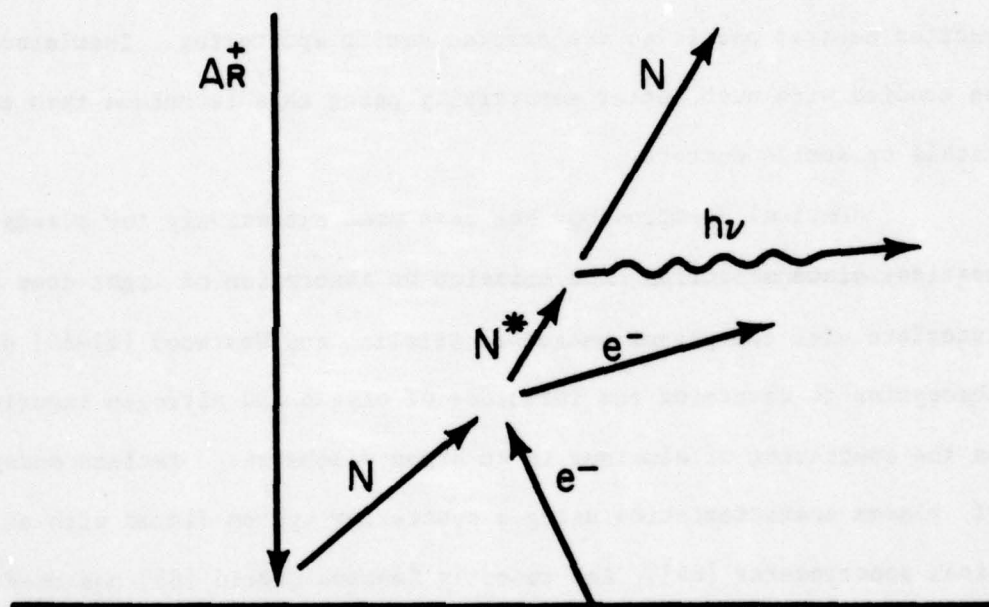
### 3. GLOW DISCHARGE OPTICAL SPECTROSCOPY

GDOS has recently been used to determine the composition of thin films [3,47], solids [48,49], and ion implanted layers [50-52]. In GDOS, a sample is placed on the cathode of a low pressure discharge and is slowly eroded by cathode sputtering. The ejected material leaves primarily as neutral atoms, which are subsequently excited by electron collisions in the cathode glow region of the discharge and emit photons of characteristic wavelengths as illustrated in Figure 3.1. The intensity of a given emission line in the resulting spectrum has been shown to be proportional to the concentration of the corresponding element in the cathode [3,47]. When combined with an independent measurement of the sputtering rate, monitoring the intensity of a single emission line as a function of time yields a profile for the element as a function of depth. This method has been used successfully for a number of different elements and, in principle, any element could be profiled.

#### 3.1. Optical Spectroscopy

Since 1926, when von Hippel [53] first observed the light emission from the sputtered particles in a discharge, there have been numerous applications of optical spectroscopy in sputtering and plasma research. In a triode system very similar to GDOS, Stuart and Wehner [54,55] used the emission from sputtered neutrals in a low pressure plasma to measure the yields and sputtering threshold energies of various elements. They found the intensity of an atomic emission line to be proportional to the sputtering yield of the element. In related work, Ratinen [56] measured the sputtering rate of insulators in a rf discharge using emission spectroscopy. A recent application by Lu [57] uses the emission intensity to





LP-1157

Fig. 3.1. Sputtering and excitation processes near the cathode. The collision of sputtered neutrals ( $N$ ) with electrons create excited neutrals ( $N^*$ ) which emit light of characteristic wavelengths

measure the sputtering rate in a deposition rate control system.

Sawatzky and Kay [58] tried to eliminate the uncertain nature of a self-sustained discharge in another emission spectroscopy experiment. They bombarded the sample with an ion beam and used a separate low energy electron beam to excite the sputtered atoms. They found the resultant light emission again to be proportional to the sputtering yield. Tolk et al. [59,68] using an ion beam discovered that sputtered atoms emit light without external excitation. Analogous to the SIMS process, excited neutral particles are emitted during sputtering. Insulators can be studied with much better sensitivity using this technique than either metals or semiconductors.

Optical Spectroscopy has been used extensively for plasma diagnostics, since measuring the emission or absorption of light does not interfere with the plasma behavior. Stirling and Westwood [61-63] used atomic absorption to determine the influence of oxygen and nitrogen impurities on the sputtering of aluminum in an argon discharge. Ratinen measured rf plasma characteristics using a sputtering system fitted with an optical spectrometer [64]. And recently Sequeda-Osorio [65] has used GDOS to characterize sputtering behavior in diode and triode systems.

### 3.2. Light Emission Characteristics

Sputtered atoms are ejected as neutrals into the plasma where they undergo excitation, and subsequently emit light of characteristic wavelengths in emission spectroscopy. However, the details of the excitation process are not known and there is no comprehensive theoretical treatment of these phenomena. The excitation process is believed to be

dominated by collisions with energetic electrons [3,47]. Thus, we would expect the most intense light emission regions to be located where high concentrations of electrons of proper energies coincide with sputtered neutrals. Measurements of the light distribution from sputtered atoms [65] show the maximum intensity occurs near the cathode (Figure 3.2). In this region, just as we observed for gas atoms in the discharge, the electrons have sufficient energies to excite the sputtered atoms. Farther into the Crooks dark space, the electron energies are too high to efficiently excite the atoms, and hence the emission intensity decreases. A second emission maximum is located near the negative glow region. There are large numbers of low energy electrons available for excitation in this region; however, the sputtered atom density and therefore the emission is not as great as it is near the cathode. It is not known if a single atom undergoes multiple excitations in the discharge or if only one photon is emitted for each sputtered atom.

GDOS does not appear to suffer the severe matrix effects which are present in other atomic profiling techniques [48,49], since the excitation of the atoms occurs away from the sample and there is only weak interaction between the sputtered particles in the discharge. However, the nature of the self-sustained discharge would indicate that some matrix effects should be observed. The emission process is determined by the sputtering rate and the density of electrons available for excitation. Because of the complex interactions between the incident ion energy, the secondary electron emission, and the sputtering yield, we should expect some variation in the excitation efficiency of atoms sputtered from different targets. Specifically, the sensitivity for atoms



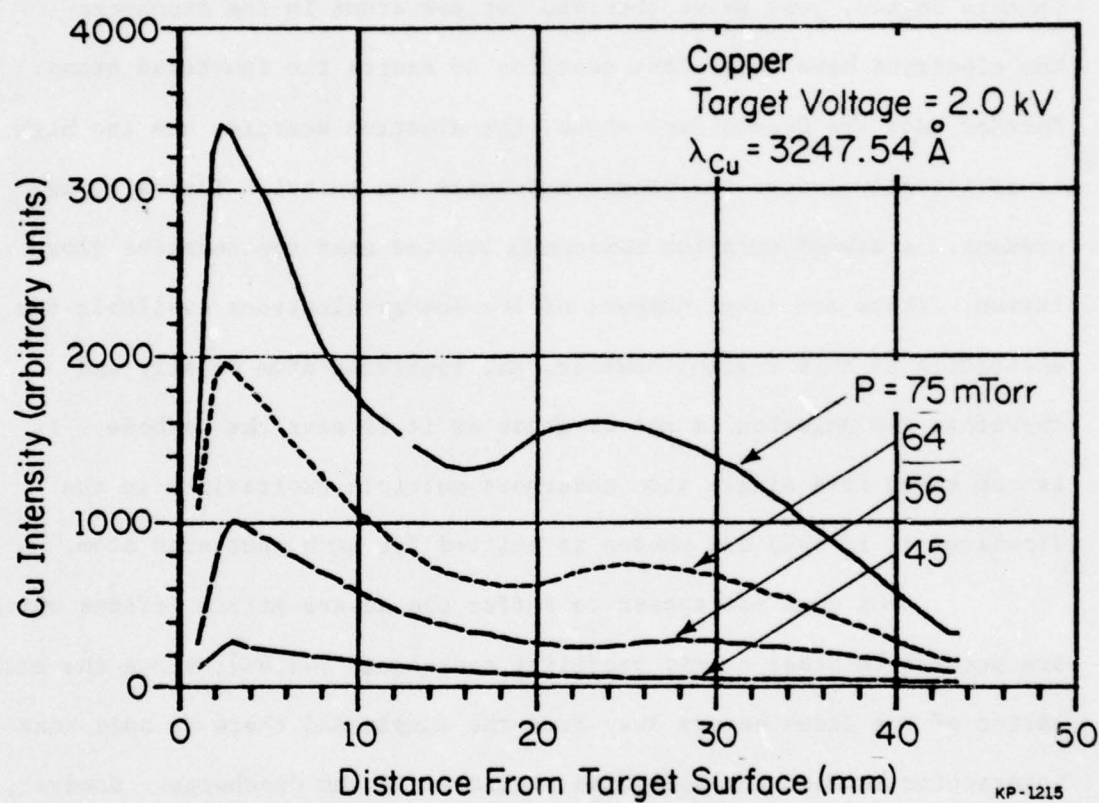


Fig. 3.2. The distribution of emitted light from sputtered copper atoms in a dc discharge [65].

sputtered from metals and semiconductors could vary considerably because of the different binding mechanisms of the atoms and electrons.

The use of GDOS as an analytical profiling technique depends on the relationship between the sputtered atoms and the resulting emission. Measurements have shown that for constant discharge parameters the emission intensity is proportional to the elemental concentration. However, the important features such as sputtering rate, emission intensity, and elemental sensitivity cannot be predicted. Thus, the GDOS technique remains subject to a number of standardizations and calibrations.

### 3.3. Experimental Apparatus

The GDOS system used in these experiments consists of a discharge chamber designed for uniform sputtering of the sample and two separate light collection subsystems as seen in Figure 3.3. One light collection subsystem (labeled as the substrate monitor) is used to examine the sputtering of the substrate for uniformity and reproducibility. When sputtering GaAs, for example, we monitor the emission of the strong  $4172 \text{ \AA}$  gallium line as a function of time. Measuring this light emission is quite easy since we are dealing with a major constituent of the sample. A uv sensitive photomultiplier tube (EMI 6256S) collects the output from the  $3/4$  meter spectrometer (SPEX 1702) which contains a grating ruled with a 1200 lines per mm and blazed at  $3000 \text{ \AA}$ . The electrical output is detected by the lock-in amplifier (PAR HR-8), which is tuned to the frequency of the chopped light. The amplifier output is proportional to the intensity and is plotted versus time or wavelength on a strip chart recorder.

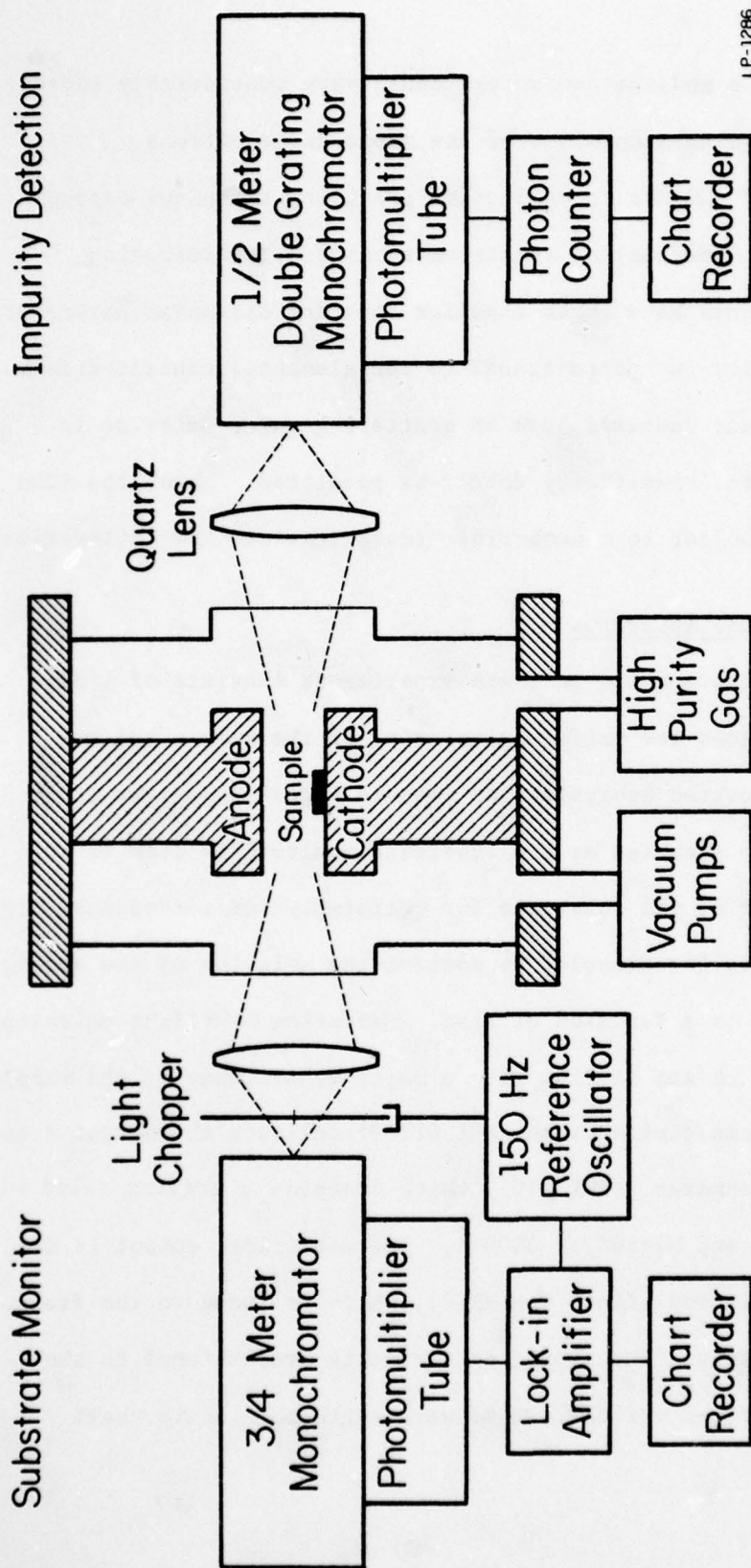


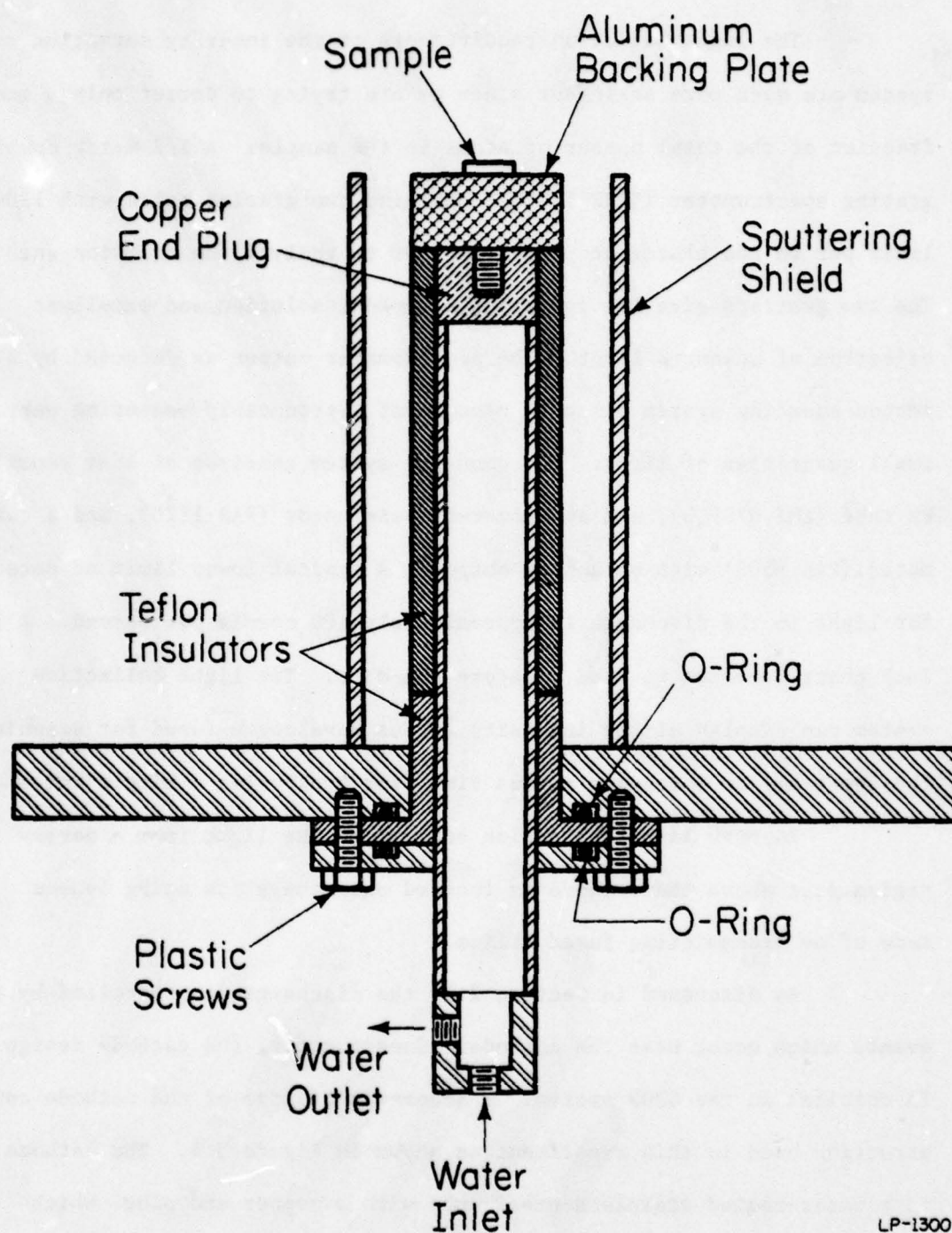
Fig. 3.3. Schematic diagram of the GDOS system used in this work.



The light detection requirements of the impurity detection subsystem are much more stringent since we are trying to detect only a small fraction of the total number of atoms in the sample. A 1/2 meter double grating spectrometer (SPEX 1302) containing two gratings ruled with 1200 lines per mm and blazed at  $3000 \text{ \AA}$  is used to analyze the emission spectrum. The two gratings give the spectrometer good resolution and excellent rejection of unwanted light. The spectrometer output is detected by a photon counting system which is capable of reproducibly measuring very small quantities of light. The counting system consists of a uv sensitive PM tube (EMI 9789QB), and amplifier-discriminator (PAR 1120), and a rate-meter (PAR 1105) with an analog output. A typical lower limit of detection for light in the discharge is approximately 100 counts per second. A 10 inch chart recorder is used to store the data. The light collection system can display either intensity versus wavelength (used for scanning the spectrum) or intensity versus time (for monitoring a single emission line).

In both light collection subsystems the light from a narrow region just above the cathode is focused onto the slits using lenses made of uv transmitting fused silica.

As discussed in Section 2.1, the discharge is controlled by the events which occur near the cathode. Consequently, the cathode design is critical in the GDOS system. A schematic diagram of the cathode construction used in this experiment is shown in Figure 3.4. The cathode is a water-cooled stainless-steel tube with a copper end plug, which allows good heat conduction. The sample is mounted onto a removable sample holder which is in turn screwed into the end plug. The cathode assembly is at an applied negative voltage with respect to the rest of the chamber, which is kept grounded. A stainless



LP-1300

Fig. 3.4. Design of the water-cooled cathode. The cathode is electrically isolated from the flange by Teflon insulators and plastic screws.

steel cylinder placed around the cathode acts as a sputtering shield to prevent unwanted sputtering of the cathode structure. The grounded shield is placed closer than the dark space distance from the cathode; thus, no discharge can be maintained in the region between the shield and the cathode. Therefore, only the top surface of the sample holder is actually sputtered in this configuration. Since both the sample and the sample holder are sputtered during the measurement, we chose to make the holder out of high-density graphite. Graphite has an extremely slow sputtering rate (as seen in Table 2.1), it can be obtained in ultra high purity, is easily machined, and the carbon emission lines do not interfere with the measurements.

The samples were mounted onto the holder using a silver-based conducting micropaint. Only small amounts of paint were used and the paint was never exposed to the discharge. The samples were generally less than  $1 \text{ cm}^{-2}$  in area; thus, we have a small sample mounted onto a larger flat surface. This helps keep the sample in a uniform field region and insures even sputtering across the face of the sample. After sputtering, the sample was removed from the holder using acetone, and the holder was cleaned in a hot solution of hydrogen peroxide and ammonium hydroxide.

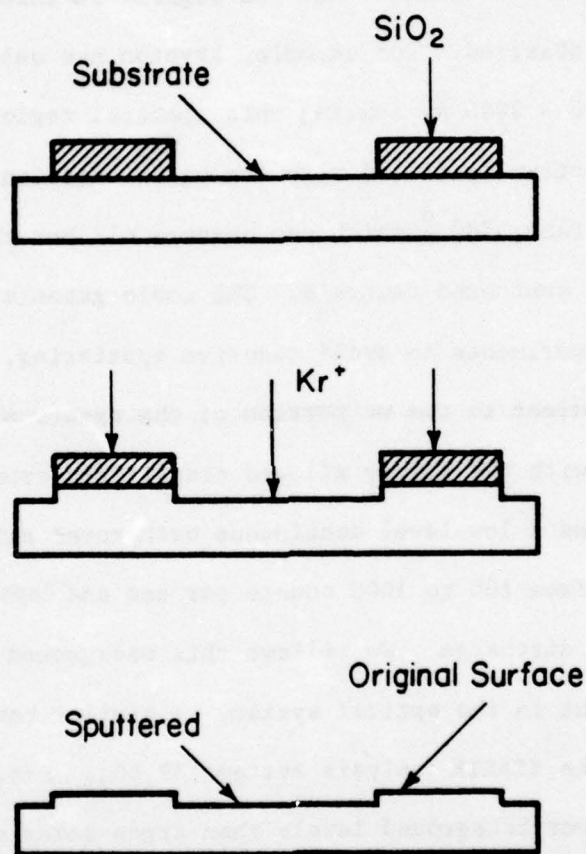
In preparation for a GDOS run, the sample is cleaned and mounted onto the holder and allowed to dry in a desiccator. The sample is then placed into the chamber and the system is pumped down to approximately  $10^{-5}$  Torr to remove residual gases. The sputtering gas is then introduced via a leak valve and a continuous flow is maintained throughout the measurement. Fine adjustments in the pressure are made by throttling the high vacuum valve. The actual sputtering time for a



sample ranges from 5 to 40 minutes with a preliminary pumpdown of about one hour.

The GDOS system described here can only measure emission intensity as a function of wavelength or time. There must be an independent calibration of the sputtering rate of the sample to obtain any depth information. This was done by directly measuring the sputtering of the surface on a number of test samples. A test sample is covered with a protective layer of either  $\text{SiO}_2$  or  $\text{Si}_3\text{N}_4$  as in Figure 3.5. Most of the encapsulant is removed using photolithographic techniques, so that only thin strips of material are left on the surface. The sample is then mounted and sputtered as usual for a specified time. After sputtering, the encapsulant is removed, leaving two distinct regions on the surface of the sample: the original surface, which was protected from sputtering by the encapsulant, and the sputtered region which was exposed to the discharge. The difference in height between the two regions was measured with a Sloan Dektak surface profiler, and the sputtering rate was obtained from the measurement. An alternate approach used for implanted samples was to use the masking techniques described above and to monitor the depth distribution of implanted atoms while sputtering. The discharge is stopped when the peak of the implanted unannealed distribution is reached. The projected range of the distribution could then be measured directly using the Dektak as before.

### Depth Measurements



LS-1387

Fig. 3.5. Sputtering rate calibration by step height measurements. The difference between the original surface (protected by the  $\text{SiO}_2$ ) and the sputtered area is measured.

#### 4. GDOS INVESTIGATIONS

##### 4.1. Emission Spectra

The emission spectra observed in GDOS come primarily from two sources; the excited gas atoms in either neutral or ionized states, and the excited sputtered neutrals. The emission from the gas atoms dominates the spectrum and also defines the regions in which sputtered neutral emission may be observed. For example, krypton has only a few transitions in the range 2000 - 3000 Å, leaving this spectral region relatively transparent. The spectrum is filled with strong Kr emission lines at wavelengths greater than 3500 Å which can obscure all but the most intense signals from the sputtered neutrals. The noble gases are normally used in sputtering experiments to avoid reactive sputtering, and they are generally transparent in the uv portion of the spectrum.

Along with the strong allowed transitions from the gas, we have also observed a low-level continuous background emission. This emission varies from 100 to 1000 counts per sec and depends on the overall intensity of the discharge. We believe this background is due principally to scattered light in the optical system. A similar background intensity is observed in the SCANIR analysis system [59,60]. Empirically, we found krypton gave lower background levels than argon under similar discharge conditions.

A fundamental problem in emission spectroscopy is to properly identify the emission lines. While several tables of atomic emission lines exist [66-68] it is best to verify the position of the lines experimentally to eliminate small errors in the wavelength settings of the spectrometers.



In this work the spectrum was measured while sputtering with and without the sample to determine if the lines were due to the gas atoms or the backing plate material. Although we never observed a transition not found in the tables, often a listed emission line was not observed in the discharge. In general, the strong transitions listed in the wavelength tables are also the most intense lines observed in GDOS. However, the relative intensities of the lines may be quite different, as seen in Table 4.1. This is not surprising since the excitation in a spark source is dramatically different from that in GDOS. All of the lines observed from the sputtered material have been identified as due to transitions involving atomic neutrals. No transitions from ionized or molecular species were observed in the glow region.

A typical emission line from a silicon substrate atom is shown in Figure 4.1. Silicon has several allowed transitions near 2500 Å, and we follow the strong 2516.1 Å line in the substrate monitor during a sputtering run. In contrast to the intense emission from the substrate, an impurity such as boron is a much weaker emitter (Figure 4.2). The sample of Figure 4.2 contained approximately  $10^{20} \text{ cm}^{-3}$  of boron and has a peak intensity of 11 k counts per second. Although two distinct transitions separated by 0.9 Å are present, only one is measured during the experiment because of the very small bandwidth of the spectrometer.

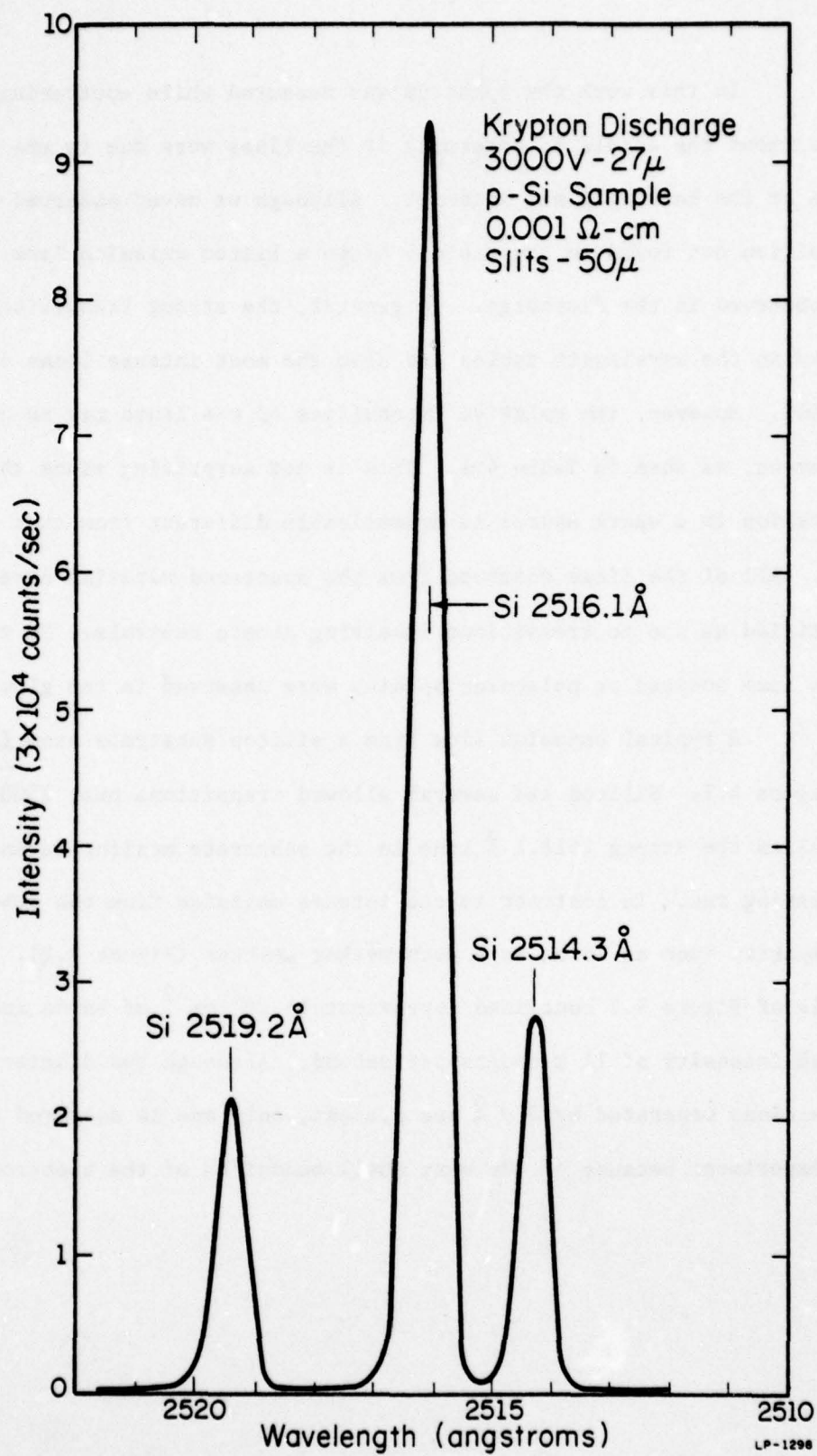


Fig. 4.1. A portion of the emission spectra of sputtered silicon. The 2516.1 Å line is used to monitor substrate sputtering.

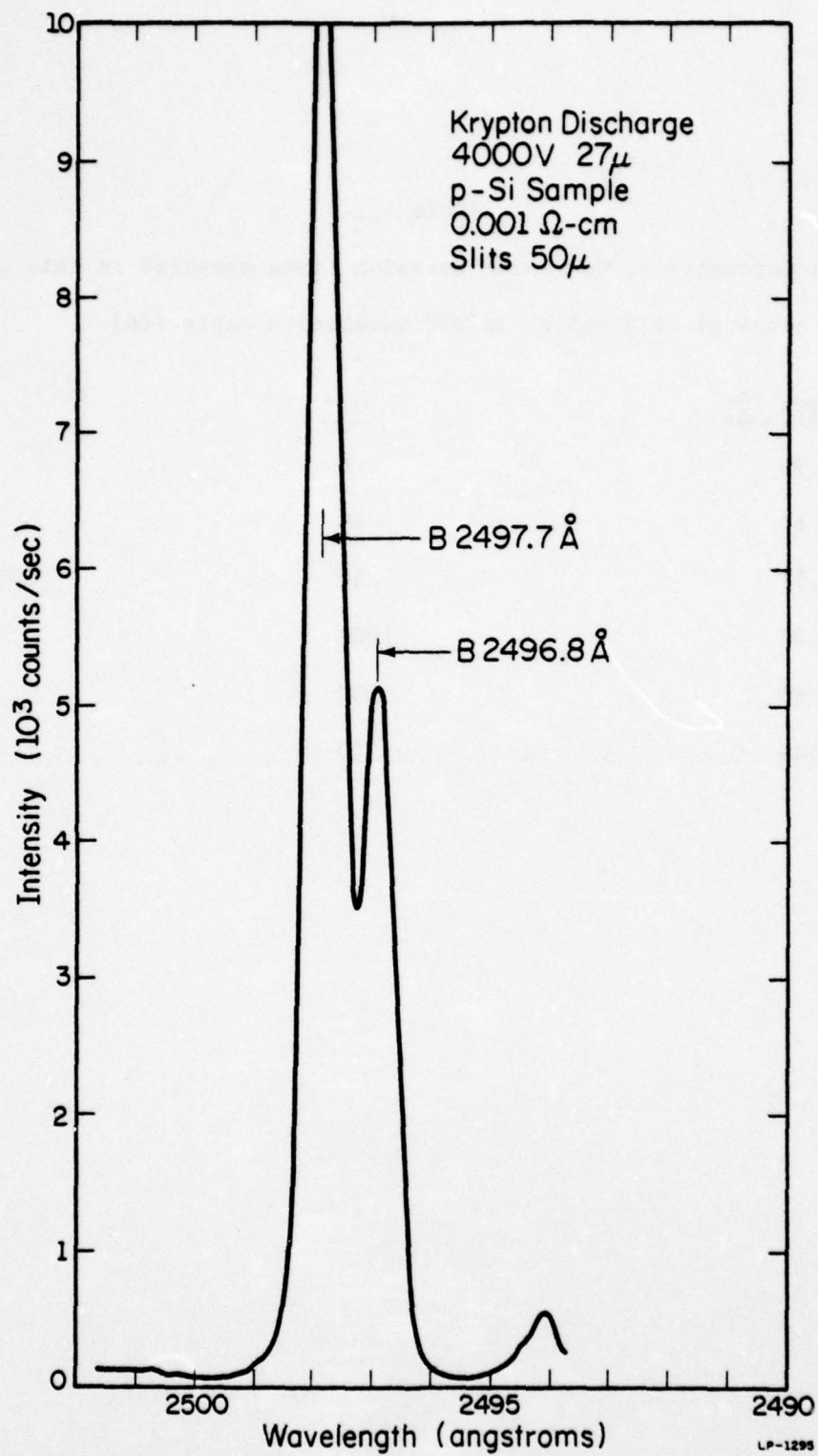


Fig. 4.2. A portion of the emission spectra of boron.



Table 4.1

Relative Intensity of Germanium Emission Lines measured in this work (GDOS), compared with values in MIT wavelength table [66].

<u>WAVELENGTH (<math>\text{\AA}</math>)</u>	<u>MIT</u>	<u>GDOS</u>
2497.96	8	9
2651.18	40	800
2651.57	30	NOT OBSERVED
3039.06	1000	1000
3124.82	200	20
3269.49	300	400

#### 4.2. Voltage and Pressure Effects

The intensity of an emission line has been shown to be proportional to the concentration of the corresponding element in the sputtered layer in a stable discharge [47]. As the current density is increased, the sputtering rate and the number of excited neutrals should also increase. One may assume the intensity is proportional to the sputtering rate times the number of electrons available for excitation. Since each term is proportional to the current, the intensity  $I$  depends on the square of the current density  $j$ .

$$I \propto j^2 \quad (4.1)$$

Using the Aston formulas (Equations 2.2 and 2.3) relating pressure, current density, and cathode fall voltage, we find

$$j = \left[ P \frac{(V_c - E)}{F} \right] \quad (4.2)$$

For a constant pressure, the current increases as  $V^2$ ; thus, the intensity should increase as the fourth power of the voltage.

$$I \propto j^2 \propto V^4 \quad (4.3)$$

The measured relationship between intensity and voltage is found to be

$$I \propto V^{4.5} \quad (4.4)$$

as seen in Figure 4.3. The slopes of the various emission lines are remarkably consistent, even though a wide range of wavelengths are excited. We have not observed preferential excitation of any wavelengths for the voltages studied.

From equations 4.1 and 4.2, the intensity should increase as

$$I \propto P^2 \quad (4.5)$$

for a constant voltage. However, the intensity does not increase monotonically with pressure, as seen in Figure 4.4. Each sample was sputtered with argon at a constant voltage while a single emission line was observed. The pressure was then changed and equilibrium sputtering reached before the next intensity measurement was taken. The effect of increased voltage was simply to increase the overall intensity; the shapes of the curves were not altered. Sputtering in a krypton discharge does not yield the same curves as an argon discharge (Figure 4.5). The intensities generally decrease with krypton pressure except for the arsenic line.

The increased gas pressure produces more current and a larger sputtering rate. However, it also increases the probability of a collision between a sputtered atom and a gas atom. Thus, cases of decreased light emission with increased pressure could be caused by a collisional de-excitation [69-71] of the excited neutrals in the discharge. Since krypton has a larger cross section than argon, the effect is more pronounced in that discharge. The anomalous behavior of arsenic in both discharges is still not understood. This could be caused by differences in atomic radii or in ejection energies.



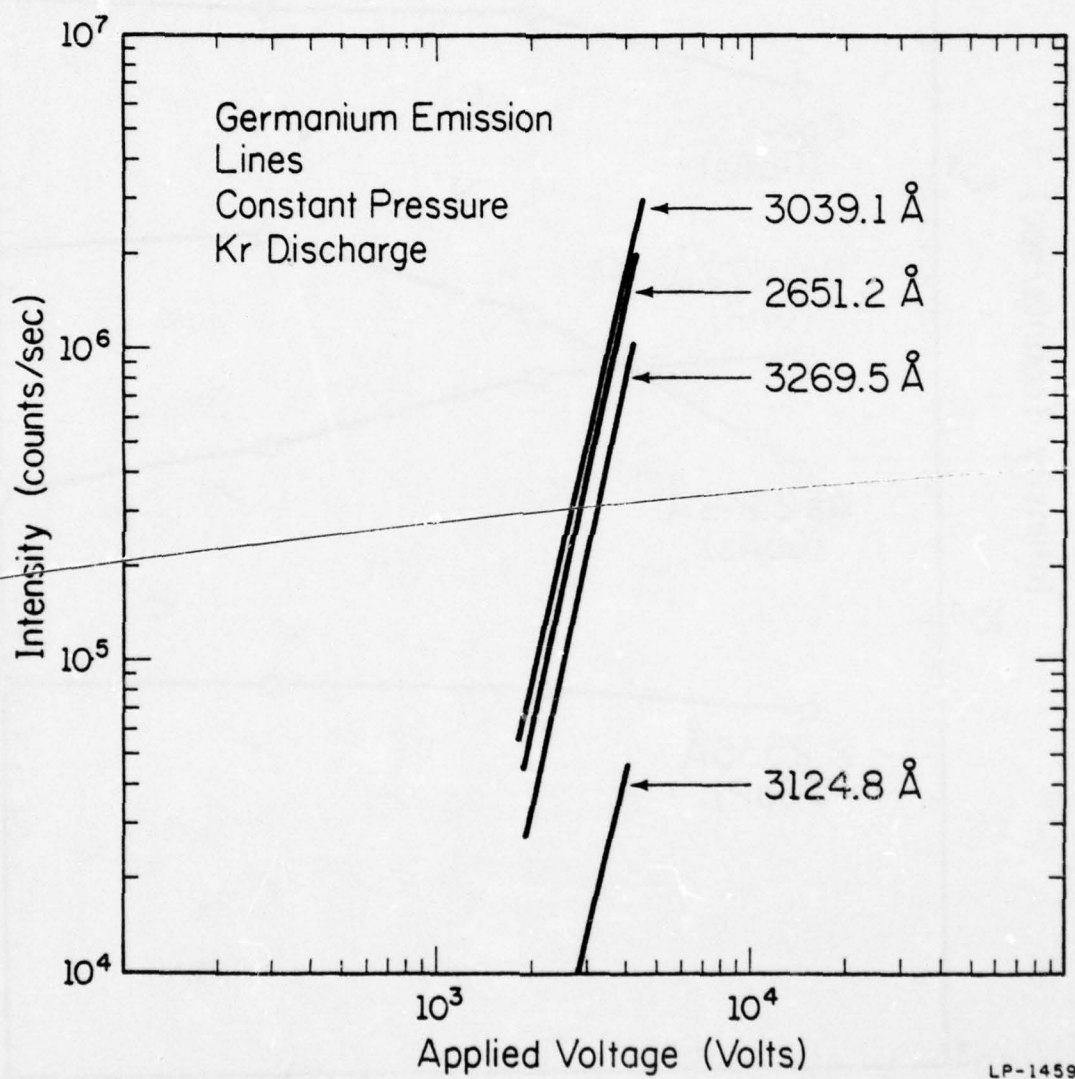


Fig. 4.3. The variation of emission intensity with applied voltage.

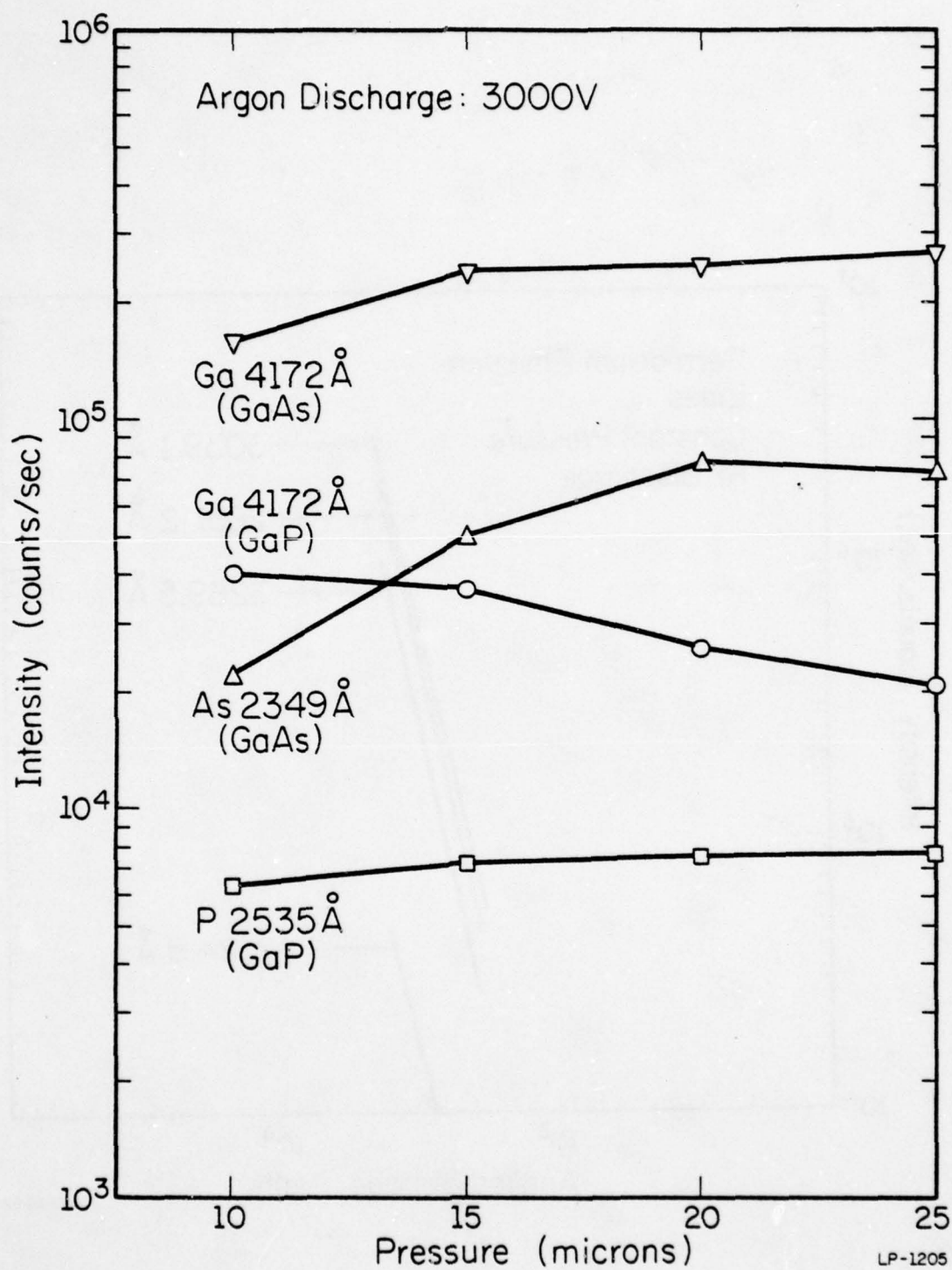


Fig. 4.4. Variation of Ga, As, and P emission intensities with argon pressure. Gallium arsenide and gallium phosphide were used as substrates.

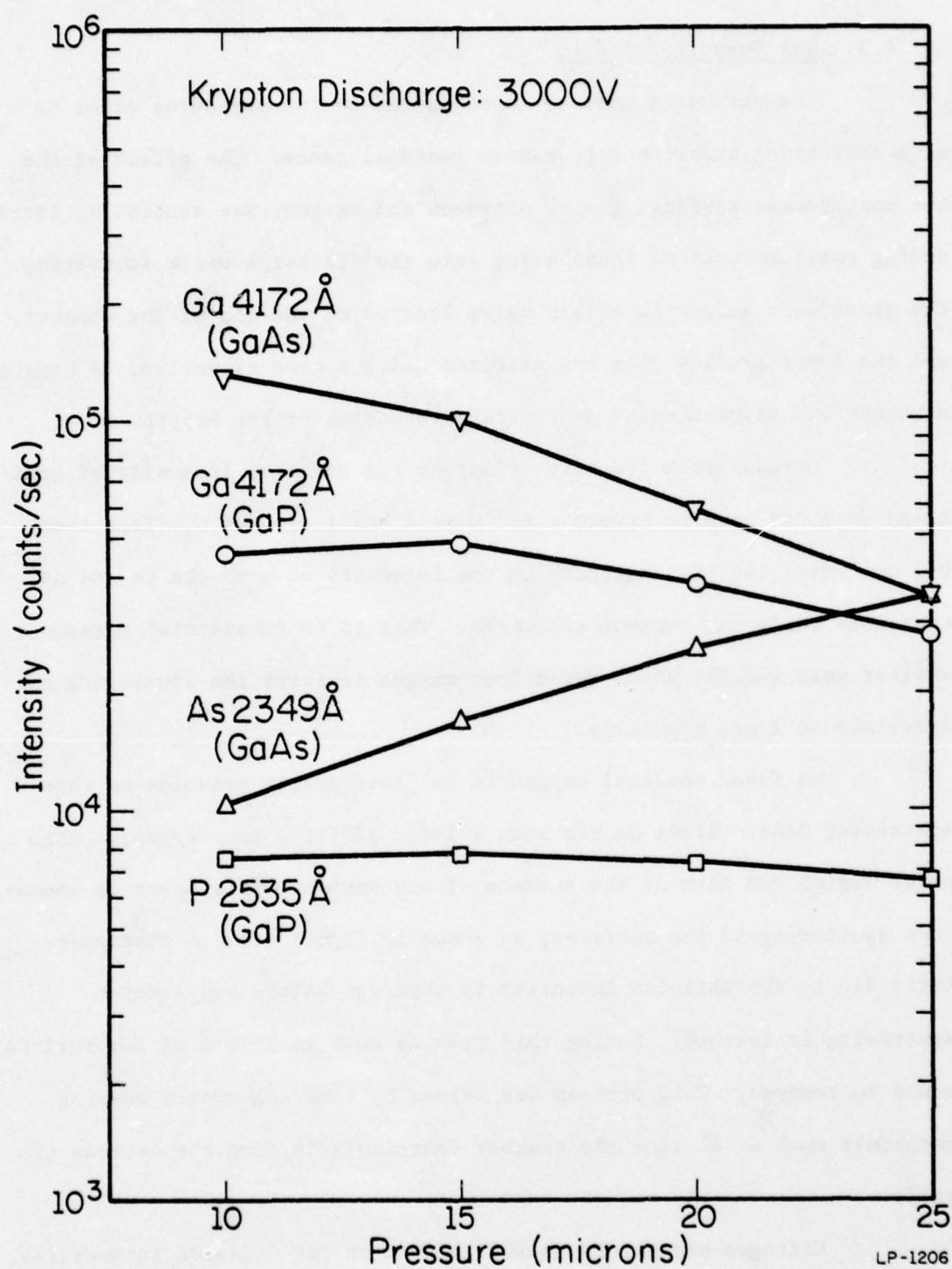


Fig. 4.5. Emission intensities of Ga, As, and P lines in krypton discharge.



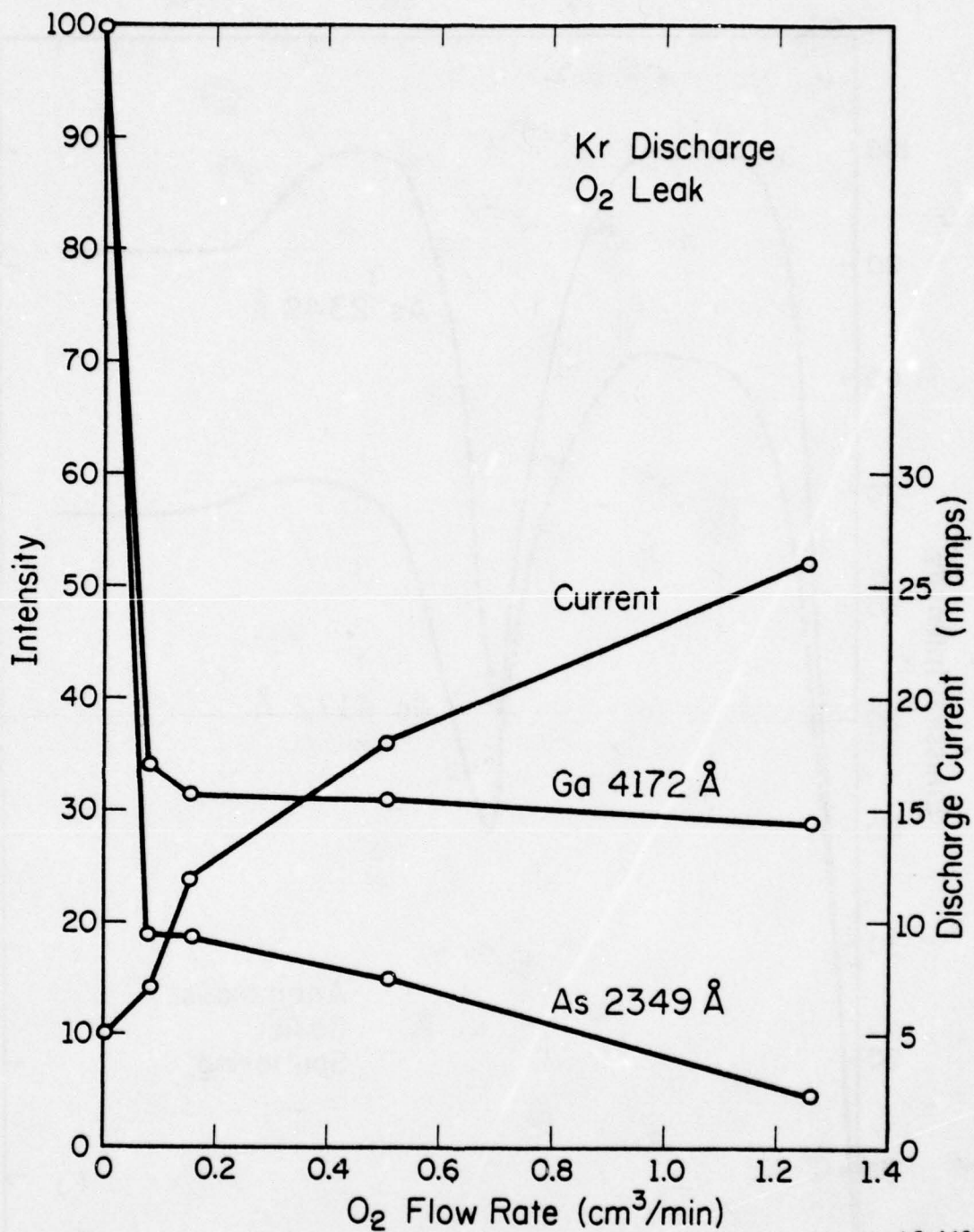
#### 4.3. Gas Impurity Effects

The discharge chamber is evacuated to low pressures prior to each sputtering experiment to remove residual gases. The effect of the two most common residual gases, nitrogen and oxygen, was studied by introducing small amounts of these gases into the discharge while sputtering. The gases were added via a leak valve located at the top of the chamber, and the impurity flow rate was measured using a mass flowmeter. A constant pressure was maintained by appropriate reduction of the krypton flow.

Oxygen has a dramatic effect on the emission intensity of sputtered GaAs, as seen in Figure 4.6. Even a small flow of  $O_2$  (less than  $0.1 \text{ cm}^{-3}/\text{min}$ ) causes a decrease in the intensity of both the Ga and As emissions while the current increases. This is in substantial agreement with earlier work [72,73] which found that oxygen inhibits the sputtering of materials in a gas discharge.

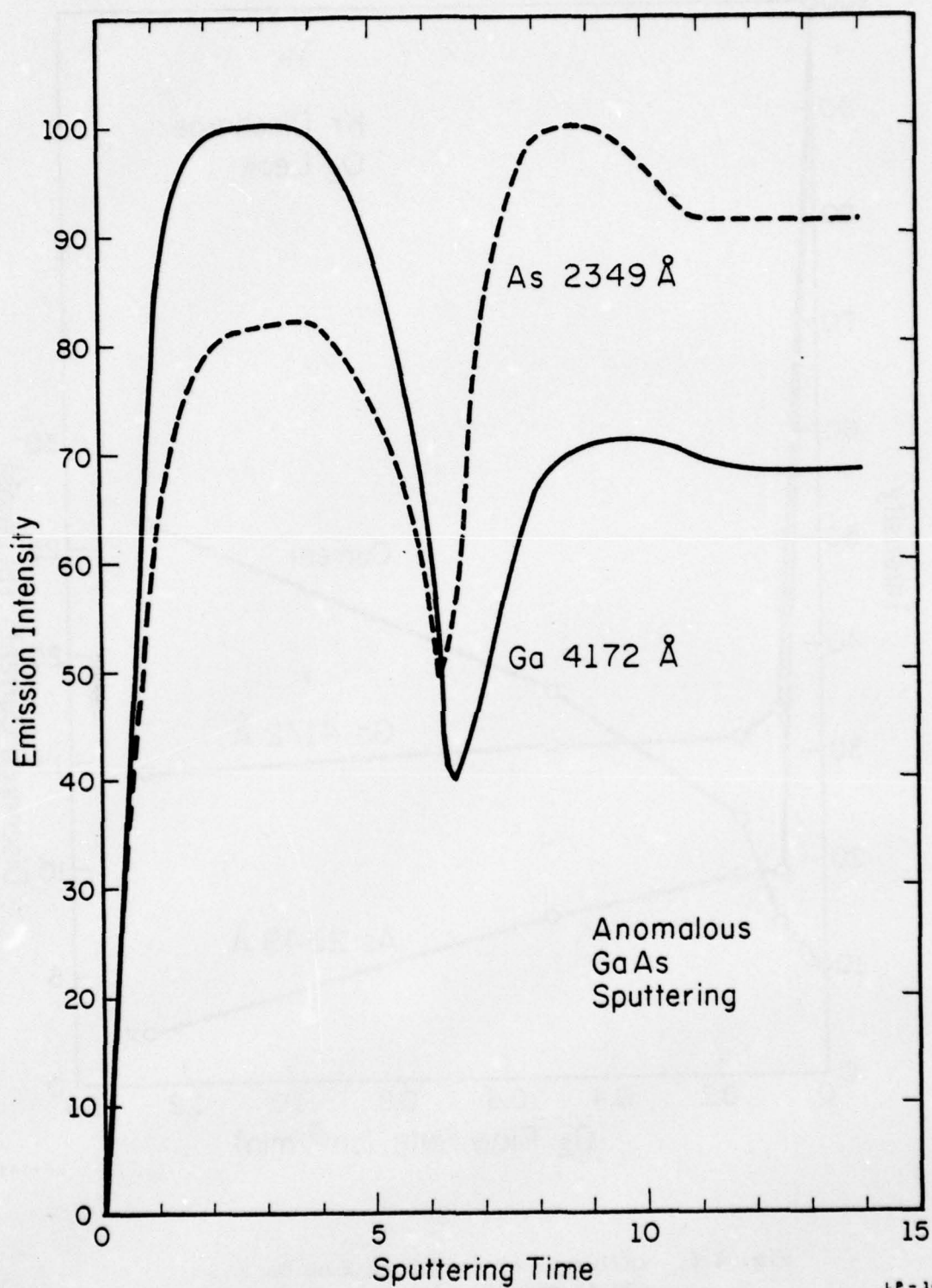
We found residual oxygen to be particularly troublesome when sputtering GaAs. Since Ga has such a large affinity for oxygen, a thin oxide region can form on the surface of the sample. This leads to anomalous sputtering of the surfaces, as shown in Figure 4.7. A characteristic dip in the emission intensity is observed before equilibrium sputtering is reached. During this time as much as  $1500 \text{ \AA}$  of the surface could be removed. This problem was solved by removing oxygen bearing materials such as Al from the chamber (particularly from the cathode itself).

Nitrogen has a more unusual effect on the emission intensities, as shown Figure 4.8. The current remains almost constant while both the Ga and As emissions increased through maxima located at different flow



LP-1458

Fig. 4.6. Influence of oxygen leak on Ga and As emission lines in krypton discharge.



LP-1464

Fig. 4.7. Anomalous sputtering of gallium arsenide substrates due to residual oxygen in chamber.



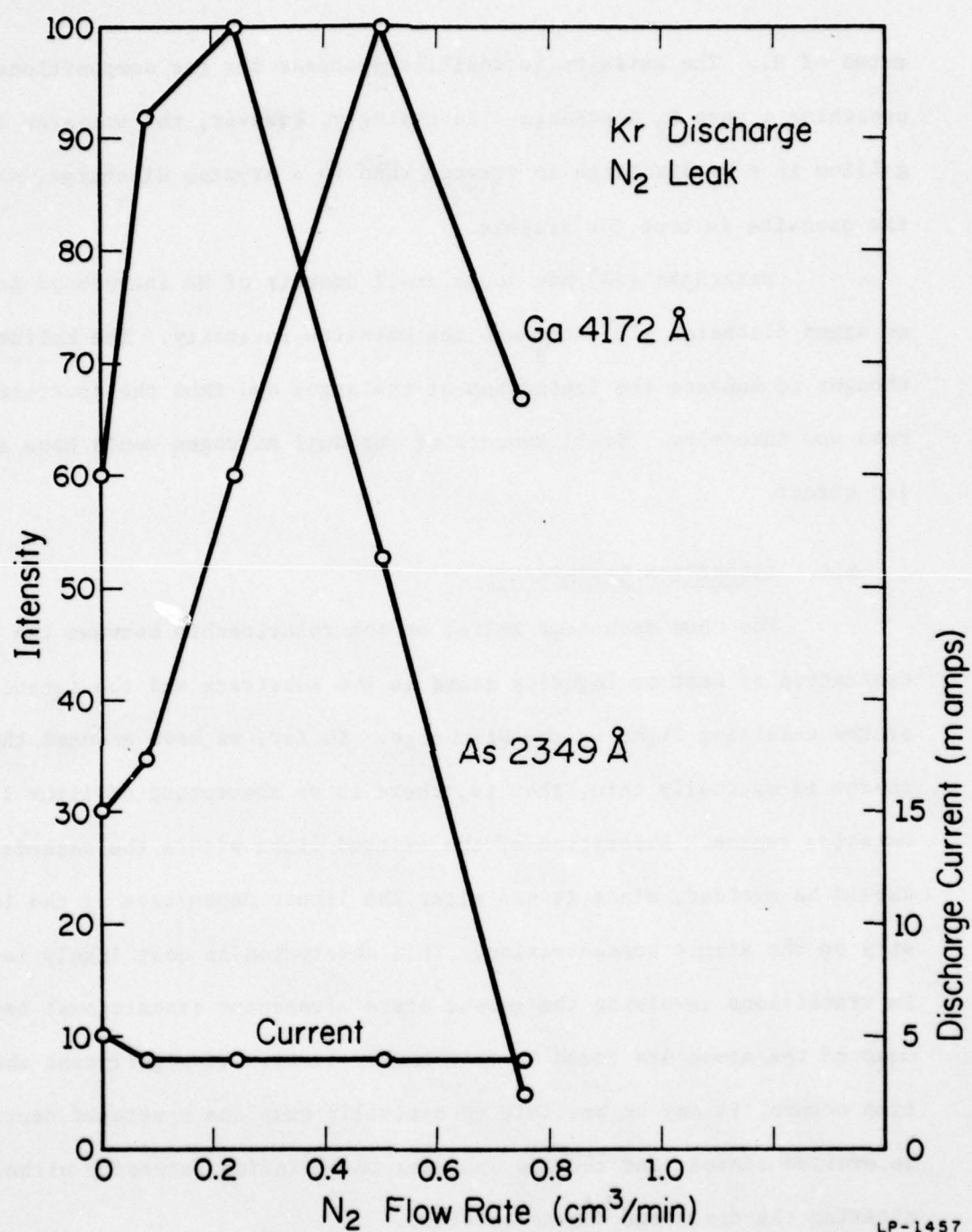
rates of  $N_2$ . The emission intensities decrease for gas compositions approaching a pure  $N_2$  discharge. Surprisingly, however, the emission from gallium in a  $N_2$  discharge is greater than in a krypton discharge, while the opposite is true for arsenic.

Natarajan [74] has found small amounts of He introduced into an argon discharge will increase the emission intensity. The helium is thought to enhance the ionization of the argon and thus the sputtering rate and intensity. Small amounts of residual nitrogen could have a similar effect.

#### 4.4. ABSORPTION EXPERIMENTS

The GDOS technique relies on the relationship between the concentration of host or impurity atoms in the substrate and the intensity of the resulting light in the discharge. So far, we have assumed the discharge is optically thin, that is, there is no absorption of light in the emission region. Absorption of the emitted light within the cathode region should be avoided, since it can alter the linear dependence of the intensity on the atomic concentration. This absorption is most likely to occur in transitions involving the ground state (resonant transitions) because most of the atoms are found in that energy level. If significant absorption occurs, it may be possible to optically pump the sputtered neutrals to excited states, and thereby increase the emission intensity without altering the discharge characteristics.

The absorption measurements were performed with GaAs samples using a gallium hollow cathode lamp as the light source. Since the lamp emits many different atomic lines simultaneously, the light was passed through a 1/2 meter Jarrel-Ash monochromator to isolate a single line.



LP-1457

Fig. 4.8. Influence of nitrogen leak on Ga and As emission lines in krypton discharge.

The output of the monochromator was collimated by lenses as in Figure 4.9 and was confined by a slit to the thin region of maximum emission intensity just above the sample. It was not possible to sample different regions of the discharge using this configuration because of the vertical orientation of the discharge chamber. The optical pumping experiment differs from the absorption measurement only in that the side window of the chamber is used to illuminate the sample area. This placed the incident light perpendicular to the detection system to minimize interference from the light source.

The intensity  $I_t$  of the light transmitted through the discharge is related to the incident intensity  $I_i$  by

$$I_t = I_i e^{-\alpha d} \quad (4.5)$$

Where  $d$  is the path length through the glow and  $\alpha$  is the absorption coefficient. The absorption coefficient is in turn the product of the number density of atoms  $n$  and their effective cross section  $\sigma(\lambda)$ . Using equation 4.5 we find

$$n = \frac{1}{\sigma(\lambda) d} \ln \frac{I_i}{I_t} \quad (4.6)$$

$$\text{or} \quad n \propto \ln \frac{I_i}{I_t} \quad (4.7)$$

assuming  $d$  and  $\sigma$  are constant for a given wavelength.

Since the atomic transition widths are exceedingly small ( $10^{-3}$  -  $10^{-4}$  Å), the spectrometer actually measures some integrated portion of the spectrum and not just a single wavelength as assumed in equation 4.5. Also, the width of the emission and absorption spectrum will be modified primarily by a Doppler broadening on the order of  $10^{-2}$  Å [28,75]. There-



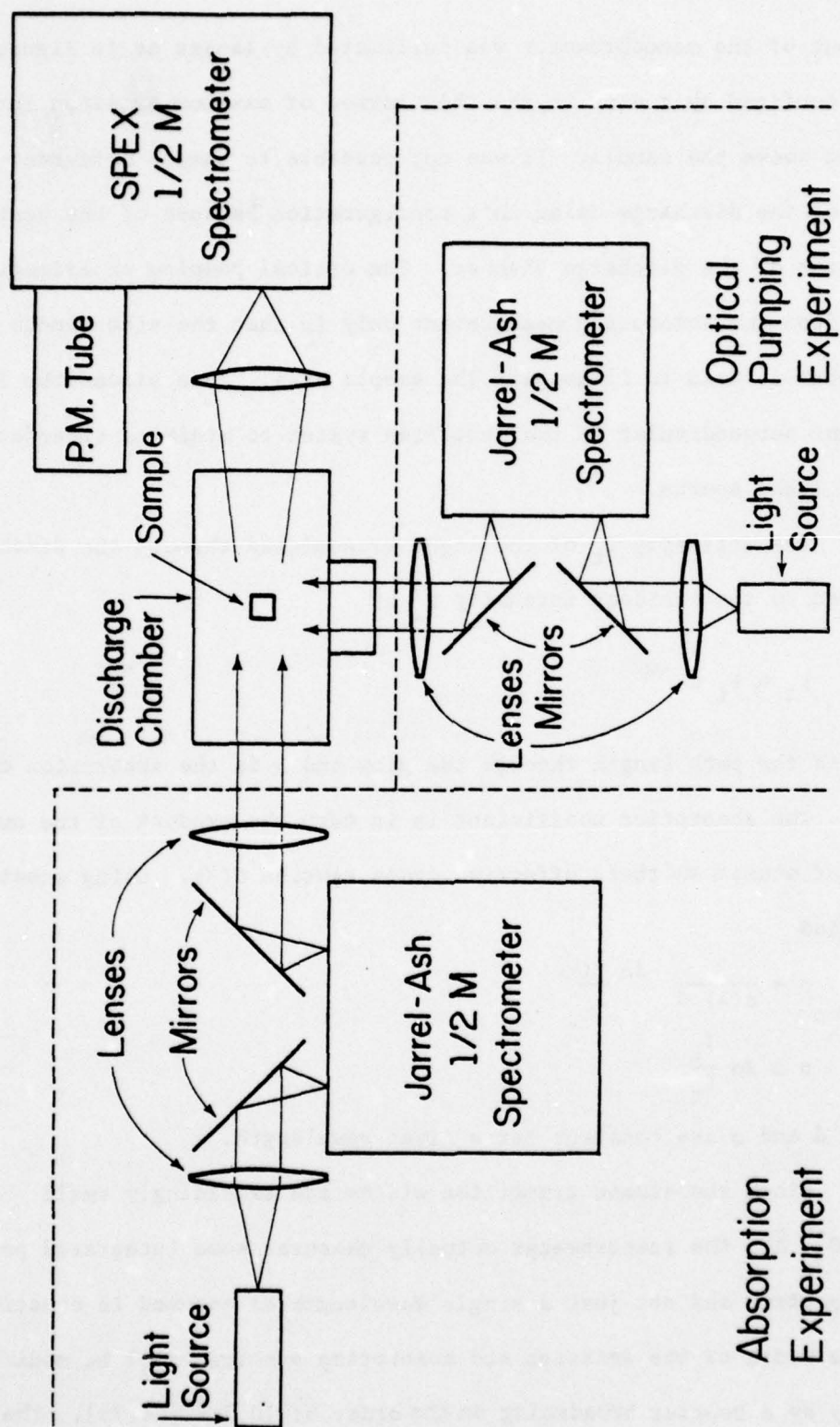


Fig. 4.9. Schematic diagram of absorption and optical pumping experiments.

fore the effective temperatures of the two media should be included. However, in this experiment we are attempting to determine if absorption exists and not to make an accurate measurement of  $n$ . Therefore, we will estimate the relative number of absorbing atoms by using equation 4.7.

Five of the gallium emission lines in the uv region are resonant transitions [68]. However, only the 2874 Å and 4032 Å lines were sufficiently intense to allow accurate measurements. Fortunately, these two lines share common energy levels associated with two non-resonant transitions as seen in Figure 4.9. This allows us to compare the absorption of both types of transitions directly.

As expected, in each case the absorption of the resonant transition is greater than for the corresponding non-resonant transition as shown in Table 4.2. This means simply that there are more atoms located in the ground state than in the higher energy states. The absorption increases with applied voltage and increased pressure (more sputtered neutrals) at approximately the same rate for each of the transitions. That is, no transition showed any preferential absorption due to changes in the discharge conditions.

As seen in Figure 4.9, it might be possible to optically pump the 2874 Å or 4032 Å lines to induce transitions in the 2944 Å or 4172 Å lines, respectively. Although light was absorbed in each of the resonant transitions, we did not observe any increase in the light emission from the two lower energy lines.

We conclude that there is some absorption of light in the cathode fall region. The absorption is usually small and increases with increased density of sputtered neutrals, induced by changes in pressure or voltage.

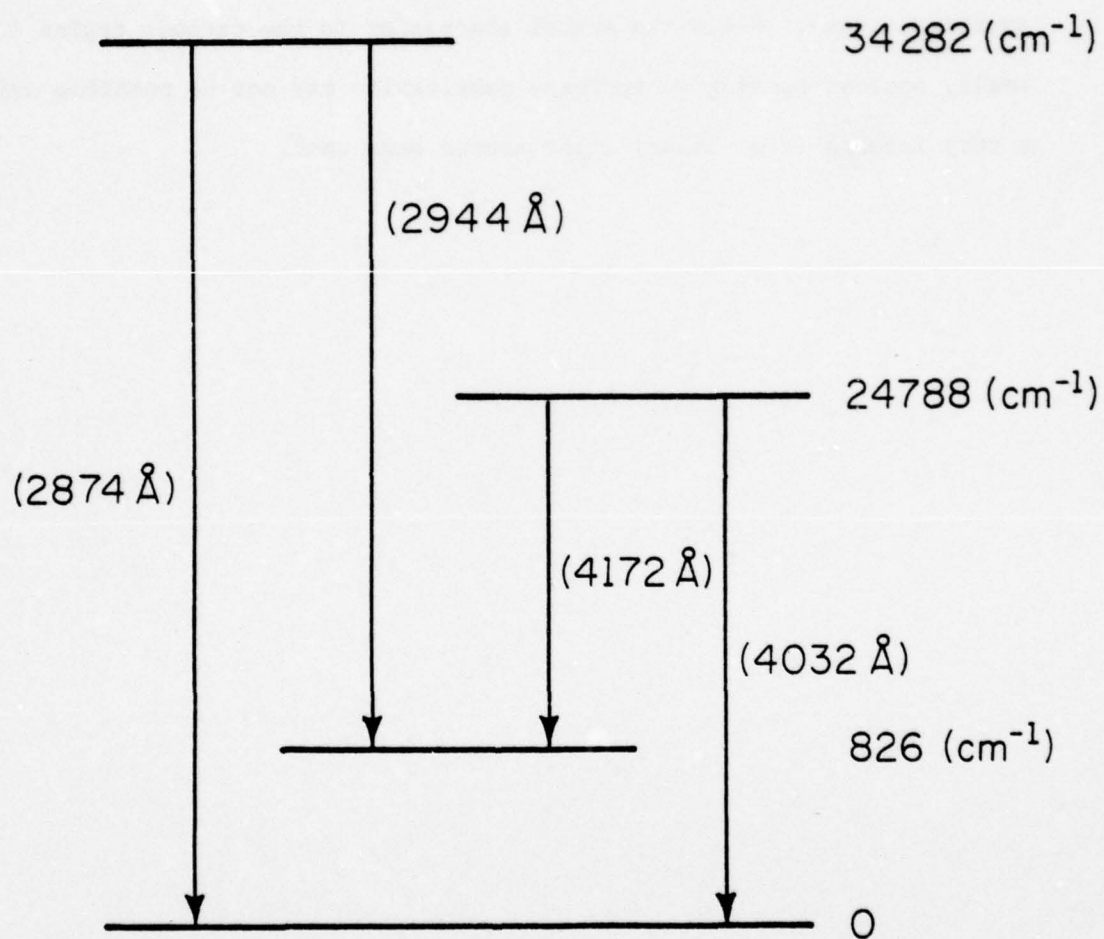
Table 4.2

## ABSORPTION IN GALLIUM EMISSION LINES

$\lambda(\text{\AA})$	E(eV)	Transition ( $\text{cm}^{-1}$ )	$\ln I_i/I_t$
2874.24	4.31	0-34782	0.0706
2944.18	4.21	826-34782	0.0526
4032.98	3.07	0-24788	0.1542
4172.06	2.97	826-24788	0.1286



## Neutral Gallium Transition



LP-1462

Fig. 4.10. Energy levels and transitions of neutral gallium used in optical pumping experiment.

Work by Sequeda-Osorio [65] with absorption spectroscopy showed the absorption was greatest in the dark regions of a dc discharge and was a minimum in the glow regions. Therefore self-absorption of emitted light should not be a problem for GDOS measurements, although some nonlinearity due to resonant transitions could be expected for high concentrations of sputtered atoms. Since the actual absorption in the cathode region is small, optical pumping to increase sensitivity may not be possible unless a very intense (e.g. laser) light source were used.

## 5. ATOMIC PROFILES

Whereas GDOS has previously been used successfully for plasma diagnostics, our primary interest here is in using GDOS as an analytical depth profiling tool for ion implanted semiconductors. One of the more serious problems associated with GDOS for depth profiling is that the discharge is unstable for a short period of time after initiation. The discharge current starts at a large value and slowly decreases with time to a steady state value. This behavior has been associated with the sputter cleaning of contaminants, particularly hydrocarbons, from the surface of the cathode [76]. The period of time needed before steady state is reached is thus related to the cleanliness of the cathode. Although this period can be shortened by careful cleaning of the cathode, it cannot be eliminated entirely. During this initial period, the sputtering rate of the sample and the excitation processes in the discharge are not constant. Therefore, the profile information contained in the surface region is lost. This effect is particularly troublesome for very shallow profiles (e.g. As into Si) where the entire implanted layer could possibly be sputtered before steady state is reached.

Some of the problems associated with transient sputtering can be reduced for the case of silicon by evaporating a thin layer of a metal such as nickel on to the surface of the sample. In this way, the nickel is sputtered during the initiation period, and the surface of the sample is protected. The interface between the nickel and the silicon is indicated by a sharp rise in the silicon emission line measured in the substrate monitor. Nickel was chosen as the overcoat layer since it has a faster sputtering rate than silicon, and yields a sharp interface (Figure



5.1). Nickel is also electrically conductive and can be handled easily without scratching.

Similar transient sputtering problems occur in the profiling of GaAs, but to a much lesser extent. We were not able to find a suitable overcoat material which gave a sharp surface interface. Therefore, the GaAs samples were profiled from the bare surface.

#### 5.1. Sample Preparation

All of the samples except for the arsenic implanted silicon [77], were implanted in the ion implantation facility of the Coordinated Science Lab. The silicon samples were  $\langle 100 \rangle$  7-14 $\Omega$ -cm p-type material and were cleaned prior to implantation using solvents and a hydrogen peroxide-based cleaning solution [78] to remove organic and metallic contamination. The GaAs samples were  $\langle 100 \rangle$  bulk GaAs, grown by the horizontal Bridgeman technique, doped with either Te or Si to an electron concentration of approximately  $10^{17} \text{ cm}^{-3}$ . The GaAs samples were cleaned only in solvents prior to implantation.

The implants were performed at room temperature with no deliberate heating or cooling of the samples. The smaller samples (i.e. GaAs) were mounted onto a aluminum plate before implantation using silver conducting micropaint to allow the entire surface of the sample to be implanted and to facilitate handling. The wafers were tilted at  $7^\circ$  from the beam normal during implantation to avoid channeling effects.

Two sets of silicon wafers were implanted. The first set was arsenic implanted into a bare surface at 150 keV and to a dose of  $5 \times 10^{15} \text{ cm}^{-2}$ . The second set was implanted through a thin thermally grown oxide layer on the surface, while keeping the same energy and dose as before. The  $\text{SiO}_2$  was

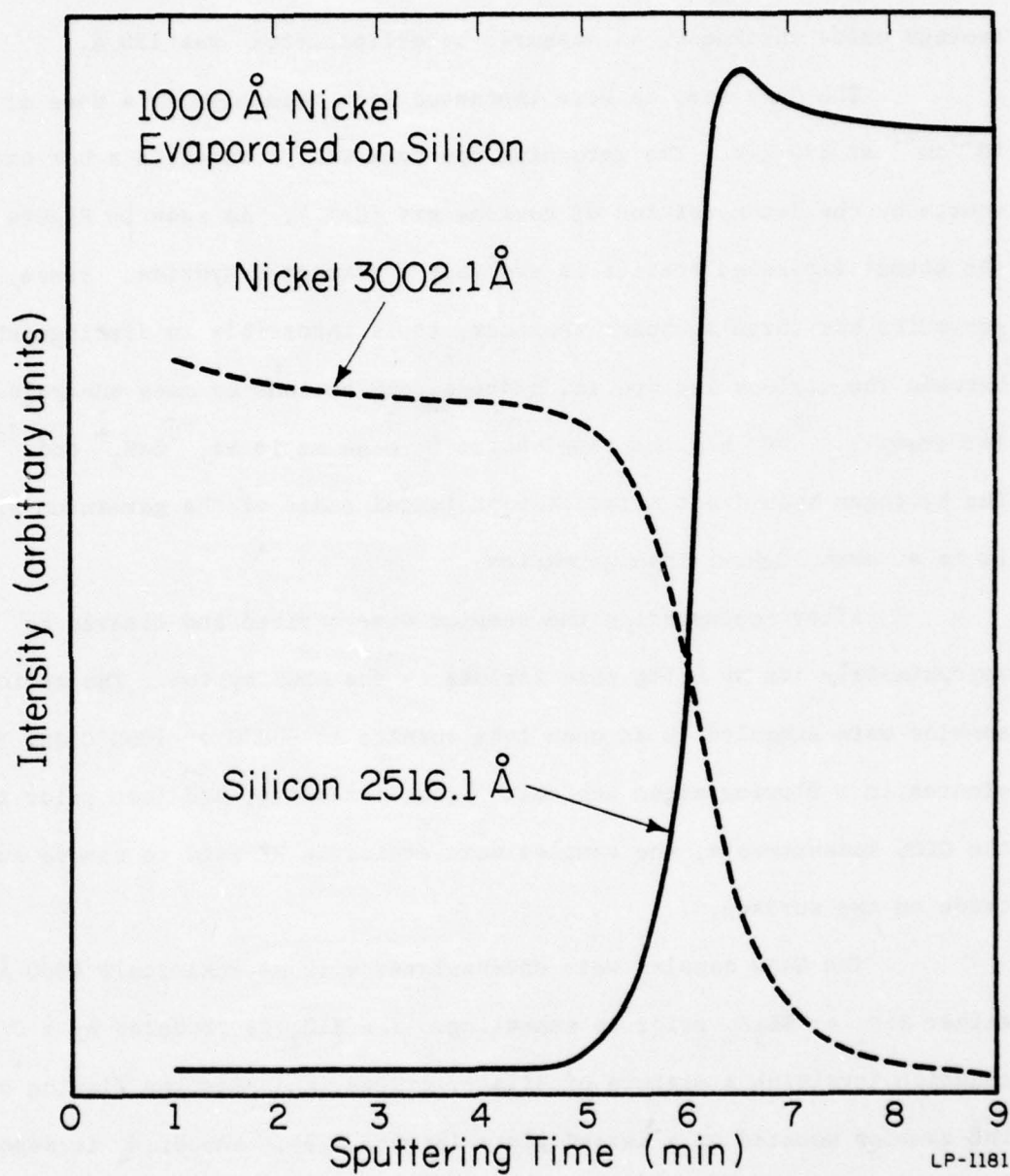


Fig. 5.1. Emission intensity of Si (from substrate) and Ni (evaporated layer on surface) during sputtering.

grown at 900°C for 20 minutes in a dry oxygen atmosphere, followed by a 5 minute bakeout at the same temperature in a nitrogen ambient. The average oxide thickness, as measured by ellipsometry, was 150 Å.

The GaAs samples were implanted with germanium to a dose of  $10^{15} \text{ cm}^{-2}$  at 250 keV. The germanium ion beam was produced in a hot cathode source by the decomposition of germane gas ( $\text{GeH}_4$ ). As seen in Figure 5.2, the actual implanted species is probably a germanium hydride. Since germanium has three abundant isotopes, it is impossible to distinguish between the various isotope and hydride combinations by mass analysis. For example,  $^{72}\text{Ge}^+$  has the same charge to mass ratio as  $^{70}\text{GeH}_2^+$  and  $^{71}\text{GeH}^+$ . The hydrogen should not affect the projected range of the germanium since it is so much lighter than germanium.

After implantation the samples were scribed and cleaved to approximately 1cm by 0.5cm size for use in the GDOS system. The silicon samples were annealed in an open tube furnace at 600°C or 1000°C for 30 minutes in a flowing argon ambient. After annealing, and just prior to the GDOS measurements, the samples were etched in HF acid to remove any oxide on the surface.

The GaAs samples were encapsulated with approximately 1000 Å of either  $\text{SiO}_2$  or  $\text{Si}_3\text{N}_4$  prior to annealing. The  $\text{SiO}_2$  is produced by a CVD reaction involving a mixture of silane, oxygen, and nitrogen flowing over the samples mounted on a heated plate (Figure 5.3). The  $\text{Si}_3\text{N}_4$  is deposited by a reactive plasma technique [79] in which a silane-argon mixture is introduced into a vacuum chamber just above the heated samples as shown in Figure 5.4. The silicon nitride is formed by a reaction involving the silane and nitrogen radicals supplied by an rf-induced nitrogen plasma.



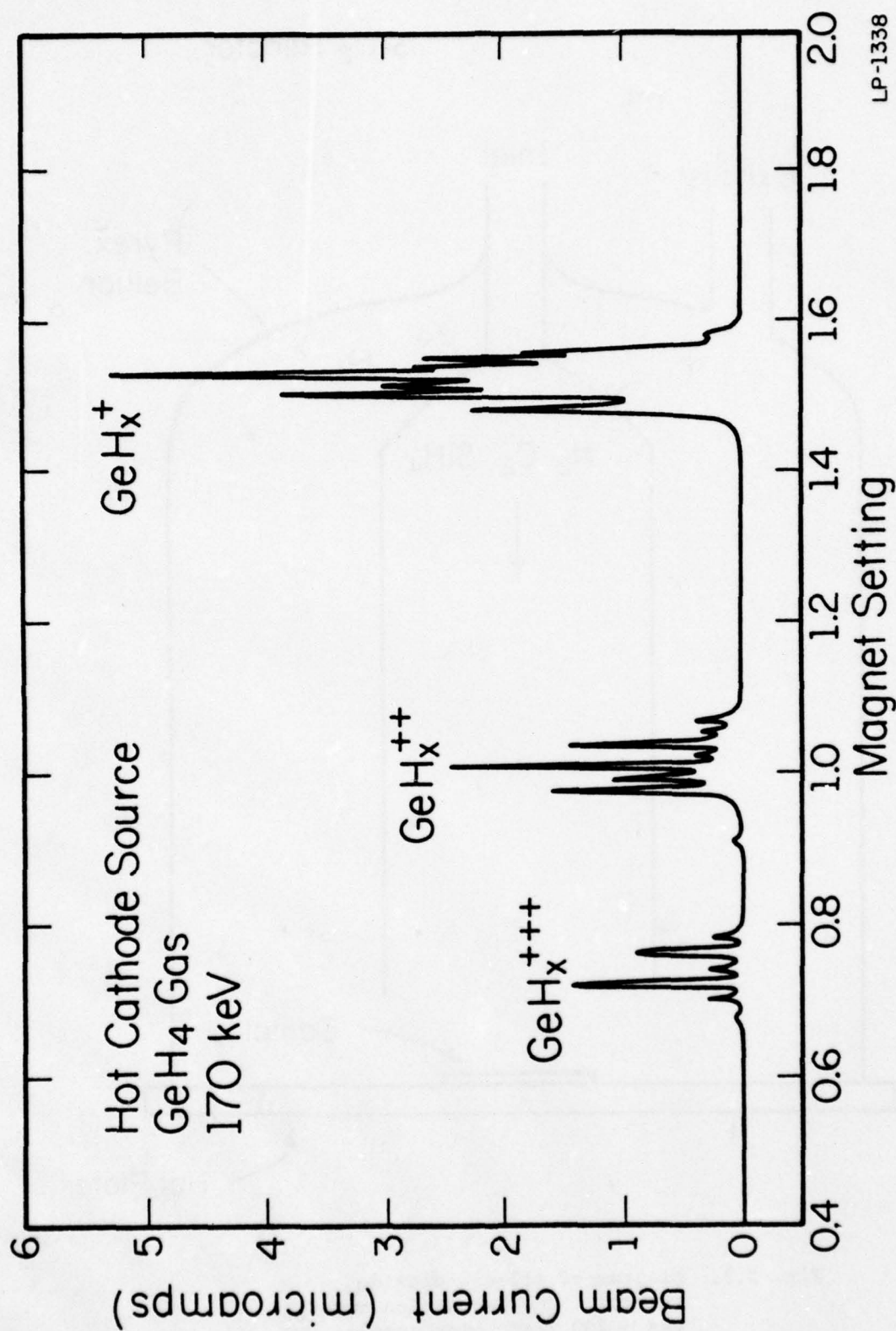
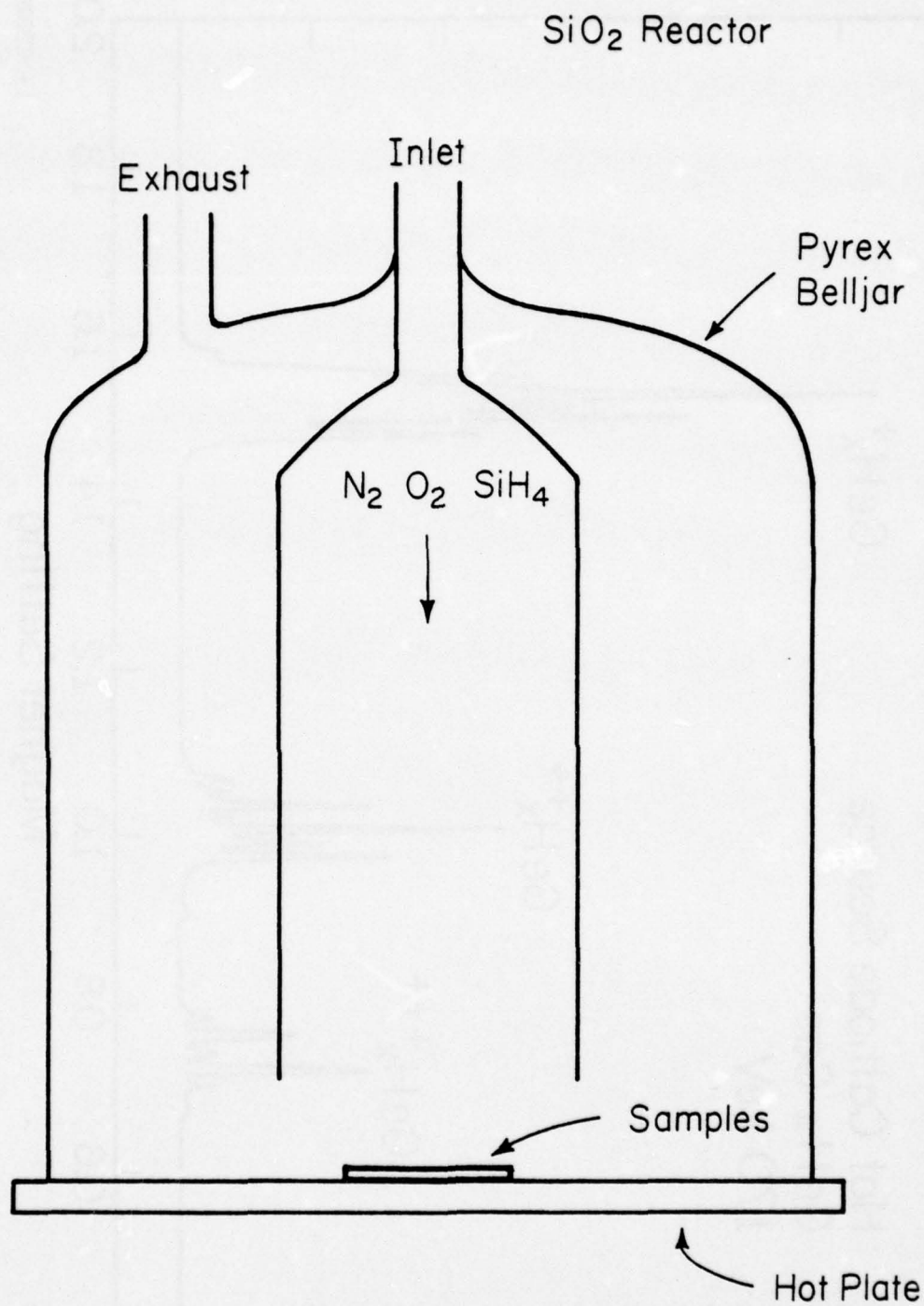
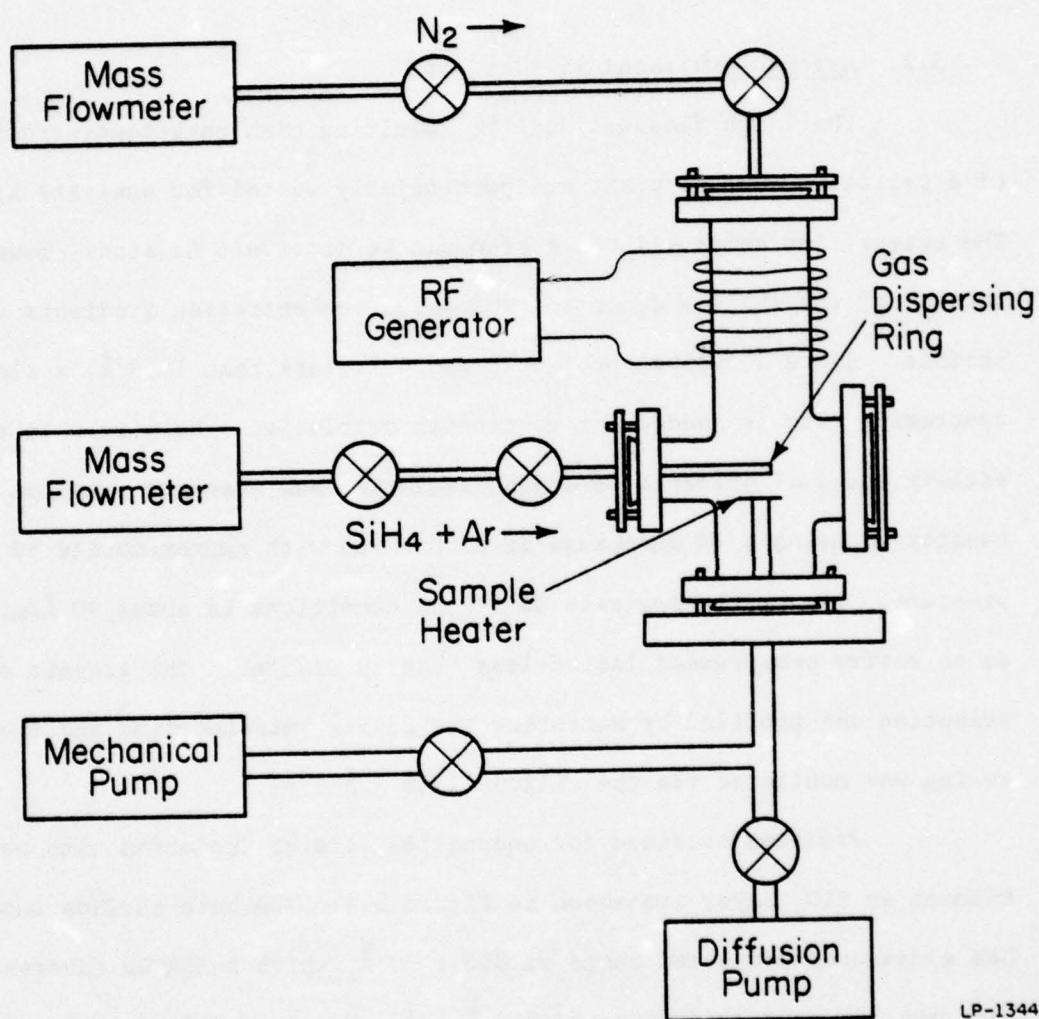


Fig. 5.2. Mass spectra of ions produced with hot cathode source by decomposition of germane gas.



LP-1463

Fig. 5.3. Diagram of silicon dioxide reactor. The deposition rate was  $\sim 200 \text{ \AA/min}$  with samples heated to  $400^\circ\text{C}$ .



LP-1344

Fig. 5.4. Diagram of silicon nitride plasma reactor. The samples are heated to  $\sim 300^\circ\text{C}$  during deposition.



The samples were isochronally annealed for 30 minutes in an open tube furnace with a flowing nitrogen-4% hydrogen ambient. The anneal temperatures ranged from 500°C to 900°C in 100° increments. The encapsulants were removed in a HF etch prior to the measurement.

### 5.2. Arsenic-Implanted Silicon

The large fluences and the resulting high peak concentrations of a typical arsenic implant are particularly suited for analysis by GDOS. The arsenic implanted silicon system can be difficult to study, however, because of the shallow depth and the large concentration gradients of the profile. Since a typical projected range is less than 1000 Å, a slow sputtering rate is needed for good depth resolution. We were able to satisfy the dual criteria of depth resolution and adequate emission intensity by using a Kr discharge at 3500 V and with approximately 50  $\mu$  pressure. The sputtering rate for these conditions is about 90 Å/min, so an entire measurement lasted less than 30 minutes. The arsenic distribution was profiled by measuring the 2349 Å emission line and the sputtering was monitored via the silicon 2516 Å line.

Profiles obtained for unannealed samples implanted with and without an SiO<sub>2</sub> layer are shown in Figure 5.5. The bare surface implant has a measured projected range of  $800 \pm 50$  Å, which compares favorably with the LSS predicted range of 845 Å [7]. The measured straggle of 360 Å is somewhat larger than the calculated value of 292 Å. These results agree substantially with those obtained by SIMS on similarly implanted samples [80]. There is a slight decrease in the silicon emission intensity measured by the substrate monitor as the transition from the amorphous

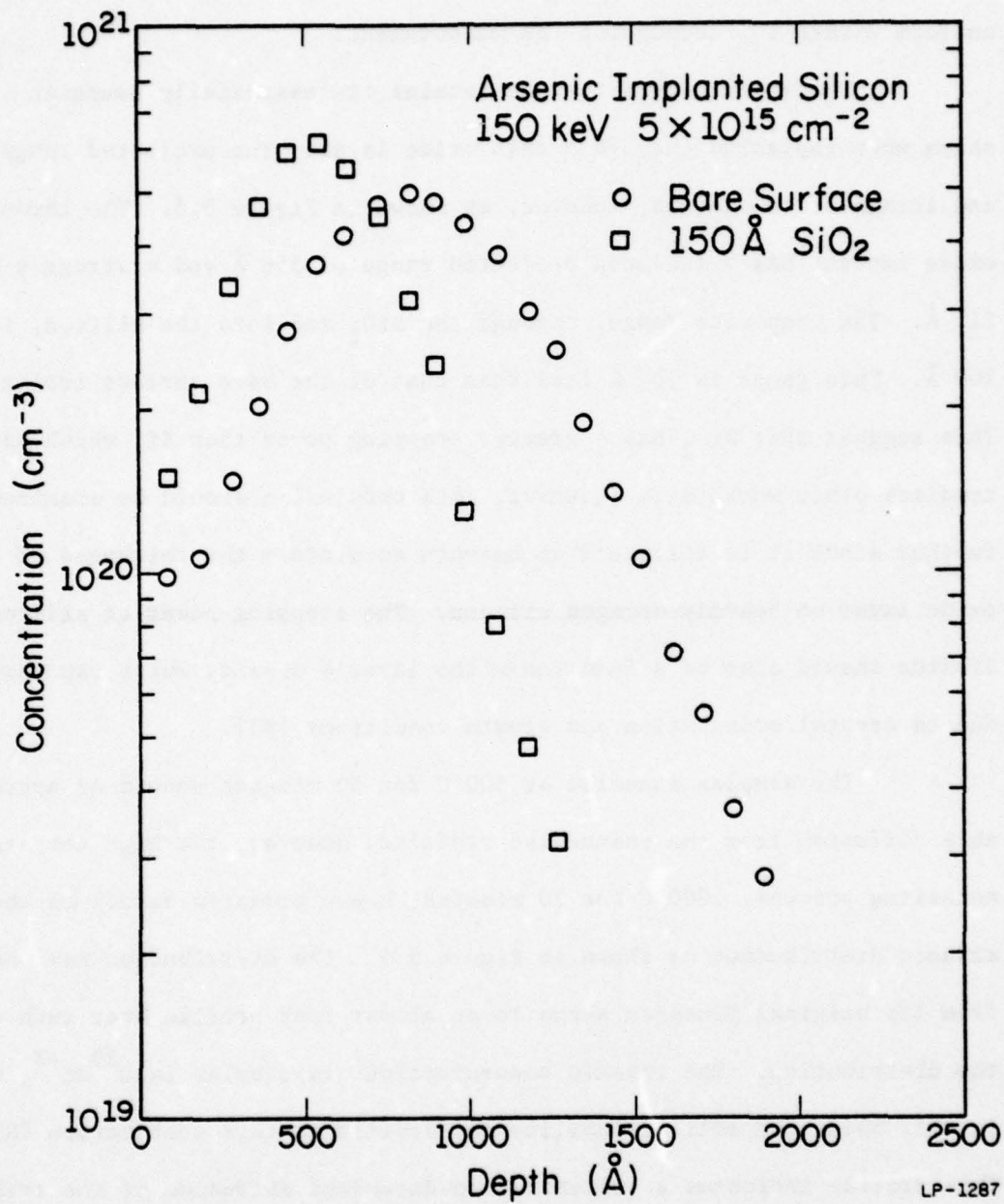


Fig. 5.5. Depth profiles of unannealed arsenic-implanted silicon. The implants were performed into bare Si or through 150 Å of  $\text{SiO}_2$ .

implanted region to the crystalline substrate is reached at a depth of approximately 1500 Å. However, the sputtering rate of the silicon is uniform within 10% throughout the measurement.

The arsenic distribution retains its essentially Gaussian shape when implanted through a thin oxide layer. The projected range and straggle are changed, however, as shown in Figure 5.5. The through-oxide implant has a measured projected range of 550 Å and a straggle of 225 Å. The composite range, through the  $\text{SiO}_2$  and into the silicon, is 700 Å. This range is 100 Å less than that of the bare surface implant. This suggests that  $\text{SiO}_2$  has a greater stopping power than Si, which contradicts other work [81]. However, this conclusion should be examined further since it is difficult to measure accurately the thickness of an oxide layer on heavily damaged silicon. The stopping power of silicon dioxide should also be a function of the layer's density which can vary due to crystal orientation and growth conditions [82].

The samples annealed at 600°C for 30 minutes showed no appreciable diffusion from the unannealed profiles. However, the high temperature annealing process, 1000°C for 30 minutes, has a dramatic effect on the arsenic distribution as shown in Figure 5.6. The distribution has changed from its original Gaussian shape to an almost flat profile over much of the distribution. The arsenic concentration stays below  $2 \times 10^{20} \text{ cm}^{-3}$ , which is well below the solid solubility for arsenic at this temperature [83]. This profile indicates a concentration-dependent diffusion of the arsenic and is characteristic of high dose implants annealed at high temperatures.



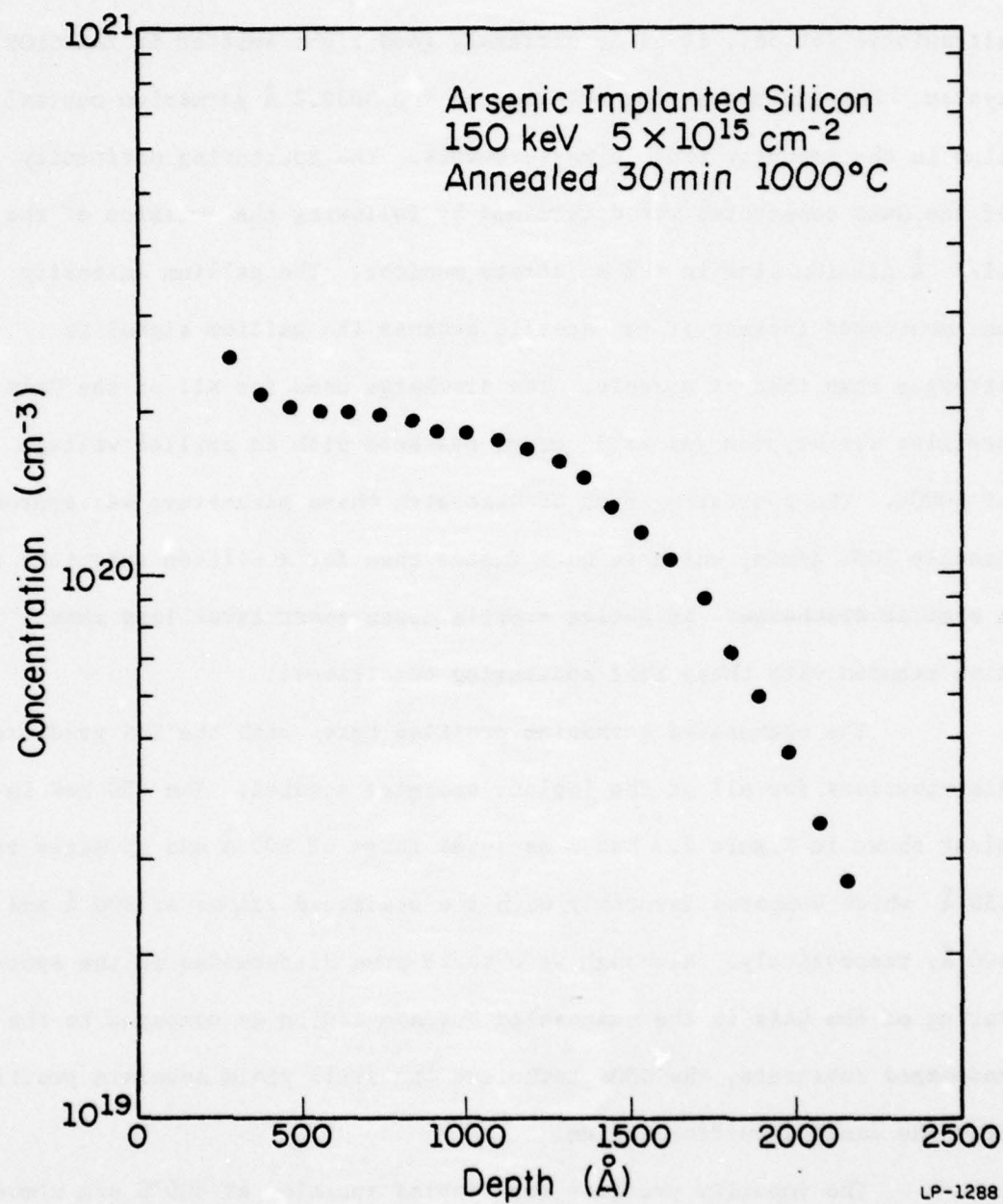


Fig. 5.6. Depth profile of As distribution after 30 minute anneal at  $1000^\circ\text{C}$ .

### 5.3. Germanium Implanted Gallium Arsenide

Since germanium has only a few allowed transitions in the ultraviolet [66,68], it is an extremely good light emitter in the GDOS system. We used the strong emission of the  $3039.2 \text{ \AA}$  germanium neutral line in the impurity profile measurements. The sputtering uniformity of the GaAs substrates was determined by following the emission of the  $4172 \text{ \AA}$  gallium line in the substrate monitor. The gallium intensity was monitored instead of the arsenic because the gallium signal is stronger than that of arsenic. The discharge used for all of the GaAs profiles was krypton gas at 30 mTorr pressure with an applied voltage of 4000V. The sputtering rate of GaAs with these parameters was approximately  $2000 \text{ \AA}/\text{min}$ , which is much faster than for a silicon substrate in a similar discharge. An entire profile measurement takes less than five minutes with these fast sputtering conditions.

The unannealed germanium profiles agree with the LSS predicted distributions for all of the implant energies studied. The 250 keV implant shown in Figure 5.7 has a measured range of  $900 \text{ \AA}$  and straggle of  $450 \text{ \AA}$ , which compares favorably with the predicted values of  $900 \text{ \AA}$  and  $400 \text{ \AA}$ , respectively. Although we observe some differences in the sputtering of the GaAs in the unannealed surface region as compared to the undamaged substrate, the GDOS technique can still yield accurate profiles from the damaged surface region.

The impurity profiles for samples annealed at  $600^\circ\text{C}$  are almost identical to the unannealed distributions. The type of encapsulation had no measurable effect on the profile at this temperature. This result is not surprising, since the anneal temperature is probably not

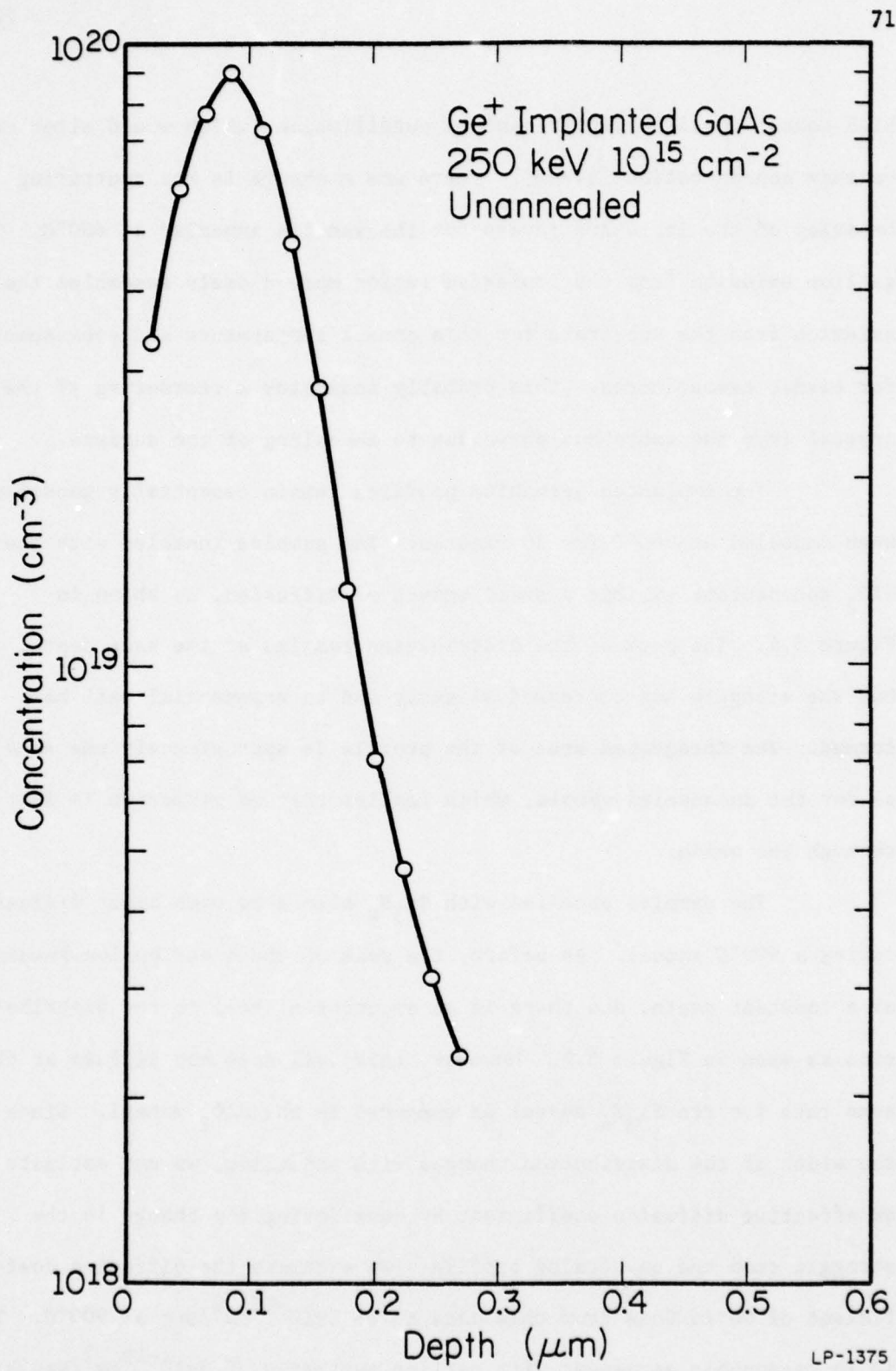


Fig. 5.7. GDOS profile of unannealed Ge-implanted GaAs.



high enough to allow significant Ga outdiffusion, which would alter the vacancy concentration [84-86]. There was a change in the sputtering behavior of the implanted layers for the samples annealed at 600°C. The gallium emission from the implanted region more closely resembles the emission from the substrate for this anneal temperature and subsequently for higher temperatures. This probably indicates a reordering of the crystal from the amorphous phase due to annealing of the surface.

The implanted germanium profiles remain essentially gaussian when annealed at 900°C for 30 minutes. The samples annealed with the  $\text{SiO}_2$  encapsulant exhibit a small amount of diffusion, as shown in Figure 5.8. The peak of the distribution remains at the same depth, but the straggle has decreased slightly and an exponential tail has formed. The integrated area of the profile is approximately the same as for the unannealed sample, which implies that no germanium is lost through the oxide.

The samples annealed with  $\text{Si}_3\text{N}_4$  also show some minor diffusion during a 900°C anneal. As before, the peak of the distribution remains at a constant depth, and there is an exponential tail to the distribution as seen in Figure 5.9. However, this tail does not diffuse at the same rate for the  $\text{Si}_3\text{N}_4$  anneal as compared to the  $\text{SiO}_2$  anneal. Since the width of the distribution changes with annealing, we can estimate an effective diffusion coefficient by considering the change in the straggle from the unannealed profile. We estimate the diffusion coefficient of Ge in GaAs from this data to be  $6 \times 10^{-15} \text{ cm}^2/\text{sec}$  at 900°C. This is in reasonable agreement with earlier estimates of  $5 \times 10^{-16} \text{ cm}^2/\text{sec}$  at 700°C [87].

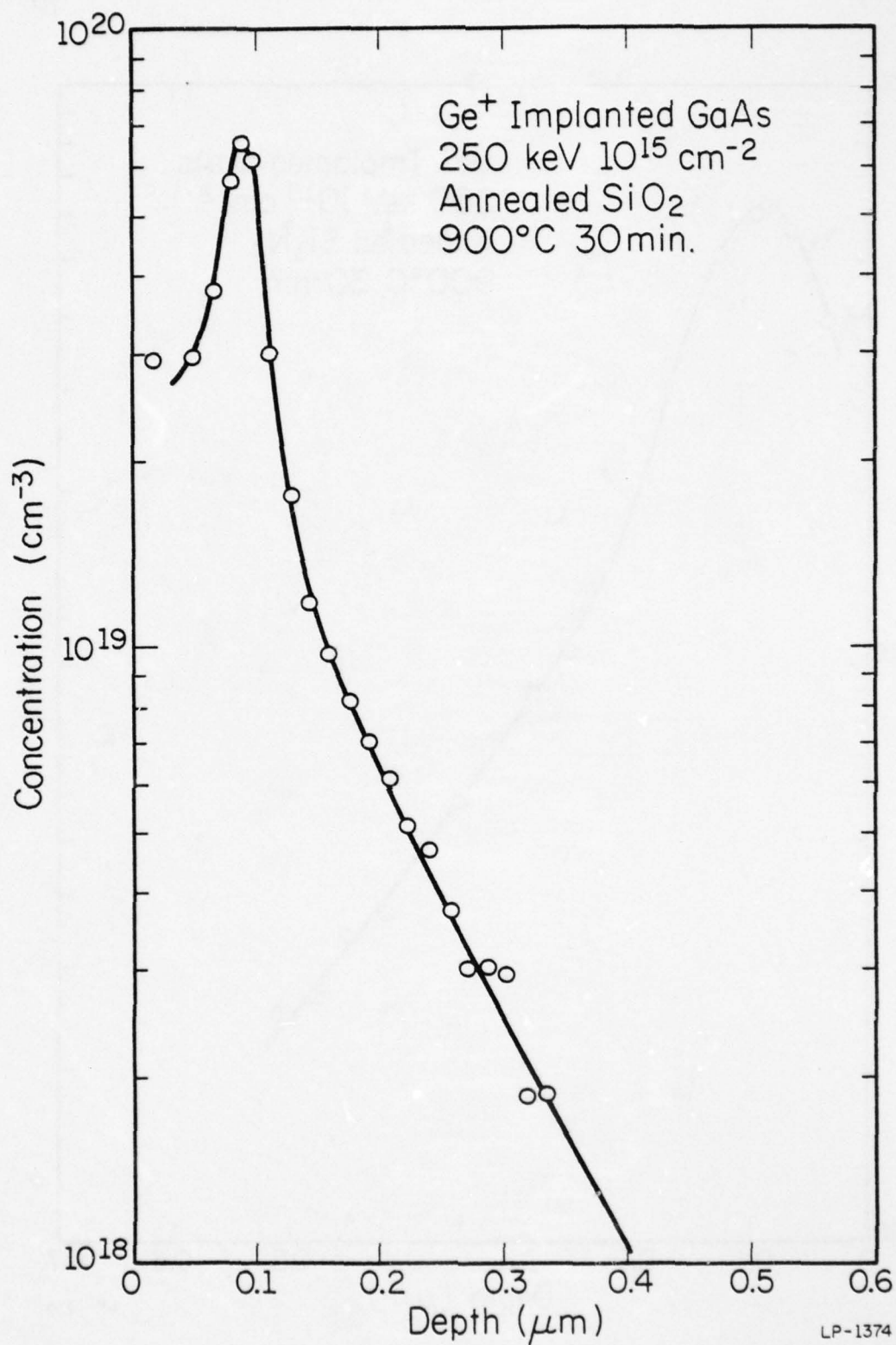


Fig. 5.8. Distribution of implanted Ge after 30 minute anneal at 900°C using SiO<sub>2</sub> encapsulant.

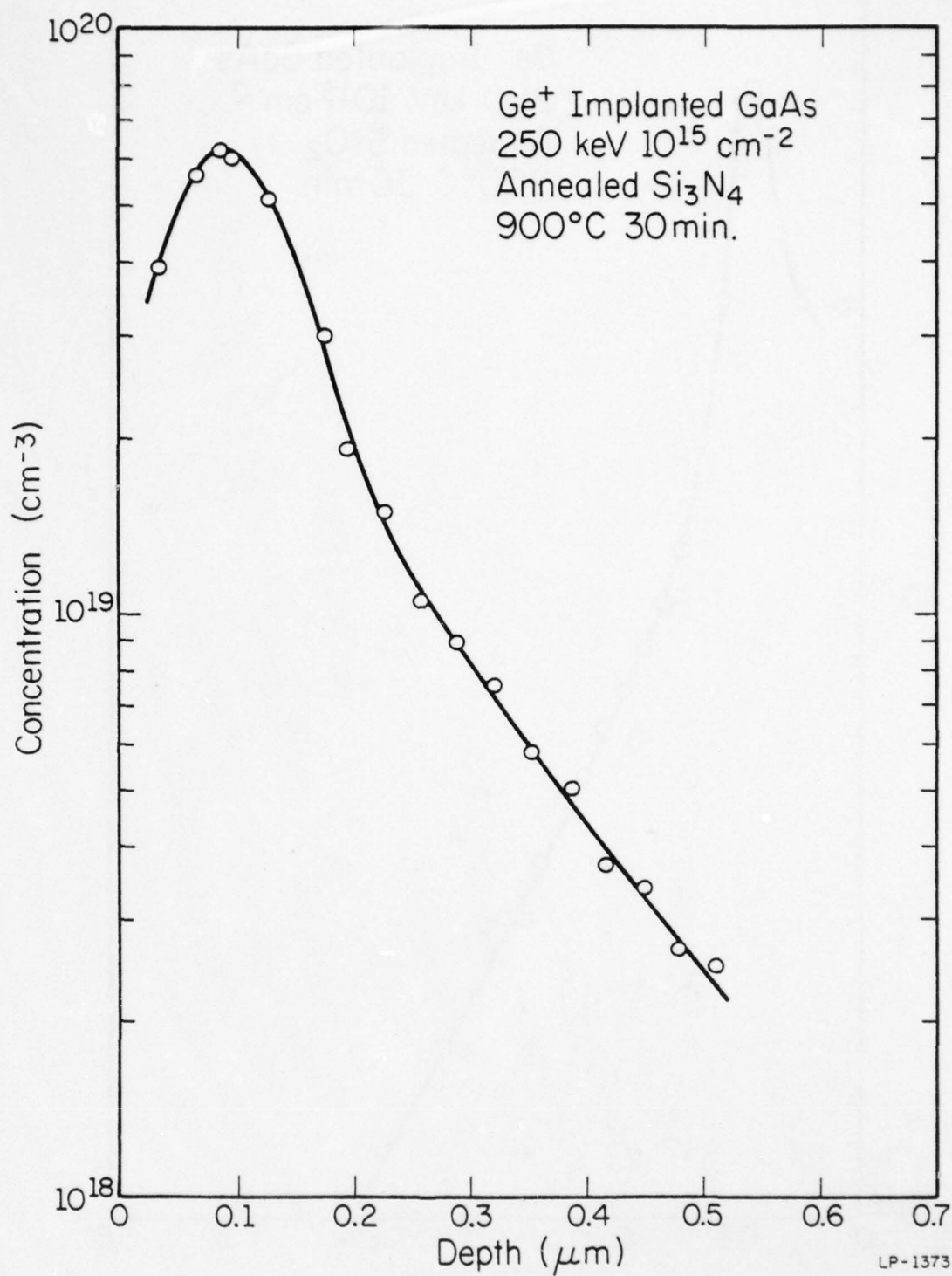


Fig. 5.9. Ge distribution after 30 minute anneal at 900°C using Si<sub>3</sub>N<sub>4</sub> encapsulation.



These results are somewhat surprising since they indicate the diffusion of germanium is slightly greater when annealed with nitride than with oxide encapsulants. A previous study of the diffusion of Ge in GaAs, using arsenic overpressure, suggests that Ge diffuses via gallium vacancies [88]. One might expect to observe enhanced diffusion for the samples encapsulated with  $\text{SiO}_2$ , since the oxide permits gallium outdiffusion, and thus generates gallium vacancies [84-86]. However, the number of gallium vacancies may be much less for the oxide anneal than for an arsenic overpressure anneal, depending on the experimental conditions. Chaing and Pearson [86] estimate the concentration of gallium vacancies at surface of the sample during an oxide anneal to be  $5 \times 10^{16} \text{ cm}^{-3}$  at  $800^\circ\text{C}$ . As Casey [89] points out, the actual diffusion source and mechanisms for a sealed ampoule anneal are complex, and should be determined using a detailed study of the ternary phase diagram. Thus, we cannot compare the diffusion in a sealed ampoule anneal directly to an encapsulated sample.

Even though the samples annealed with nitride show more diffusion than the oxide annealed sample, the actual diffusion in both cases is very minor. Germanium implanted gallium arsenide does not exhibit the strong concentration-dependent diffusion effects observed for Be and Zn implanted samples [90,91]. The atomic profiles indicate that germanium may be useful for creating thin, highly doped regions in GaAs.

#### 5.4. Elemental Sensitivity

The atomic profiles of several implanted impurities have been studied using GDOS and, in principle, any element could be detected and

profiled. In practice, only those elements with strong radiative transitions in the ultraviolet can be examined. The preferred elements for analysis are those with only a few allowed transitions. Nitrogen, for example, is a poor light emitter in GDOS. It has more than one hundred transitions in the uv region [66-68]; consequently, the intensity of any one transition is weak. Fortunately, some of the typical impurities of interest to semiconductor applications can be successfully profiled.

Table 5.1 lists the estimated sensitivities for a number of elements sputtered in this work from various sources. Since the excitation mechanisms in GDOS occur outside the sample, the relative sensitivities should be matrix-independent. Sulfur, selenium, and tellurium are poor light emitters and their detection limit is about one atomic percent. These values were obtained using a krypton discharge under typical operating conditions and are not the ultimate detection limit of the system. Better sensitivities could be obtained simply by increasing the sputtering rate of the samples, with a corresponding loss of depth resolution. Larger samples could be used, but this approach is often not practical, especially for compound semiconductors.

The elemental sensitivity in GDOS depends on the sputtering rate, the excitation efficiency of the sputtered atoms, the strength of the radiative transition, the light collection efficiency, and the detector response. The sputtering rate and the electron excitation mechanisms are not independent in a self-sustained discharge. Therefore, it is not always possible to increase the elemental detection limit without suffering a corresponding loss in the depth resolution. We have no control

Table 5.1  
Estimated GDOS Sensitivity

Element	Material Sputtered	$\lambda(\text{\AA})$	Intensity (Counts/sec)	Detection Limit ( $\text{cm}^{-3}$ )
Al	Al	3082.1	$4.0 \times 10^5$	$10^{19}$
As	GaAs	2349.8	$7.0 \times 10^4$	$10^{18}$
B	Si(0.001 $\Omega$ -cm)	2497.7	$5.0 \times 10^3$	$10^{17}$
Be	Cu-2%Be	2348.6	$5.0 \times 10^4$	$5 \times 10^{18}$
Cd	CdSe	2288.0	$1.1 \times 10^4$	$10^{20}$
Cu	Cu-2%Be	2824.4	$7.5 \times 10^3$	$10^{20}$
Ga	GaAs	4172.1	$1.2 \times 10^6$	$10^{19}$
Ge	Ge	3039.1	$1.5 \times 10^6$	$10^{18}$
P	GaP	2535.6	$1.0 \times 10^5$	$5 \times 10^{18}$
S	CdS	2089.9	$2.0 \times 10^2$	$10^{21}$
Se	CdSe	2039.8	$3.5 \times 10^3$	$10^{20}$
Si	Si	2516.1	$1.8 \times 10^5$	$5 \times 10^{18}$
Te	CdTe	2385.8	$8.0 \times 10^3$	$10^{20}$



over some of the important parameters which govern the sensitivity. For example, the strength of the radiative transition is determined solely by the atomic species. We have not been able to preferentially excite a selected wavelength by changes in the discharge pressure or voltage. There is a good possibility of increasing the total light output of the discharge by using a gas mixture as the sputtering medium. However, any changes in the excitation mechanism will probably alter the strength of all the observed transitions equally.

The one area in which significant advances in lowering the detection limit can be made is the light collection efficiency. So far, we have utilized only a small fraction of the light generated in the discharge. The light analysis systems could also be improved. For example, the grating spectrometers are relatively inefficient. Also their optical design ( $f/8$ ) does not allow us to focus all of the light from the broad emission region onto the narrow entrance slit. A Fabry-Perot interferometer may be a better instrument for this system. Of course, as the optical system becomes more sophisticated, so does the problem of alignment and reproducibility.

In summary, GDOS can produce adequate atomic profiles for a select group of impurities used in semiconductor research. The technique is best suited for the analysis of high concentration levels of dopants. Both crystalline and thin amorphous regions may be examined. The elemental sensitivity of GDOS is usually better than that of Auger electron spectroscopy, but not as good as secondary ion mass spectroscopy. Unfortunately, GDOS is a wide-beam technique, that is, there is no lateral resolution available.

There is a strong possibility that the sensitivities obtained in this study may be improved in the future. Further refinements in the optical system and perhaps mixed gas sputtering will lower the detection limit. Until these improvements are realized, GDOS will continue to play only a minor role in semiconductor characterization.

## 6. ELECTRICAL MEASUREMENTS

The important electrical parameters of an ion implanted layer are sheet resistance, carrier concentration, and mobility. The sheet resistance can be evaluated from a single van der Pauw measurement [10]. Obviously, the carrier concentration and mobility are functions of depth for an implanted layer, thus a single measurement is inadequate to profile the distribution of carriers. A double-ac Hall technique described in detail elsewhere [2], combined with successive layer removal was used to profile the electrical activity of implanted layers in this study.

### 6.1. Measurement System

The double-ac system is a variation of the basic Hall measurement [91] which exploits the excellent noise rejection available from phase sensitive lock-in techniques. In this system, an alternating current at a frequency of 1 kHz flows through the sample and, simultaneously, the applied magnetic field is modulated at 250 Hz. The resulting Hall voltage appears at the two heterodyne frequencies and is sampled at 750 Hz for this system. A double-ac system has the advantage of automatically removing the influence of various second order effects which are observed in dc measurements [2,91], so only a single measurement is needed. Unfortunately, the ac system does not produce a definite sign on the Hall voltage. An additional dc Hall measurement was therefore taken whenever the conductivity type of a low mobility sample was in question. Figure 6.1 shows a block diagram of the double-ac Hall system used in this experiment.

If we label the four sample contacts in a clockwise fashion A, B, C, and D, the sheet resistivity  $\rho$  can be expressed as [ ]



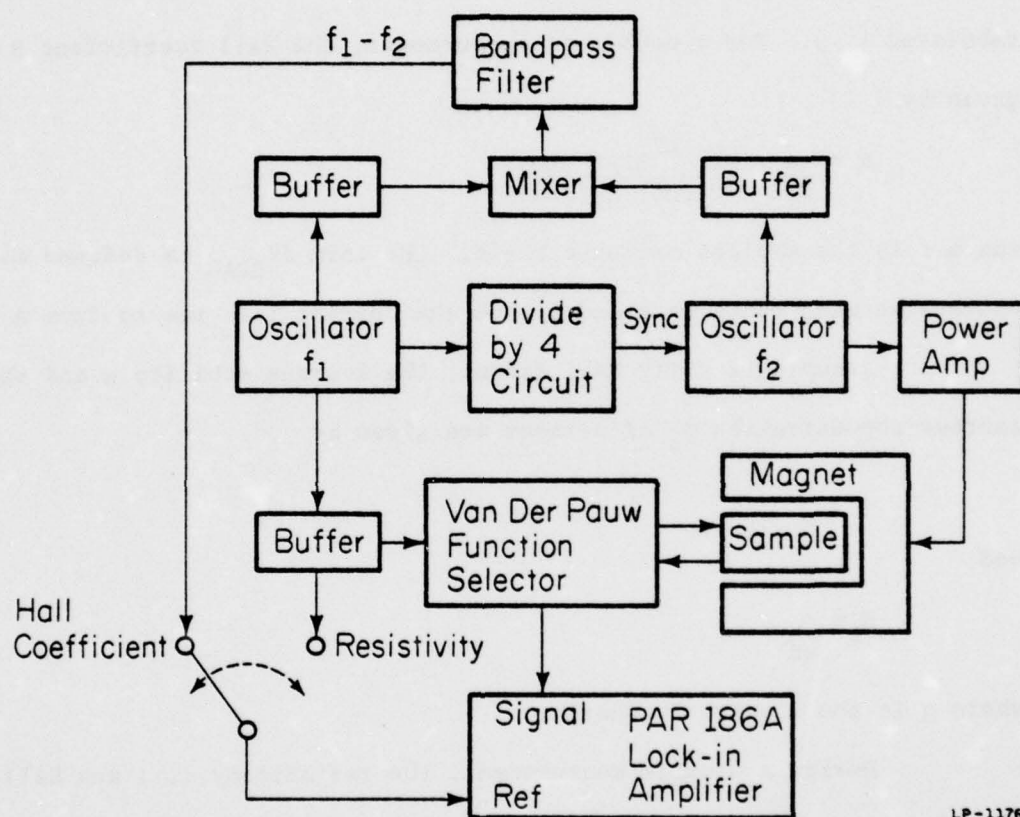


Fig. 6.1. Block diagram of double-ac Hall system.

$$\rho = \frac{\pi}{\ln 2} \left( \frac{R_{ABCD} + R_{BCDA}}{2} \right) f \left( \frac{R_{ABCD}}{R_{BCDA}} \right) \quad (6.1)$$

where  $R_{ABCD}$  is defined as the voltage measured between contacts A and B divided by the current passed from C to D. The other resistances are similarly labeled and the function  $f$  (vander Pauw coefficient) has been tabulated [ ]. For a double-ac measurement, the Hall coefficient  $R$  is given by [ ]

$$R = \frac{\pi}{\ln 2} \frac{\sqrt{2} \Delta V_{BDAC} (rms)}{\beta (rms) \times I (rms)} \quad (6.2)$$

where  $\beta$  is the applied magnetic field. The term  $\Delta V_{BDAC}$  is defined as the voltage between contacts B and D when the current  $I$  is passed from A to C.

Assuming a unity Hall factor, the average mobility  $\mu$  and sheet carrier concentration  $N_s$  of a layer are given by

$$\mu = \frac{R}{\rho} \quad (6.3)$$

and

$$N_s = \frac{1}{qR} \quad (6.4)$$

where  $q$  is the electronic charge.

During a profile measurement, the resistivity ( $\rho$ ) and Hall coefficient ( $R_j$ ) of the implanted layer are determined. A thin region ( $d_j$ ) of the implanted layer is removed after each measurement, and the two quantities ( $\rho_{j-1}$  and  $R_{j-1}$ ) are determined for the remaining implanted layer. The carrier concentration ( $n_j$ ) and the carrier mobility ( $\mu_j$ ) in the layer removed can be expressed as [80]

$$\mu_j = \frac{R_j / \rho_j^2 - R_{j-1} / \rho_{j-1}^2}{1 / \rho_j - 1 / \rho_{j-1}} \quad (6.5)$$

and

$$n_j = \frac{1/\rho_j - 1/\rho_{j-1}}{q d_j \mu_j} \quad (6.6)$$

We have assumed that the measured Hall mobility is identical to the carrier drift mobility [9] for these profiles.

## 6.2. Sample Preparation

Although a number of differing types of implanted GaAs samples were used in this study, the sample preparation followed a common procedure. The sample encapsulation was removed by an HF acid etch after annealing. The  $\text{Si}_3\text{N}_4$  films are very dense and require a much longer etching time than a comparable  $\text{SiO}_2$  encapsulation. The samples were then cleaned with organic solvents prior to contact metalization. The four contacts were evaporated onto the sample through a shadow mask in a square array as illustrated in Figure 6.2. The metal used to make ohmic contacts depends on the conductivity type of the implanted layer. Contacts to p-type layers was made using a Ag - 4% Mn alloy, while either Ag - 4% Sn or Au - 4% Sn metal could use used for n-type layers. No appreciable differences between the silver-based and gold-based alloys were observed for low-resistivity n-type layers. However, the gold-tin alloy makes better contacts to high-resistivity samples.

The contacts were annealed in a reducing atmosphere (flowing  $\text{H}_2$ ) at approximately  $400^\circ\text{C}$  for 10 seconds for both types of GaAs samples. Since the Ge-implanted layers were extremely thin, it was difficult to avoid alloying the contacts through the implanted layer and into the substrate during extended anneal times. This ruins the electrical isolation of a surface layer on a conducting substrate. Therefore, short anneal



times were used to avoid substrate leakage currents for layers implanted onto conducting substrates. In contrast, extended annealing has no observable effect on the electrical measurements of implanted layers in semi-insulating GaAs, because the substrate is not conductive. The arsenic-implanted silicon samples used in electrical measurements were identical to those described in section 5.1. The details of the cleaning and ohmic contact production are described in detail elsewhere [80]. As with the gallium arsenide samples, the samples were cleaned with organic solvents and the contacts were evaporated through a shadow mask. The contact metal was a Au - 1% Sb alloy which was annealed at approximately 400°C for twenty seconds to give ohmic contacts.

The van der Pauw geometry was defined by cutting grooves into the sample after the ohmic contacts were made. The grooves extend through the implanted layer into the substrate and are used to simulate an edge mounting of the contacts. The grooves were defined by mounting the samples onto a shadow mask and using a small abrasive air gun to erode the surface. The leakage current of the implanted layer to the silicon substrates was not substantially increased by the resulting rough surface of the grooves.

For measurement, a sample was mounted using a G.E. varnish (#7031) onto a nylon disc, which fits into the sample holder (Figure 6.2). In this holder, a sample is contacted by four spring loaded pogo stick probes as shown in the insert of Figure 6.2. A guide slot in the nylon disc keeps the sample in a constant position relative to the probes. This configuration allows the sample to be measured, removed, etched, and measured again without a realignment of the probes or the sample.

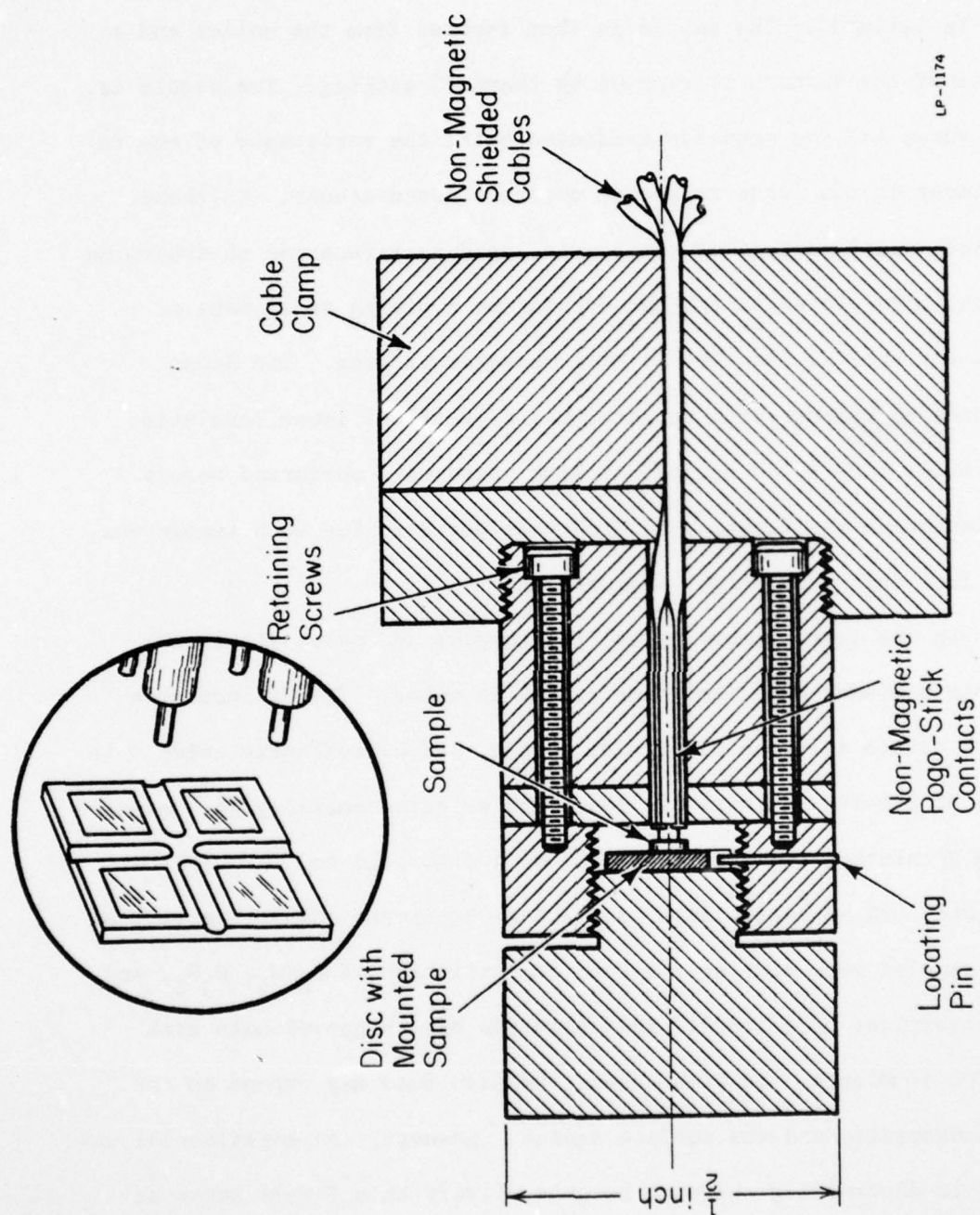


Fig. 6.2. Details of sample holder construction. The sample and nylon holder are inserted into an electromagnet during Hall measurement.

During a profile experiment, a sample's sheet resistance and mobility is measured. The sample is then removed from the holder and a thin layer of the surface is removed by chemical etching. The sample is again measured and the sequence continues until the resistance of the remaining layer is too large to permit accurate measurements. In these experiments, small regions of the sample, used as references to determine etch depth, were protected against etching by applying small dots of black wax (Apiezon W) outside the Hall measurement area. The Sloan Dektak, used to measure step heights, has a practical lower resolution limit of about  $1000 \text{ \AA}$ , so several etching steps were performed before a depth measurement was taken. The etch rate per step for each sample was averaged from this step height measurement.

In the layer removal step, the samples and nylon discs were immersed in a planar etch, and then rinsed in water. The silicon etch used was a dilute solution of nitric, acetic, and hydrofluoric acids. An etch rate of  $230\text{--}580 \text{ \AA/minute}$  was found for an etch combining  $10.4 \text{ ml}$  of a diluted HF mixture (consisting of  $100 \text{ ml}$  acetic acid and  $4 \text{ ml}$  hydrofluoric acid),  $90 \text{ ml}$  acetic acid, and  $300 \text{ ml}$  of nitric acid. The gallium arsenide samples were similarly etched in a solution of  $\text{H}_2\text{SO}_4$ ,  $\text{H}_2\text{O}_2$ , and  $\text{H}_2\text{O}$  in proportions of  $1:1:300$ . This solution has an approximate etch rate of  $200 \text{ \AA/minute}$ . In both cases, the etch rate may depend on the sample conductivity and the surface damage. However, the experimental uncertainty in determining the step heights of very thin layers masks any direct evidence of non-uniform etching.



### 6.3. Arsenic-Implanted Silicon

The heavy-dose arsenic implants into bare silicon showed no appreciable diffusion for low annealing temperatures. The 600°C anneal (Figure 6.3) had an electrical distribution of carriers similar to the atomic profiles. Comparing the two profiles, we observe that the region of the Gaussian distribution above  $2 \times 10^{20} \text{ cm}^{-3}$  is not electrically active. It is difficult to speculate as to whether this is due to solid solubility effects, since the solubility of As in Si at 600°C is not available. The carrier mobility, while seemingly low for electrons, compares very favorably with the measured data of Fair and Tsai [92] for similarly doped silicon.

The samples annealed at 1000°C do not exhibit the simple diffusion of a Gaussian distribution. The atomic and electrical profiles (Figure 6.4) both have a relatively flat region extending  $\sim 2000 \text{ \AA}$  into the sample, and a sharp leading edge. As before, the mobility is consistent with other measured data of arsenic doped silicon [92].

The 600°C anneal shows several interesting features. The heavy implanted dose of arsenic makes the implanted region amorphous in unannealed samples [93]. After a 600°C anneal, the surface has epitaxially regrown on the underlying substrate and the arsenic is incorporated up to a limit of  $\sim 2 \times 10^{20} \text{ cm}^{-3}$ . Thus doped layers can be produced even at very low anneal temperatures. The electron concentration limit is below the solid solubility of arsenic in silicon at this temperature [83]. However, as Fair and Tsai note [92], the electrical and chemical solubility of a species can be defined as separate quantities. Much of the arsenic present at high concentrations is not electrically active.

The 1000°C anneal causes substantial diffusion from the Gaussian

AD-A069 782

ILLINOIS UNIV AT URBANA-CHAMPAIGN COORDINATED SCIENCE LAB F/G 20/12  
ATOMIC AND ELECTRICAL PROFILE STUDIES OF ION-IMPLANTED SEMICONDUCTORS (U)  
DEC 78 G T MARCYK  
R-835  
DAAB07-72-C-0259

UNCLASSIFIED

2 OF 2  
AD  
A069782

NL







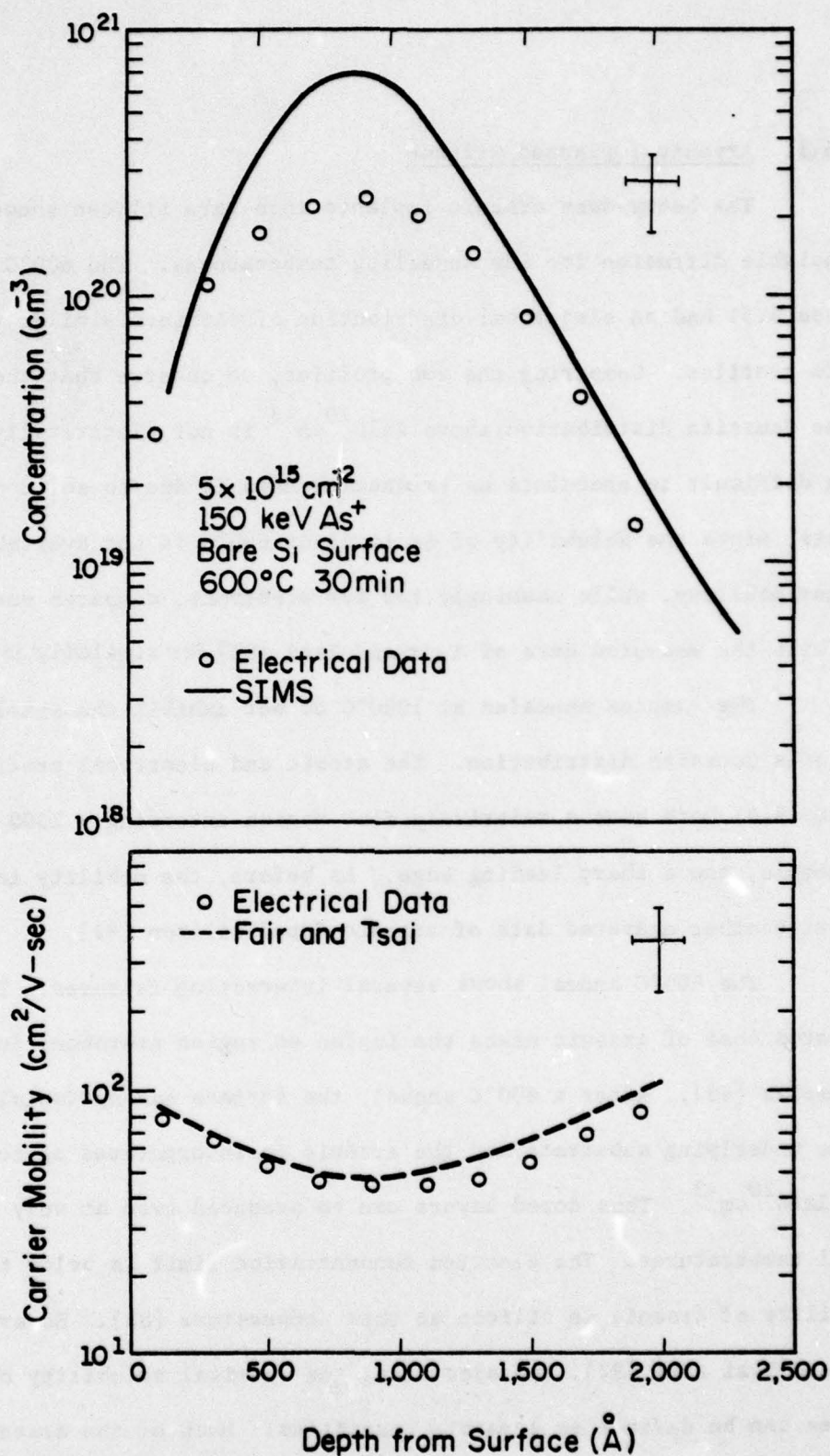


Fig. 6.3. Electrical and SIMS profiles of As-implanted Si after 600°C anneal [80]. The carrier mobility is compared to the experimental values obtained by Fair and Tsai [92].

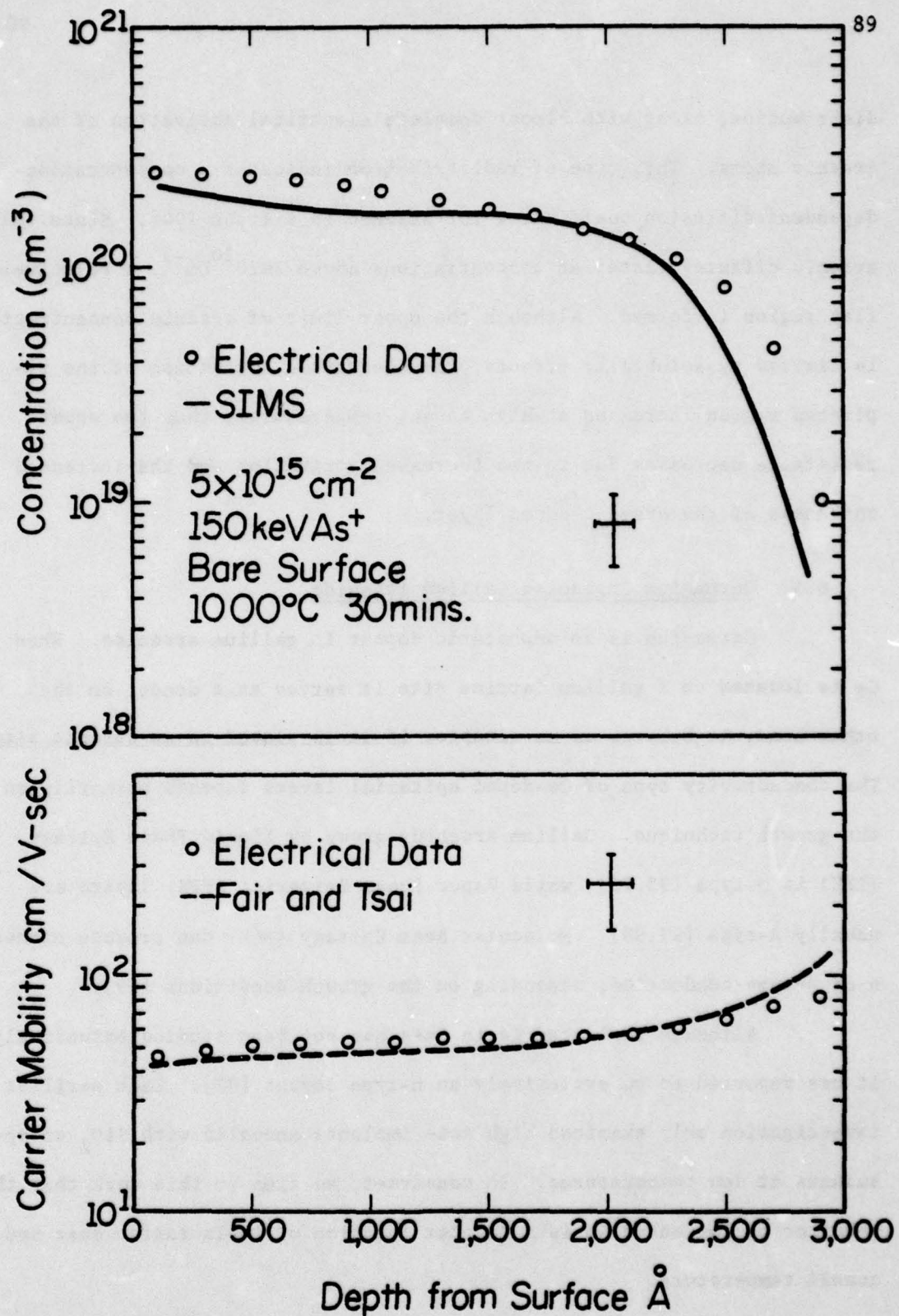


Fig. 6.4. Electrical and SIMS profiles of As-implanted samples after 1000°C anneal for 30 minutes [80].

LP-1277

distribution, along with almost complete electrical activation of the arsenic atoms. This type of redistribution indicates a concentration-dependent diffusion coefficient for arsenic in silicon [94]. Since the arsenic diffuses faster at concentrations above  $2 \times 10^{20} \text{ cm}^{-3}$ , a relatively flat region is formed. Although the upper limit of arsenic concentration is limited by solubility effects, the electrical activation of the implanted region increases at high anneal temperatures; thus the sheet resistance decreases due to the increased activation and the increased thickness of the arsenic-doped layer.

#### 6.4. Germanium Implanted Gallium Arsenide

Germanium is an amphoteric dopant in gallium arsenide. When Ge is located on a gallium lattice site it serves as a donor; on the other hand, it behaves as an acceptor if it is placed on an arsenic site. The conductivity type of Ge-doped epitaxial layers depends primarily on the growth technique. Gallium arsenide grown by Liquid Phase Epitaxy (LPE) is p-type [95,96], while Vapor Phase Epitaxial (VPE) layers are usually n-type [97,98]. Molecular Beam Epitaxy (MBE) can produce either n or p-type conduction, depending on the growth conditions [99].

Although implanted Ge in GaAs has not been studied extensively, it has reported to be exclusively an n-type dopant [87]. That earlier investigation only examined high dose implants annealed with  $\text{SiO}_2$  encapsulants at low temperatures. In contrast, we find in this work that the behavior of implanted Ge is a complex function of implantation dose and anneal temperature.

Chromium-doped semi-insulating GaAs was used for these Ge implantation studies, since we could not predict what the conductivity type



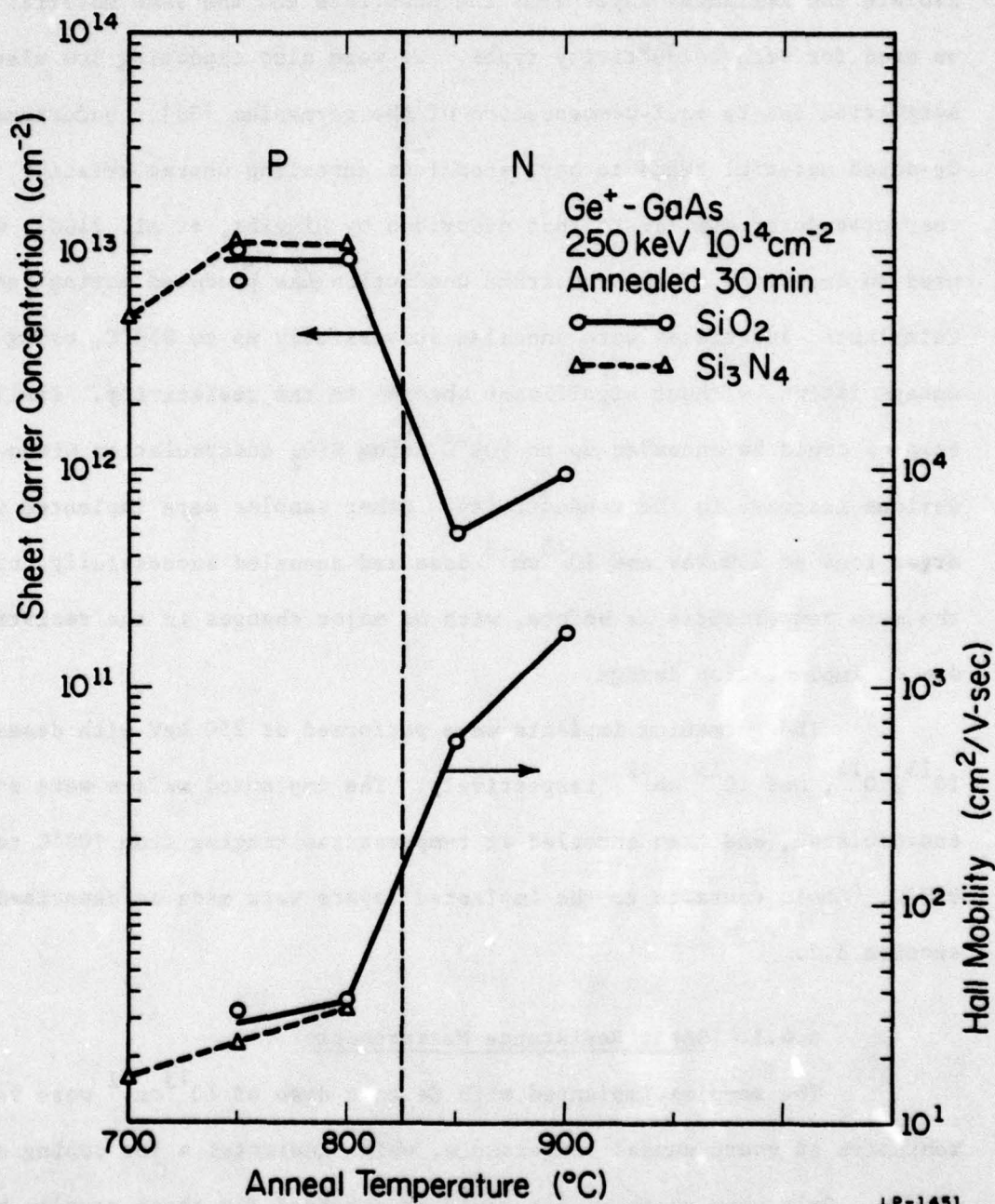
would be. Thus there was no need to form p-n junctions to electrically isolate the implanted layer from the substrate and the same material could be used for both conductivity types. We were also expecting low electrical activation due to self-compensation of the germanium [78]. Unfortunately, Cr-doped material tends to have anomalous annealing characteristics. A test procedure, similar to that described by Higgins, et al. [100], was used to determine if any substrate conduction was produced during annealing. Unimplanted substrates were annealed successfully up to 850°C, using  $\text{Si}_3\text{N}_4$  encapsulation, without significant changes in the resistivity. Similar samples could be annealed up to 900°C using  $\text{SiO}_2$  encapsulation without a serious increase in the conductivity. Other samples were implanted with argon ions at 200 keV and  $10^{15} \text{ cm}^{-2}$  dose and annealed successfully, up to the same temperatures as before, with no major changes in the resistivity due to implantation damage.

The germanium implants were performed at 250 keV with doses of  $10^{13}$ ,  $10^{14}$ , and  $10^{15} \text{ cm}^{-2}$ , respectively. The implanted wafers were scribed, encapsulated, and then annealed at temperatures ranging from 700°C to 900°C. Ohmic contacts to the implanted layers were made as described in section 6.2.

#### 6.4.1. Sheet Resistance Measurements

The samples implanted with Ge to a dose of  $10^{13} \text{ cm}^{-2}$  were very resistive at every anneal temperature, which indicates a low doping efficiency. Only very sketchy data could be obtained for these samples because of their large resistances, and this data is not presented here.

Samples implanted with  $10^{14} \text{ cm}^{-2}$  dose illustrate the amphoteric nature of germanium (Figure 6.5). Such samples annealed at temperatures



LP-1451

Fig. 6.5. Iso chroanal anneals of 10<sup>14</sup> cm<sup>-2</sup> implanted GaAs and samples co-implanted with argon. The doubly-implanted samples are n-type at all anneal temperatures.



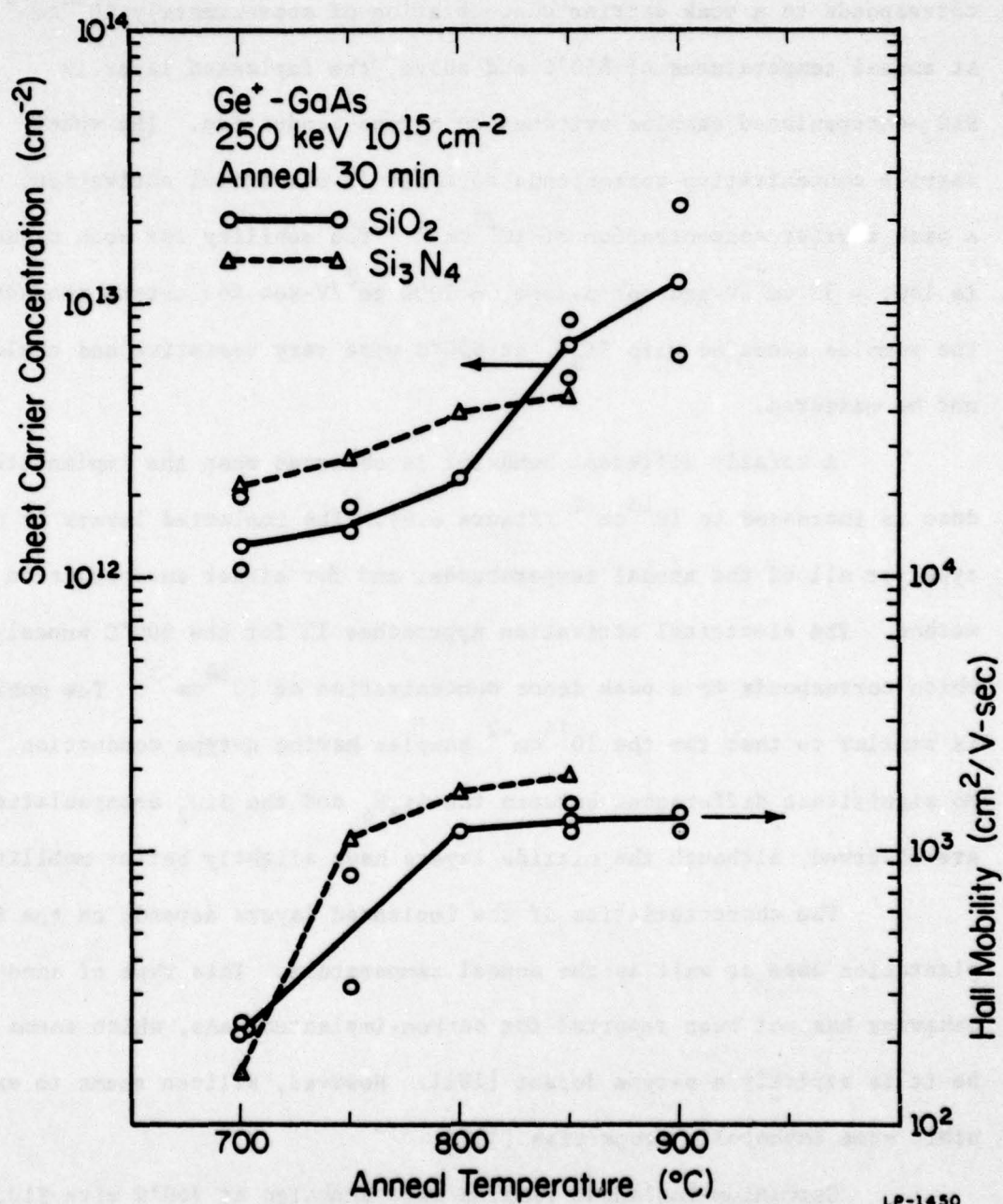
below 850°C were p-type, with about 10% electrical activation. This corresponds to a peak carrier concentration of approximately  $10^{18} \text{ cm}^{-3}$ . At anneal temperatures of 850°C and above, the implanted layer in  $\text{SiO}_2$ -encapsulated samples switches to n-type conduction. The sheet carrier concentration corresponds to about 1% electrical activation, or a peak carrier concentration of  $10^{17} \text{ cm}^{-3}$ . The mobility for both cases is low;  $\sim 30 \text{ cm}^2/\text{V-sec}$  for p-type,  $\sim 1000 \text{ cm}^2/\text{V-sec}$  for n-type conduction. The samples annealed with  $\text{Si}_3\text{N}_4$  at 850°C were very resistive and could not be measured.

A totally different behavior is observed when the implantation dose is increased to  $10^{15} \text{ cm}^{-2}$  (Figure 6.6). The implanted layers is n-type for all of the anneal temperatures, and for either encapsulation method. The electrical activation approaches 1% for the 900°C anneal, which corresponds to a peak donor concentration of  $10^{18} \text{ cm}^{-3}$ . The mobility is similar to that for the  $10^{14} \text{ cm}^{-2}$  samples having n-type conduction. No significant differences between the  $\text{Si}_3\text{N}_4$  and the  $\text{SiO}_2$  encapsulations are observed, although the nitride layers have slightly better mobilities.

The characteristics of the implanted layers depends on the implantation dose as well as the anneal temperature. This type of annealing behavior has not been reported for carbon-implanted GaAs, which seems to be it is strictly a p-type dopant [101]. However, silicon seems to exhibit some amphoteric properties [102].

Germanium-implanted samples were annealed at 900°C with  $\text{SiO}_2$  encapsulation to determine if the n-type conduction was related to the production of gallium vacancies. The  $\text{SiO}_2$  encapsulation permits gallium vacancies in the sample. Since Ge a donor when on a gallium site, the n-





LP-1450

Fig. 6.6. Sheet carrier concentration of GaAs samples implanted with  $10^{15}$  cm<sup>-2</sup> dose of Ge. All of the samples are n-type

type conductivity should increase with anneal time. However, the sheet carrier concentration of the  $10^{15} \text{ cm}^{-2}$  implant (Figure 6.7) is almost constant with varying anneal times. The  $10^{14} \text{ cm}^{-2}$  samples show a similar behavior. Thus we can conclude, surprisingly, that the outdiffusion of gallium has little effect on the electrical activation at these temperatures.

Unequal amounts of radiation damage could lead to the differences in the two sets of implanted samples ( $10^{14}$  or  $10^{15} \text{ cm}^{-2}$  dose). A set of samples implanted with Ge at  $10^{14} \text{ cm}^{-2}$  was co-implanted with argon at 150 keV energy and to a  $5 \times 10^{15} \text{ cm}^{-2}$  fluences to determine if the n-type behavior of the higher Ge doses was due to changes in the damage. The argon energy was chosen to produce the same projected range as the Ge implants. As observed in Section 6.1, the implanted argon does not alter directly the electrical properties of the substrate. The additional damage created by the argon implant has a pronounced effect on the annealing characteristics, as seen in Figure 6.8. The dual implanted sample shows only n-type conduction, in contrast to the single Ge implant which produces both n and p layers. The mobility of the carrier in the doubly-implanted layer is much lower than for a single  $10^{14} \text{ cm}^{-2}$  implant. This suggests strongly that the n-type conduction observed for higher doses is related to the amount of damage produced in the implanted layer.

#### 6.4.2. Depth Profiles

The depth profiles of the carrier concentration are very different from the Ge atomic distributions. Only a small portion of the implanted layer is electrically active in the  $10^{14} \text{ cm}^{-2}$  samples annealed at  $800^\circ\text{C}$  (Figure 6.9). The hole concentration increases from a low initial

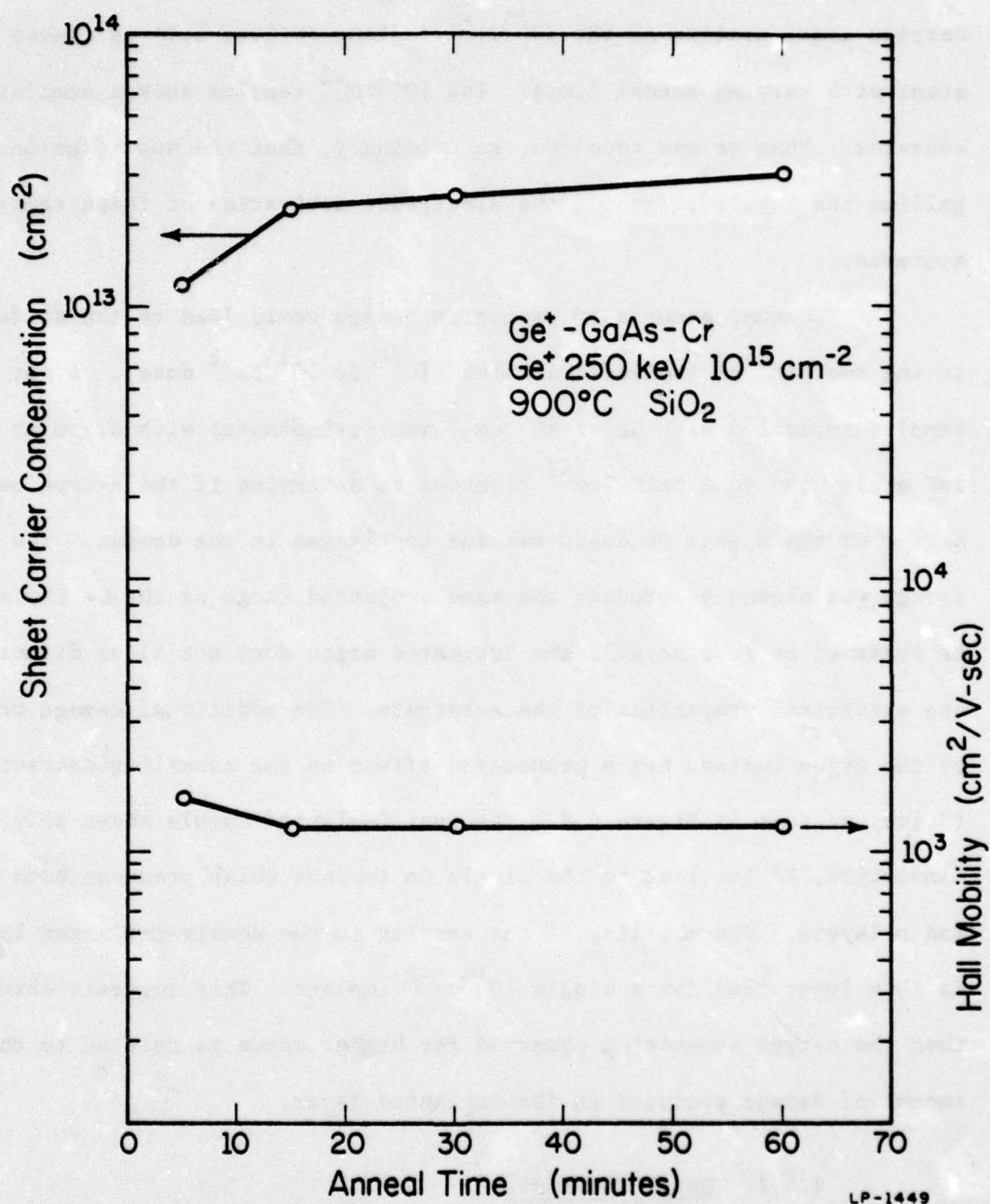
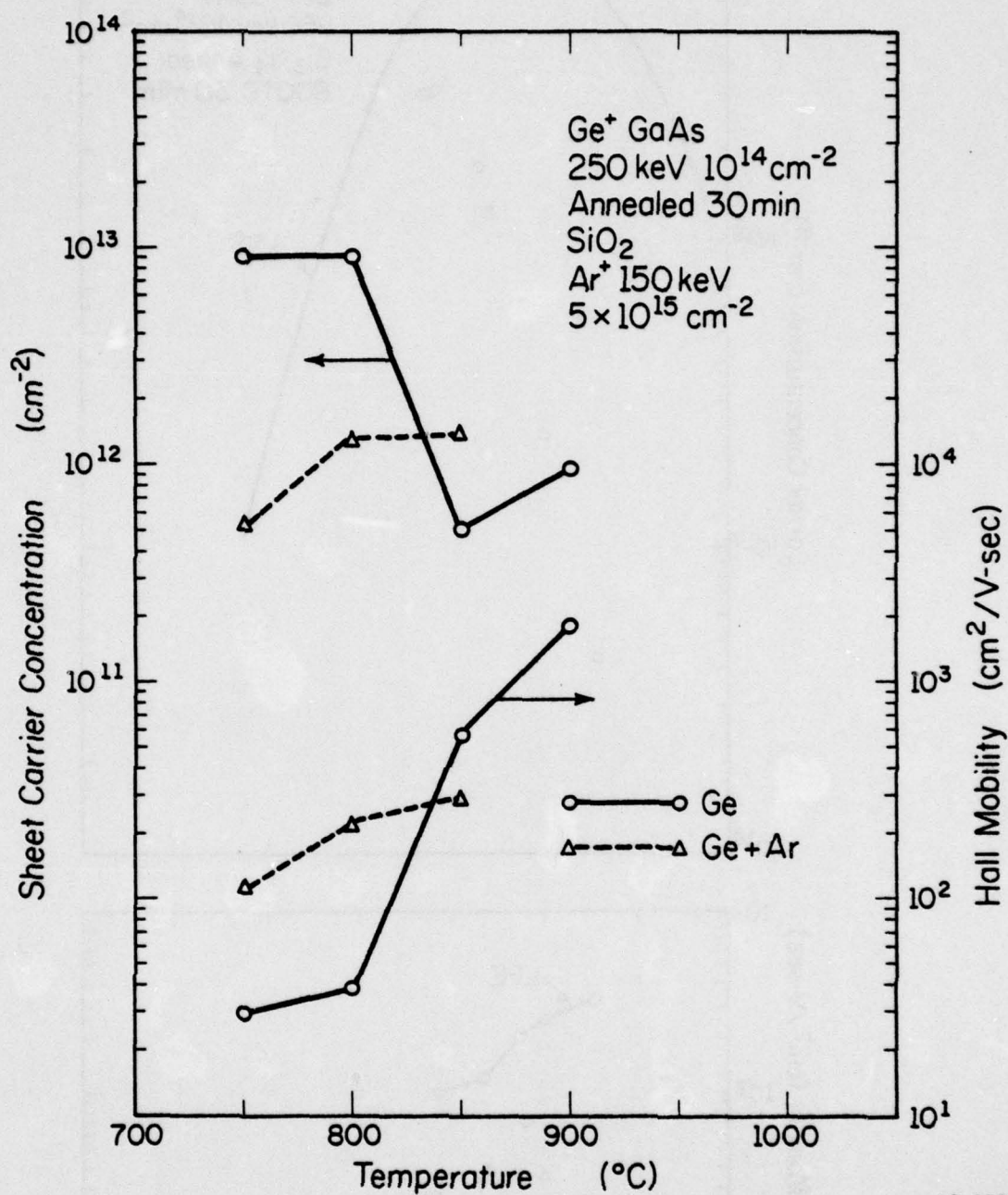


Fig. 6.7. Isothermal anneal of Ge-implanted GaAs.





LP-1447

Fig. 6.8. Sheet carrier concentration of Ge-implanted GaAs at  $10^{14} \text{ cm}^{-2}$  dose. The samples annealed below  $850^{\circ}\text{C}$  are p-type, while those annealed at  $850^{\circ}\text{C}$  or higher are n-type.

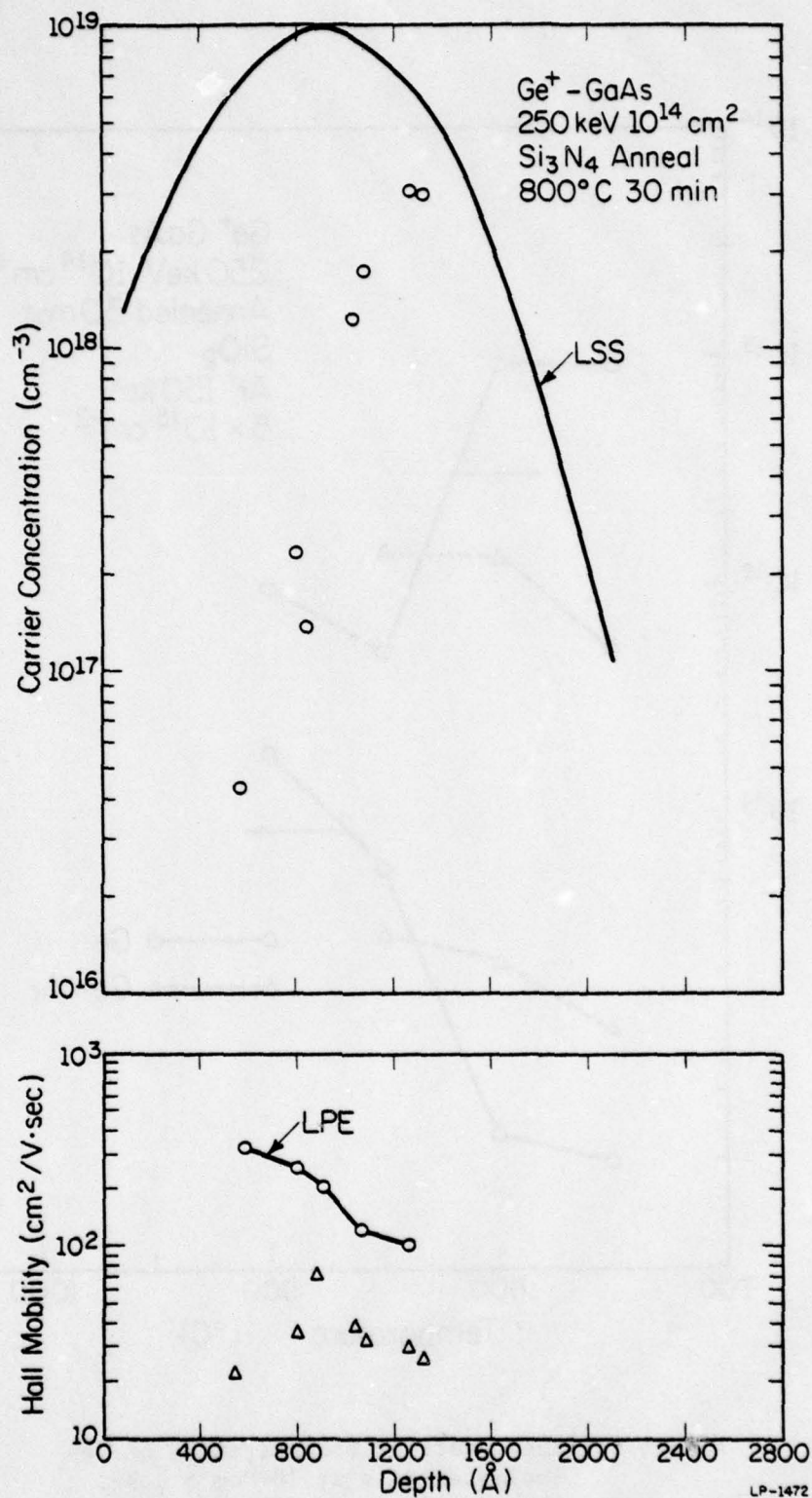


Fig. 6.9. Electrical profiles of  $10^{14}$  cm<sup>-2</sup> implanted GaAs annealed at 800°C for 30 minutes. The hole mobility is compared to similarly doped LPE layers [96].

value and then, surprisingly, ends abruptly. Similar behavior has been observed in silicon implanted layers [102]. The abrupt end to the distribution for silicon implants has been attributed to the formation of a p-n junction within a single implanted layer. To determine if another active layer exists for germanium implants, samples were etched in a  $\text{H}_2\text{SO}_4\text{-H}_2\text{O}_2\text{-H}_2\text{O}$  solution, as before, to remove part of the implanted layer. Then n-type contacts were evaporated and alloyed onto the etched surface. Layers of various thicknesses were removed in the etch sequence, and n-type activity was not observed at any depth.

The samples implanted at  $10^{15}\text{ cm}^{-2}$  dose have a completely different type of carrier profile. A sample annealed at  $900^\circ\text{C}$  (Figure 6.10) has a flat region of electrical activity, with an electron concentration of  $\sim 10^{17}\text{ cm}^{-3}$ . As with the previous dose, the surface layer is relatively inactive. The n-type conduction (Figure 6.10) seems to occur at a greater depth than the p-type conduction (Figure 6.9).

We are not able to explain these complex and puzzling depth profiles. However, the differences in the regions of electrical activity suggest that the conductivity type is influenced by the amount of lattice damage. It is clear that the germanium tends to be incorporated onto gallium sites (thus becoming a donor) when a particularly heavy damaged region is annealed. The details of these effects will not be understood without an extensive study of impurity-defect interactions.

#### 6.4.3. Implanted Diodes

The most important test of ion implantation doping is the production of actual devices. In this work, Ge-implanted p-n junctions diodes were fabricated using the implanted region as either an n or p type region.



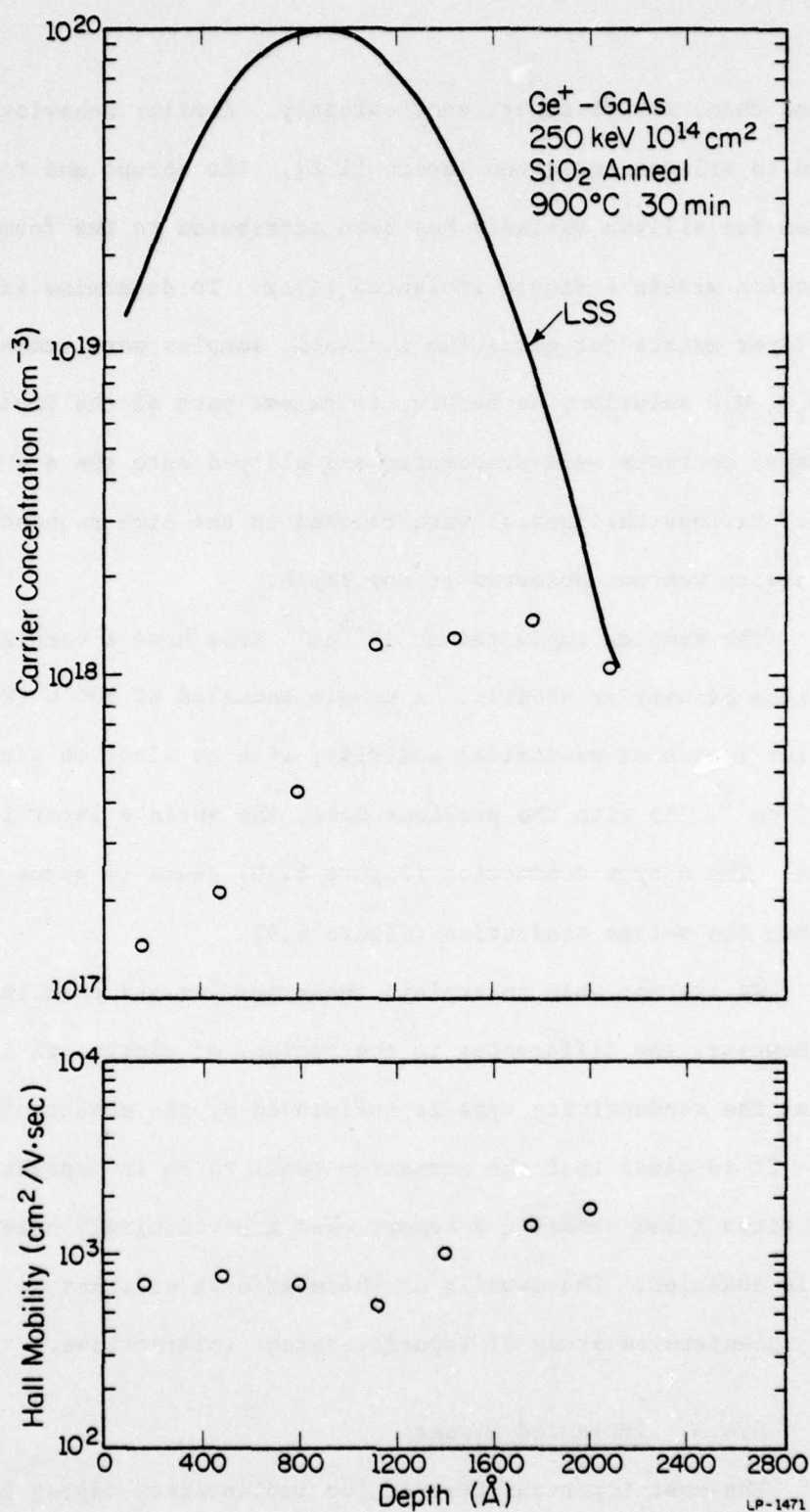
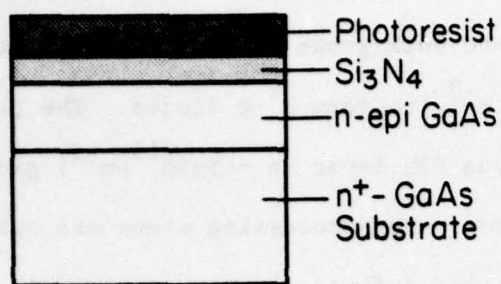


Fig. 6.10. Electrical profile of 10<sup>15</sup> cm<sup>-2</sup> implanted GaAs annealed at 900°C for 30 minutes.

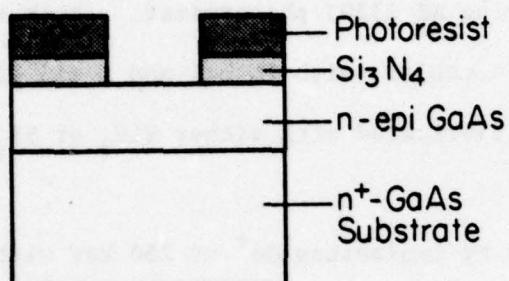
The n-type regions were implanted into bulk grown Cd-doped substrates having a hole concentration of  $10^{17} \text{ cm}^{-3}$ , to form  $n^+$ -p diodes. The p-type regions, implanted into an n-type VPE layer ( $n \sim 5 \times 10^{15} \text{ cm}^{-3}$ ) grown on a  $n^+$  substrate, form  $p^+$ -n- $n^+$  diodes. The processing steps are outlined in Figure 6.11. The junctions are defined using the standard photolithographic techniques involving AZ 1350J photoresist. Both the diodes and the metal contacts were circular, with 10 mil and 5 mil diameters, respectively. Diodes were fabricated with either  $\text{SiO}_2$  or  $\text{Si}_3\text{N}_4$  as the encapsulants.

The  $n^+$ -p diodes were made by implanting  $\text{Ge}^+$  at 250 keV with  $10^{15} \text{ cm}^{-2}$  fluence into the p-type substrate. Recall that this dose produces n-type layers for all annealing temperatures. The reverse bias current versus voltage graph (I-V) in Figure 6.12 shows a substantial increase in the leakage current for the higher anneal temperatures. These diodes were made using  $\text{SiO}_2$  encapsulation. The ohmic behavior at low bias voltages agrees with previous studies of Be implanted diodes [103] annealed with  $\text{SiO}_2$  encapsulation. However, the ohmic leakage can be minimized by low temperature ( $\sim 300^\circ\text{C}$ ) processing. The breakdown voltage of 9 volts is slightly lower than the predicted value of 15 volts for this heavily doped junction [9].

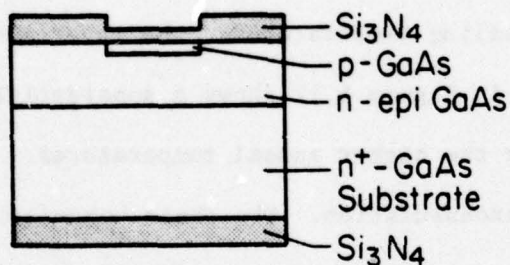
The  $p^+$ -n- $n^+$  diodes studied here were produced by implanting Ge at the same energy of 250 keV to a dose of  $10^{14} \text{ cm}^{-2}$ . A p-type layer is formed for this dose for anneal temperatures below  $850^\circ\text{C}$  (see Figure 6.5). The breakdown voltage (Figure 6.13) for a junction in this lightly doped VPE layer is higher than that for the  $n^+$ -p diode, as expected. These diodes were formed using  $\text{Si}_3\text{N}_4$  encapsulation, and as a result very little



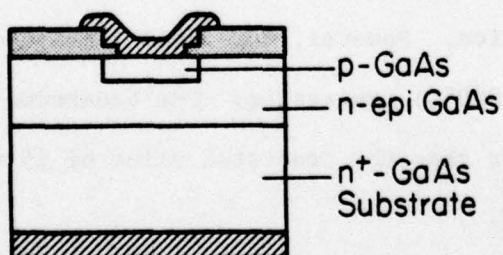
Encapsulate sample with  $\text{Si}_3\text{N}_4$  and apply photoresist.



Expose PR with a suitable mask, develop and open windows in  $\text{Si}_3\text{N}_4$ .  
Ion implant Ge.



Strip photoresist, encapsulate with  $\text{Si}_3\text{N}_4$  and anneal.



Open contact windows, evaporate and define Ag-Mn for top contact and Ag-Sn for back contact.

LS-1380

Fig. 6.11. Fabrication sequence for Ge-implanted  $p^+-n-n^+$  diodes. Silicon dioxide may be substituted for the  $\text{Si}_3\text{N}_4$  as an encapsulant. A similar procedure, with appropriate contacts, is used for  $n^+-p$  diodes.



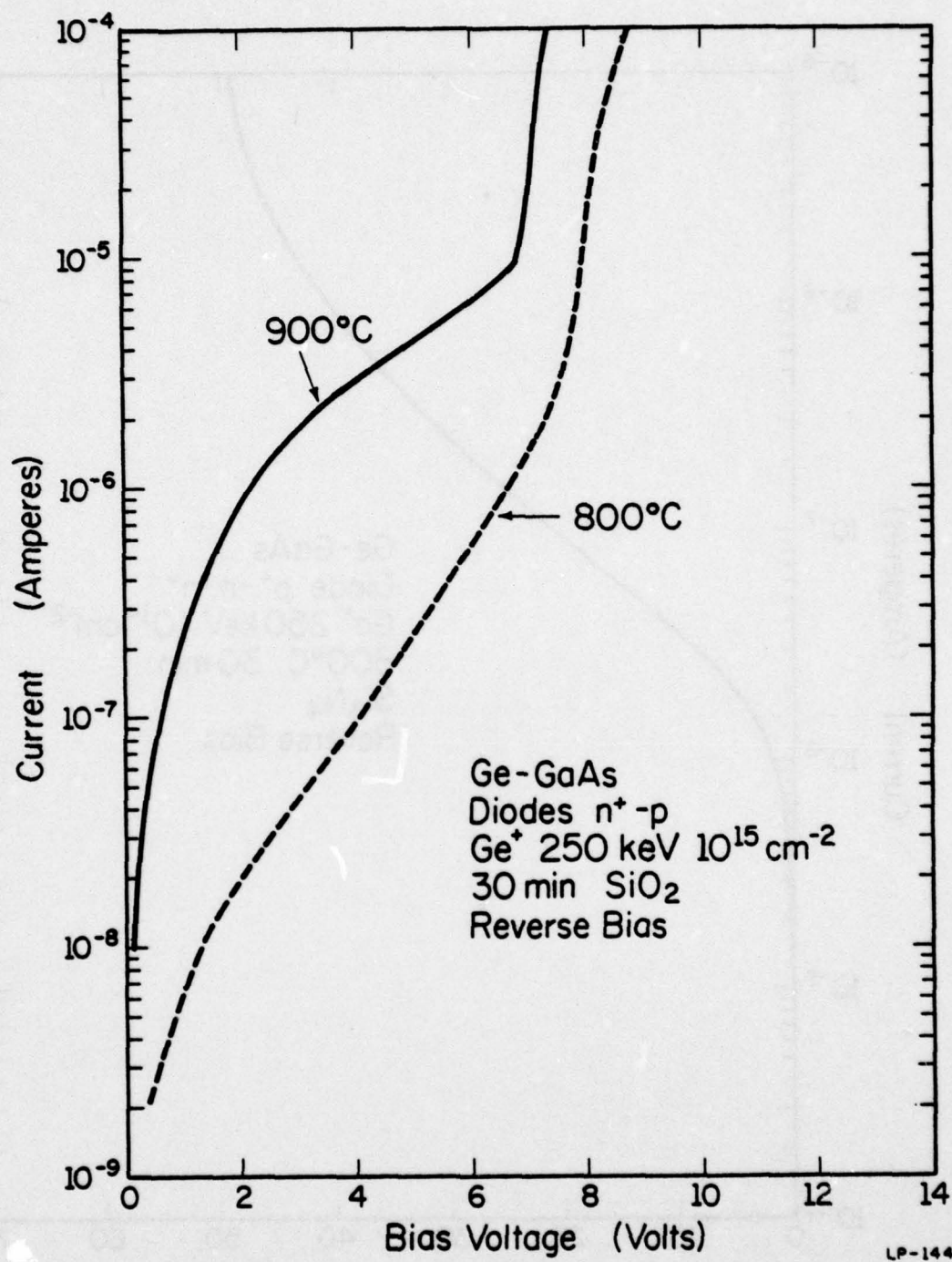


Fig. 6.12. Comparison of reverse-bias currents of  $SiO_2$  encapsulated diodes annealed at 800°C and 900°C.

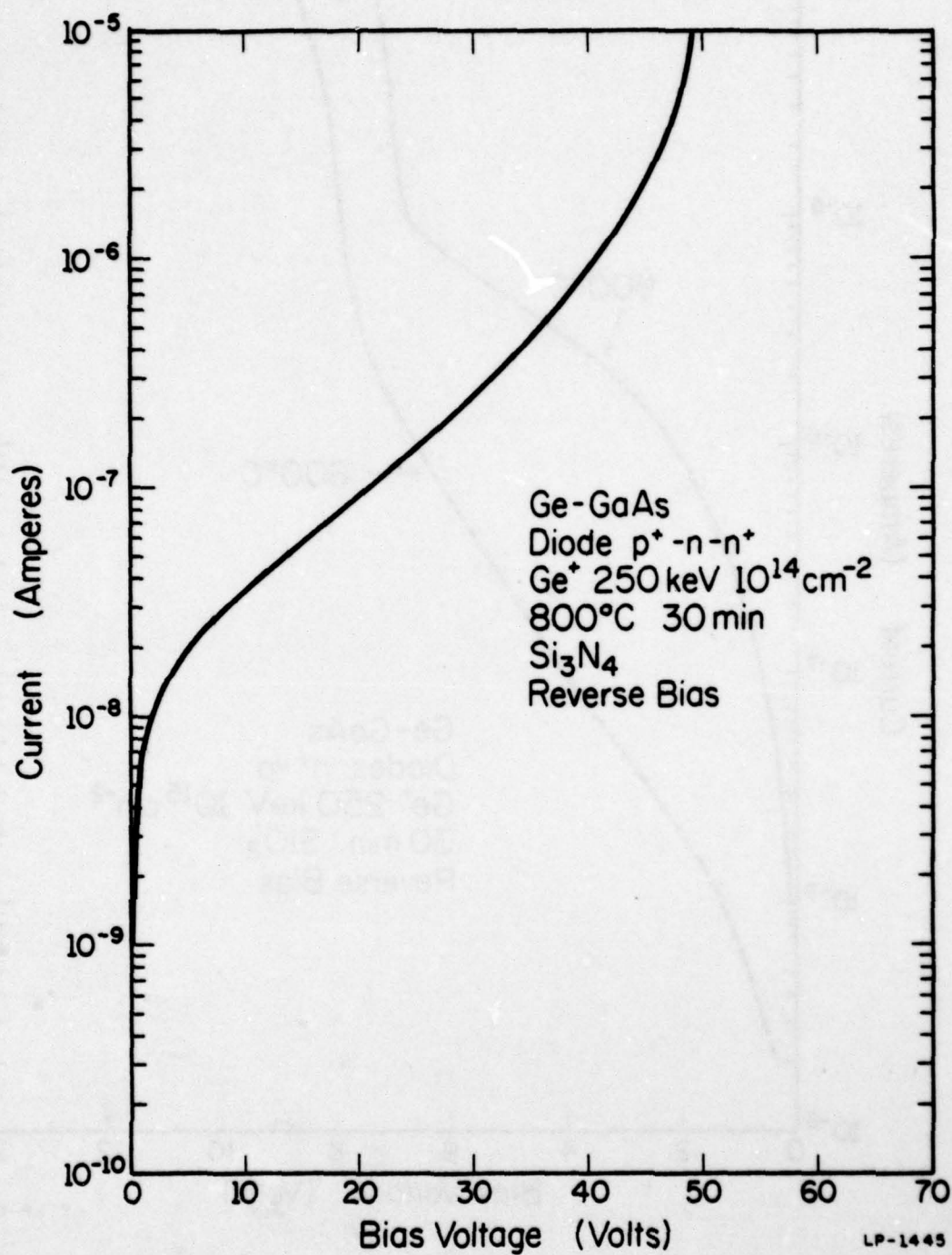


Fig. 6.13. Reverse-bias characteristic of Ge-implanted diode using  $Si_3N_4$  encapsulation.

ohmic component is observed. However, the diodes with the best breakdown characteristics were similarly implanted but encapsulated with  $\text{SiO}_2$  (Figure 6.14). The breakdown region of the curve ( $\sim 180$  V.) is not shown because of the limitations of the current generator used to produce the bias current. The reverse bias plot (Figure 6.15) for this diode shows two distinct regions; the ohmic leakage below 5V bias, and the rectifying portion above 10V. The current in the rectifying region varies as  $V^{0.65}$ , which is a higher voltage dependence than the  $V^{0.5}$  relationship expected for current generated completely in the depletion region of the junction [104].

We are able to fabricate either p-n or n-p junctions with the same implant energy and anneal temperature. The choice of dose determines the conductivity type of the implanted layer. Unfortunately, we were not able to make diodes with  $10^{14} \text{ cm}^{-2}$  dose at anneal temperatures higher than  $800^\circ\text{C}$ . Since the substrate was so heavily doped, we were probably unable to type-convert the surface region. Both  $\text{SiO}_2$  and  $\text{Si}_3\text{N}_4$  were used successfully as encapsulants for the diodes. The nitride encapsulation produces less ohmic leakage in the junction compared with oxide encapsulation. In the case of  $p^+-n$  diodes annealed at  $800^\circ\text{C}$ , the oxide encapsulated samples had better breakdown voltages than the nitride-encapsulated samples. We believe this is due to processing variations rather than any fundamental limitation of the nitride for annealing protection.

#### 6.5. Conclusions

Germanium implanted into gallium arsenide displays a true amphoteric behavior. The conductivity type of the implanted layer is a



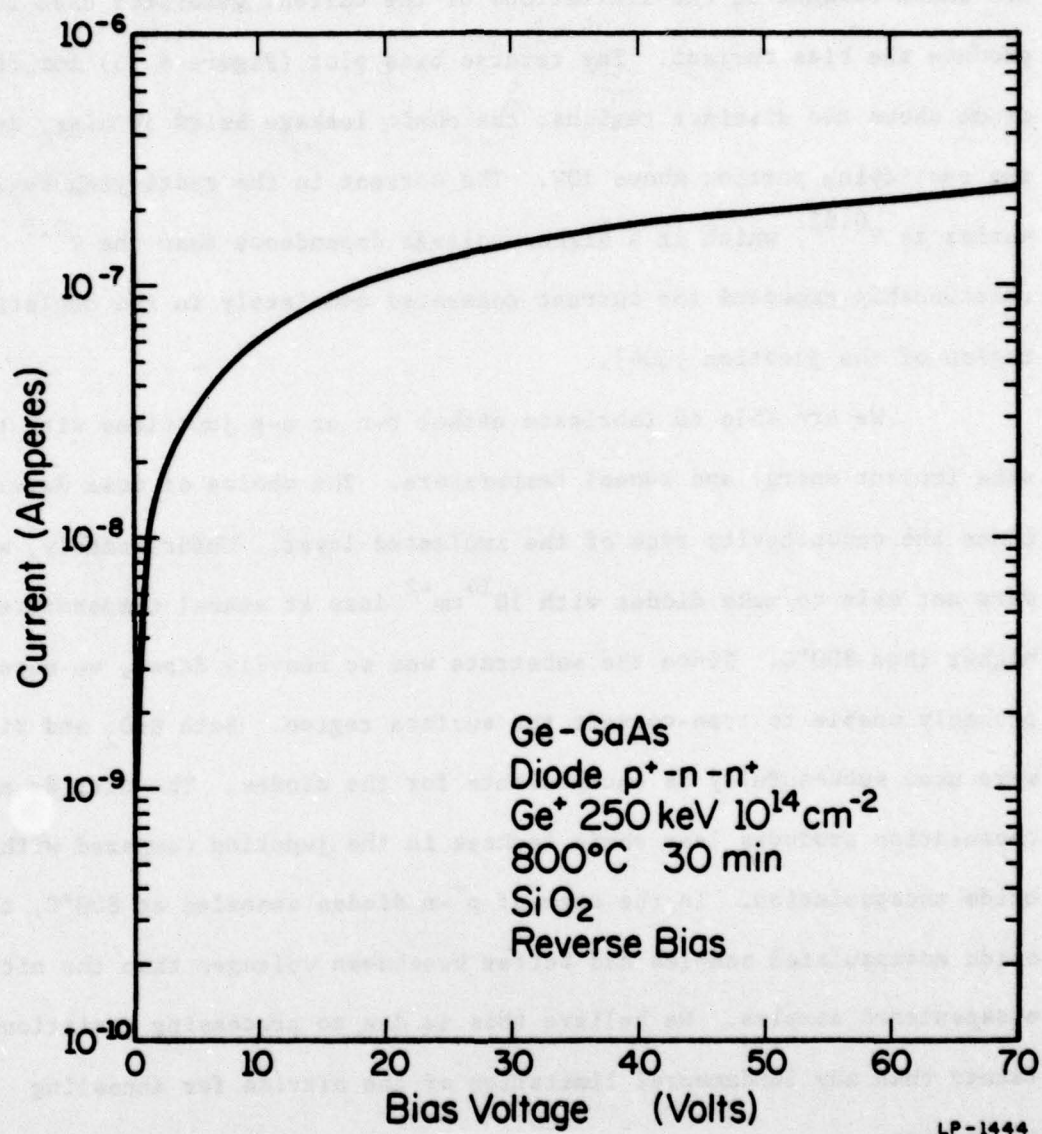


Fig. 6.14. Reverse characteristics of Ge-implanted diode in  $p^+-n-n^+$  configuration. Avalanche breakdown occurs at  $\sim 180\text{v}$ .

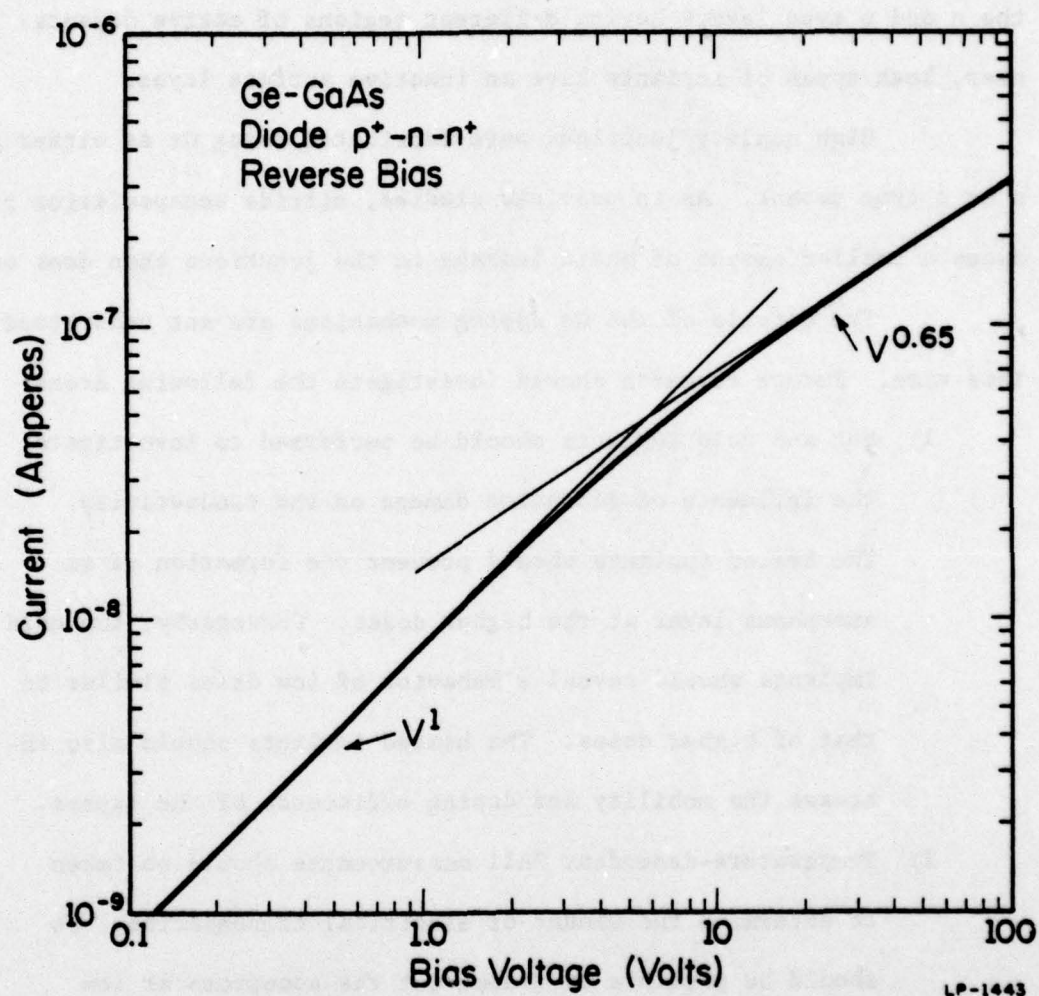


Fig. 6.15. Reverse characteristics of Ge-implanted diode annealed with  $SiO_2$  at  $800^\circ C$  for 30 minutes.

complex function of the implantation dose and the annealing temperature. High implant doses and the high anneal temperatures produce n-type layers, whereas lower doses and temperatures favor p-type conduction. Only a small portion of the implanted distribution is electrically active, with the n and p type layers having different regions of active dopants. However, both types of implants have an inactive surface layer.

High quality junctions were fabricated using Ge as either an n or p type dopant. As in previous studies, nitride encapsulation produces a smaller amount of ohmic leakage in the junctions than does oxide.

The details of the Ge doping mechanisms are not understood at this time. Future research should investigate the following areas:

- 1) Hot and cold implants should be performed to investigate the influence of radiation damage on the conductivity. The heated implants should prevent the formation of an amorphous layer at the higher doses. Conversely, the cold implants should reveal a behavior of low doses similar to that of higher doses. The heated implants should also increase the mobility and doping efficiency of the layers.
- 2) Temperature-dependent Hall measurements should be taken to determine the amount of electrical compensation. It should be possible to freeze out the acceptors at low temperatures, and to determine the total number of active impurities.
- 3) Photoluminescence (PL) from the implanted layers should be compared with the electrical measurements. The PL data can be used to determine if complete annealing of the im-



p       planted layers occurs and if any donor-acceptor complexes are formed. Germanium may be an efficient recombination site in GaAs.

- 4) Co-implantation with other impurities should be explored to increase the doping efficiency. Co-implants with arsenic or phosphorus should increase the n-type conduction, while gallium or aluminum should enhance the p-type activity.
- 5) Since Ge is an amphoteric dopant with a very small diffusion coefficient, it may be possible to reduce the contact resistance of light emitting diodes and other devices by a suitable Ge implant. If the lack of electrical activation near the surface can be overcome, a shallow Ge-doped layer could improve the characteristics of the metal contacts to GaAs and related materials such as  $\text{GaAs}_{1-x}\text{Px}$ .
- 6) We cannot stress too strongly the importance of good substrate material. High quality GaAs, which does not have annealing problems, is essential to the study of dopants with low activations, such as germanium. Therefore high-quality epitaxial layers or carefully qualified bulk samples should be used in such studies.

REFERENCES

- 1) J. Sansbury, "Applications of Ion Implantation in Semiconductor Processing," Sol. State Tech., vol. 19, No. 11, pp. 31-43, 1976.
- 2) W. V. McLevige, P. R. Chatterjee, and B. G. Streetman, "Versatile double-ac system for profiling impurities in semiconductors," J. Phys. E., vol. 10, pp. 335-337, 1977.
- 3) J. Greene and J. Whalen, "Glow discharge Optical Spectroscopy for the analysis of thin films," J. Appl. Phys., vol. 44, pp. 2509-2513, 1973.
- 4) S. Lindhard, M. Schraff, and H. Schiott, "Range concepts and heavy ion ranges," Mat. Fys. Medd. Dan. Vid. Selsk., vol. 33, pp. 1-39, 1963.
- 5) J. F. Gibbons, "Ion implantation in semiconductors, Part I," Proc. IEEE, vol. 56, pp. 295-318, 1968.
- 6) J. W. Mayer, L. Erikscon, and J. A. Davies, Ion Implantation in Semiconductors, Silicon and Germanium, New York: Academic Press, 1970.
- 7) J. F. Gibbons, W. S. Johnson, and S. W. Mylroie, Projected Range Statistics, 2nd edition, Stroudsburg, Penn: Halstead Press, 1975.
- 8) J. F. Gibbons and S. Y. Mylroie, "Estimation of impurity profiles in ion implanted amorphous targets using joined half-Gaussian Distributions," Appl. Phys. Lett., vol. 22, pp. 568-569, 1973.
- 9) S. M Sze, Physics of Semiconductor Devices, New York: Wiley-Interscience, 1969.
- 10) L. J. van der Pauw, "A method of measuring specific resistivity and Hall effect of discs of arbitrary shapes," Phillips Res. Reports, vol. 13, pp. 1-9, 1958.
- 11) R. Behrish, International Conference on ion surface interactions, sputtering, and related phenomena, 1972, London: Gordon and Breach, 1973.
- 12) N. Treitz, "Analysis of solid surface monolayers by mass and energy spectrometry methods," J. Phys. E., vol. 10, pp. 573-585, 1977.
- 13) An excellent review of analytical techniques may be found in: Surface Analysis of Silicon Devices, NBS SPECIAL PUBLICATION 400-27, A. G. Lieberman, ed., WASHINGTON: National Bureau of Standare, 1976.



- 14) For example, P. Blood, "Annealing of Room Temperature implants of Indium in Silicon," in Ion Implantation in Semiconductor, 1976, F. Cherrow, J. A. Borders, and D. K. Brice eds., New York: Plenum 1977.
- 15) For example, A. Hihaki, M. Iwami, K. Shuto, T. Saegusa, T. Narusawa, K. Gamo, and S. Namba, "High Dose Implantation of Au and Cu into Si studied by Auger electron and backscattering spectroscopies," *ibid.*
- 16) For example, J. C. C. Tsai, and J. M. Morabito, "In-Depth Profile Detection Limits of Nitrogen in GaP, Nitrogen and Fluorine in Si by SIMS and AES," in Ion Implantation in Semiconductors, S. Namba, ed., New York: Plenum, 1975.
- 17) S. Luduck, L. Scharpen, and H. E. Weaver, "Measurement of Arsenic Implantation Profiles in Silicon using Auger Electron Spectroscopic Technique," *ibid.*
- 18) H. Liebl, "Ion Probe Microanalysis" J. Phys. E., vol. 8, pp. 797-809, 1975.
- 19) C. A. Evans, Jr., "Secondary Ion Mass Analysis: A technique for Three Dimensional Characterization," Anal. Chem., vol. 44, pp. 67A-80A, 1972.
- 20) J. Cobine, Gaseous Conductors, New York: McGraw-Hill, 1941.
- 21) F. Penning, Electrical Discharges in Gases, New York: McGraw-Hill, 1957.
- 22) A. von Engel, Ionized Gases, Oxford: Clarendon Press, 1965.
- 23) S. C. Brown, Introduction to Electrical Discharges in Gases, New York: Wiley, 1966.
- 24) M. M Shakin, "Ion-molecule interaction in the cathode region of a glow discharge," J. Chem. Phys., vol. 43, pp. 1798-1805, 1965.
- 25) W. R. Grove, "On the Electro-Chemical Polarity of Gases," Phil. Trans. Roy. Soc. vol. 142, pp. 87-119, 1852.
- 26) L. Maissel and R. Glang, Handbook of Thin Film Technology, New York: McGraw-Hill, 1970.
- 27) R. W. Berry, P. M. Hall, and M. T. Harris, Thin Film Technology, Princeton N. J. : Van Nostrand, 1968.
- 28) G. K. Wehner and G. S. Anderson, "The Nature of Physical Sputtering," in ref. 26.



- 29) M. Kaminsky, Atomic and Ionic Impact Phenomena on Metal Surfaces, Berlin: Springer-Verlag, 1965.
- 30) P. Sigmund, "Theory of Sputtering, I, Sputtering Yield of Amorphous and Polycrystalline Targets," Phys. Rev., vol. 184, pp. 383-416, 1969.
- 31) G. K. Wehner and D. Rosenberg, "Angular Distribution of Sputtered Materials," J. Appl. Phys., vol. 31, pp. 177-179, 1960.
- 32) G. S. Anderson, "Atom Ejection in Low Energy Sputtering of Single Crystal of fcc Metals and of Ge and Si," J. Appl. Phys., vol. 33, pp. 2017-2025, 1962.
- 33) R. S. Nelson and M. W. Thompson, "Atomic Collision Sequences in Crystals of Copper, Silver, and Gold Revealed by Sputtering in Energetic Ion Beams," Proc. Roy. Soc. (London), vol. A259, pp. 458-479, 1961.
- 34) L. Maissel, "Application of Sputtering to the Deposition of Films," in ref. 26.
- 35) N. Laegreid and G. K. Wehner, "Sputtering Yields of Metal for  $\text{Ar}^+$  and  $\text{Ne}^+$  Ions with Energies from 50 to 600 ev." J. Appl. Phys., vol. 32, pp. 365-369, 1961.
- 36) K. Pearmain and B. A. Unvala, "Sputtering of Silicon and gallium arsenide with medium energy intense ion beams of argon and xenon," Vacuum, vol. 25, pp. 3-7, 1974.
- 37) J. Comas and C. B. Cooper, "Mass-Spectrometric Study of Sputtering of Single Crystals of GaAs by Low-Energy A Ions," J. Appl. Phys., vol. 38, pp. 2956-2960, 1967.
- 38) R. Herzog, W. Poschenrieder, and F. Satkiewicz, "Observation of Clusters in a Sputtering Source," in reference 11.
- 39) H. W. Pickering, "Ion Sputtering of Alloys," J. Vac. Sci. Technol., vol. 13, pp. 618-621, 1976.
- 40) H. W. Werner and N. Warmolz, "The influence of selective sputtering on surface composition," Surface Science, vol. 57, pp. 706-714, 1976.
- 41) Z. L. Lau, W. L. Brown, R. Homer, and J. M. Poate, "Surface-layer composition changes in sputtered alloys and compounds," Appl. Phys. Lett., vol. 30, pp. 626-628, 1977.
- 42) W. K. Chu, J. K. Howard, and R. F. Lever, "Surface enrichment of copper due to ReV Xe sputtering of an Al-Cu mixture," J. Appl. Phys., vol. 47, pp. 4500-4503, 1976.
- 43) J. E. Green, B. R. Natarajan, and F. Sequeda-Osorio, "Sputtering of metal alloys containing second phase precipitates," J. Appl. Phys., vol. 49, pp. 417-425, 1978.

- 44) B. R. Natarajan, Glow Discharge Optical Spectroscopy for microvolume elemental analysis and sputtering diagnostics, C.S.L. Report R-668, 1974.
- 45) I. H. Wilson, "The Topography of Sputtered Semiconductors," in Reference 11.
- 46) W. D. Davis and T. A. Vanderslice, "Ion energies at the cathode of a glow discharge," Phys. Rev., Vol. 131, pp. 219-228, 1963.
- 47) J. Greene and F. Sequeda-Osorio, "Glow discharge Optical Spectroscopy for monitoring sputter deposited film thickness," J. Vac. Sci. Technol., vol. 10, pp. 1144-1149, 1973.
- 48) J. Greene, F. Sequeda-Osorio, and B. R. Natarajan, "Glow discharge Optical Spectroscopy as an analytical depth profiling technique," J. Vac. Sci. Technol., Vol. 12, pp. 366-369, 1975.
- 49) J. Greene, F. Sequeda-Osorio, and B. R. Natarajan, "Glow discharge optical spectroscopy for microvolume elemental analysis," J. Appl. Phys., vol. 46, pp. 2701-2709, 1975.
- 50) J. Greene, F. Sequeda-Osorio, B. Streetman, J. Noonan, and C. Kirkpatrick, "Measurement of boron impurity profiles in Si using glow discharge optical spectroscopy," Appl. Phys. Lett., vol. 25, pp. 435-439, 1974.
- 51) G. Marcyk and B. Streetman, "Boron impurity profile tailoring in silicon by ion implantation and measurement by glow discharge optical spectroscopy," J. Electro Chem. Soc., vol. 123, pp. 1388-1391, 1976.
- 52) G. Marcyk and B. Streetman, "Glow discharge optical spectroscopy measurement of arsenic implanted silicon," J. Vac. Sci. Technol., vol. 14, pp. 1165-1167, 1977.
- 53) A. von Hippel, "Kathodenzerstobungsprobleme," Annalen der Physik, vol. 80, pp. 672-707, 1926.
- 54) R. Stuart and G. Wehner, "Sputtering Thresholds and Displacement Energies," Phys. Rev. Lett., vol. 4, pp. 409-410, 1960.
- 55) R. Stuart and G. Wehner, "Sputtering Yields at Very Low Bombarding Ion Energies," J. Appl. Phys., vol. 33, pp. 2345-2352, 1962.
- 56) H. Ratinen, "Determination of the sputtering into by the fluorescence of sputtered atoms," J. Appl. Phys., vol. 44, pp. 2730-2734, 1973.
- 57) C. Lu, "Recent developments in monitoring and controlling techniques for alloy deposition processes," Thin Solid Films, vol. 45, pp. 481-490, 1977.



- 58) E. Sawatzky and E. Kay, "Method for Studying Sputtered Particles by Emission Spectroscopy," Rev. Sci. Instr., vol. 37, pp. 1324-1329, 1966.
- 59) C. W. White, D. L. Simms, and N. H. Tolk, "Surface Composition Determined by Analysis of Impact Radiation," Science, vol. 177, pp. 481-486, 1972.
- 60) N. Tolk, D. Simms, E. Foley, and C. White, "Photon Emission from Low-energy ion and neutral bombardment of solids" in Reference 11.
- 61) A. Stirling and W. Westwood, "Investigation of the Sputtering of Aluminum using Atomic-Absorption," J. Appl. Phys., vol. 41, pp. 742-748, 1970.
- 62) A. Stirling and W. Westwood, "A Spectroscopic Investigation of the Reactive Sputtering of Aluminum," Thin Solid Films, vol. 7, pp. 1-10, 1971.
- 63) W. D. Westwood, "Analysis of sputtering discharge by optical and mass spectroscopy," J. Appl. Phys., vol. 44, pp. 2619-2626, 1973.
- 64) H. Ratinen, "Rf sputtering investigations using an apparatus equipped with an optical spectrometer," Acta. Poly. Scand., Ph. 103, pp. 7-36, 1974.
- 65) F. Sequeda-Osorio, "Glow Discharge Optical Spectroscopy for Sputtering Diagnostics," Thesis (University of Illinois), 1978.
- 66) Massachusetts Institute of Technology, Wave Length Table, Boston, Mass.: MIT Press, 1969.
- 67) A. R. Striganov and N. S. Sventitskii, Tables of Spectral Lines of Neutral and Ionized Atoms, New York: Plenum Press, 1968.
- 68) National Bureau of Standards, Tables of Spectral Line Intensities, N.B.S. Monograph 32 Part 1, Washington: U.S. Government Printing Office, 1961.
- 69) A. Mitchell and M. Zemansky, Resonance Radiation and Excited Atoms, London: Cambridge at the University Press, 1971.
- 70) B. Moiseiwitch and S. Smith, "Electron Impact Excitation of Atoms," Reviews of Modern Physics, vol. 40, 1968.
- 71) L. G. Christophorou, Atomic and Molecular Radiation Physics, New York: Wiley-Interscience, 1971.
- 72) J. Heller, "Reactive Sputtering of Metals in Oxidizing Atmospheres," Thin Solid Films, vol. 17, pp. 163-176, 1973.
- 73) B. Goranchev, V. Orlinov, and V. Popovu, "D.C. Cathode Sputtering: Influence of the oxygen content in the gas flow on the discharge current," Thin Solid Films, vol. 33, pp. 173-183, 1976.



- 74) B. R. Naturajan, "Glow Discharge-Optical Spectroscopy for Micro volume Elemental Analysis and Sputtering Diagnostics," Thesis (University of Illinois), 1974, Chap 2, ref 23.
- 75) K. Yasuda, "Relationship between Resonance Line Profile and Absorbance on Atomic Absorption Spectroscopy," Anal. Chem., vol. 38, pp. 592-599, 1966.
- 76) J. E. Houston and R. D. Bland, "Relationship between Sputter Cleaning Parameters and Surface Contaminents," J. Appl. Phys., vol. 44, pp. 2504-2508, 1973.
- 77) The Arsenic implants were performed by Dr. Pradep Shah of Texas Instruments.
- 78) W. Kern and D. A. Pontinen, "Cleaning solutions based on hydrogen peroxide for use in silicon semiconductor technology," RCA Review, vol. 31, pp. 187-206, 1970.
- 79) M. J. Helix, R. V. Vaidyanathan, B. G. Streetman, H. B. Dietrich, and P. K. Chatterjee, "RF Plasma Deposition of Silicon Nitride Layers," unpublished.
- 80) D. R. Myers, "Properties of silicon implanted with arsenic through silicon dioxide," thesis, U. of Illinois, 1977.
- 81) W. K. Chu, B. L. Crowder, J. W. Mayer, and J. F. Ziegler, "Range distributions of implanted ions in  $\text{SiO}_2$ ,  $\text{Si}_3\text{N}_4$ , and  $\text{Al}_2\text{O}_3$ ," Appl. Phys. Lett., vol. 22, pp. 490-491, 1973.
- 82) R. M. Burger and R. P. Donovan, Fundamentals of silicon integrated device technology, volume I, New Jersey: Prentice-Hall, 1967.
- 83) F. A. Trumbore, "Solid Solubilities of Impurity Elements in Germanium and Silicon," Bell. Sys. Tech. J., vol. 39, pp. 205-233, 1960.
- 84) S. Y. Chiang and G. L. Pearson, "Properties of vacancy defects in GaAs single crystals," J. Appl. Phys., vol. 46, pp. 2986-2991, 1975.
- 85) E. Bell, A. G. Laecum, P. Hemment, and B. Sealy, "Heat Treatment of Ion Implanted GaAs," Rad. Effects, vol. 22, pp. 253-258, 1974.
- 86) K. V. Vaidyanathan, M. J. Helix, D. J. Wolford, B. G. Streetman, R. J. Bluttner, and C. A. Evans, Jr., "Study of encapsulants for Annealing GaAs," J. Electrochem. Soc., vol. 124, pp. 1781-1784, 1977.
- 87) V. M. Zelevinskaya and G. A. Kachurin, "Behavior of germanium implanted in GaAs by ion bombardment," Sov. Phys. Semicond., vol. 5, pp. 1011-1013, 1971.

- 88) T. T. Lavrishchev and S. S. Khludkov, "How the vapor pressure of arsenic affects diffusion of germanium in gallium arsenide," Izv. Akad. Naur. SSR, Neorg. Mater., vol. 7, pp. 310-311, 1971.
- 89) H. C. Casey, Jr., "Diffusion in the III-V Compound Semiconductors," in Atomic Diffusion in Semiconductors, D. Shaw, ed., New York: Plenum, 1973.
- 90) J. Comas, L. Plew, P. K. Chatterjee, W. V. McLevige, K. V. Vaidyanathan, B. G. Streetman, "Impurity Distribution of Ion-Implanted Be in GaAs by SIMS, Photoluminescence and Electrical Profiling," in Ion Implantation in Semiconductors, F. Chernow, J. A. Borders, and D. K. Brice, eds., New York: Plenum, 1977.
- 91) W. R. Runyan, Semiconductor Measurements and Instrumentation, New York: McGraw-Hill, 1975.
- 92) R. B. Fair and J.C.C. Tsai, "The diffusion of ion-implanted arsenic in silicon," J. Electrochem. Soc., vol. 122, pp. 1689-1696, 1975.
- 93) B. L. Crowder, "The influence of the amorphous phase on ion distribution and annealing behavior of Group III and Group V ions implanted into silicon," J. Electrochem Soc., vol. 118, pp. 943-948, 1971.
- 94) S. M. Hu, "Diffusion in silicon and germanium," in Atomic Diffusion in Semiconductor, D. Shaw, ed., New York: Plenum, 1973.
- 95) F. E. Rosztoczy, F. Ermanis, I. Hayashi, and B. Schwartz, "Germanium Doped Gallium Arsenide," J. Appl. Phys., vol. 41, pp. 264-270, 1970.
- 96) F. E. Rosztoczy and K. B. Wolfstirn, "Distribution Coefficient of Germanium in Gallium Arsenide Crystals grown from Gallium Solutions," J. Appl. Phys., vol. 42, pp. 426-429, 1971.
- 97) W. Schairer and W. Graman, "Photoluminescence from Ge doped GaAs grown by vapor-phase epitaxy," Phys. Chem. Solids, vol. 30, pp. 2226-2229, 1969.
- 98) H. Kasano, "Diatomic-complex donor and acceptor model for Ge-doped vapor-grown GaAs," J. Appl. Phys., vol. 49, pp. 4028-4030, 1978.
- 99) A. V. Cho and I. Hayashi, "P-N junction formation during Molecular-Beam Epitaxy of Ge-Doped GaAs," J. Appl. Phys., vol. 42, pp. 4422-4425, 1971.
- 100) J. A. Higgins, R. L. Kuvas, F. H. Eisen, and D. R. Ch'en, "Low-Noise GaAs FET's Prepared by Ion Implantation," IEEE Trans. Elect. Dev., vol. ED-25, pp. 587-596, 1978.
- 101) B. Shin, "Carbon-ion-implanted gallium arsenide," App. Phys. Lett., vol. 29, pp. 435-440, 1976.



- 102) G. R. Antell, "The effect of the anneal ambient on implanted GaAs and the occurrence of compensated regions in Si implants," Appl. Phys. Lett., vol. 30, pp. 432-434, 1977.
- 103) M. J. Helix, K. V. Vaidyanathan, and B. G. Streetman, "Properties of Be-Implanted Planar Ga As p-n junctions," Unpublished.
- 104) C. T. Sah, R. N. Noyce, and W. Shockley, "Carrier generation and recombination in p-n junctions and p-n junction characteristics," Proc. IRE, vol. 45, pp. 1228-1243, 1957.



## VITA

Gerald T. Marcyk was born on September 9, 1951 in Thoruton, Illinois. He received a B.S. degree in Electrical Engineering from the University of Illinois in 1973. As an undergraduate, Mr. Marcyk was a recieipient of a United Steelworkers of America, District 31 scholarship. He received his M.S. and Ph.D. degrees in Electrical Engineering from the University of Illinois in 1976 and 1978, respectively. He is a member of the Electrochemical Society and the Institute of Electrical and Electronics Engineers.